12-2006

The Thermophysical Roll of Nanoparticles in Nanofluidic Heat and Mass Transport

Chan Hee Chon
University of Tennessee - Knoxville

To the Graduate Council:

I am submitting herewith a dissertation written by Chan Hee Chon entitled "The Thermophysical Roll of Nanoparticles in Nanofluidic Heat and Mass Transport." I have examined the final electronic copy of this dissertation for form and content and recommend that it be accepted in partial fulfillment of the requirements for the degree of Doctor of Philosophy, with a major in Mechanical Engineering.

Kenneth D. Kihm, Major Professor

We have read this dissertation and recommend its acceptance:

Masood Parang, Anthony E. English, Jayne Wu

Accepted for the Council:

Carolyn R. Hodges

Vice Provost and Dean of the Graduate School

(Original signatures are on file with official student records.)

To the Graduate Council:

I am submitting herewith a dissertation written by Chan Hee Chon entitled “The Thermophysical Roll of Nanoparticles in Nanofluidic Heat and Mass Transport.” I have examined the final electronic copy of this dissertation for form and content and recommend that it be accepted in partial fulfillment of the requirements for the degree of Doctor of Philosophy, with a major in Mechanical Engineering.

Kenneth D. Kihm
Major Professor

We have read this dissertation
and recommend its acceptance:

Masood Parang

Anthony E. English

Jayne Wu

Accepted for the Council:

Linda Painter

Interim Dean of Graduate Studies

(Original signatures are on file with official student records.)

THE THERMOPHYSICAL ROLL OF NANOPARTICLES IN NANOFLUIDIC HEAT AND MASS TRANSPORT

A Dissertation

Presented for the

Doctor of Philosophy

Degree

The University of Tennessee, Knoxville

Chan Hee Chon

December 2006

DEDICATION

to my wife Haejeong, two daughters Hannah and June,

and my Lord …

ACKNOWLEDGEMENTS

I give sincere appreciation and thanks to my faculty advisor Dr. Kenneth Kihm for his continuous encouragement, valuable advice, and support throughout the course of this study. Also I would like to thank my dissertation committee members, Dr. Masood Parang, Dr. Anthony English, and Dr. Jayne Wu for their advice and constructive comments and voluntary supports.

Special thanks are expressed to the MINSFET Lab former and current members, Dr. Sokwon Paik, Mr. Iltai Kim, Mr. Changkyung Choi, Mr. Chuck Margrave, and Mr. Seonghwan Kim, and last two special persons, visiting scholar Mr. Hyundong Kim for his help in PIV study and my collaborator Joseph Tipton particularly for his help in my experiments and writing.

I wish to extend my thanks to my dear father and mother and my mother in law for their continuous praying. Lastly I would like to give my most valuable love and appreciation to two my daughters, Hannah and June, and my wife, Haejeong for their sacrifices, patience, trust, and love.

> But now, this is what the LORD says--he who created you, O Jacob, he who formed you, O Israel: "Fear not, for I have redeemed you; I have summoned you by name; you are mine. When you pass through the waters, I will be with you; and when you pass through the rivers, they will not sweep over you. When you walk through the fire, you will not be burned; the flames will not set you ablaze. (Isaiah 41:1-2)

ABSTRACT

Nanofluids are colloids that consist of a base fluid and nanometer sized metallic particles, which serve to improve the heat and mass transport characteristics of nanofluids over those of the base fluid. Many researchers, attracted to the highly enhanced thermal conductivity, have studied nanofluids, and yet have never been able to reveal the basic mechanisms of their characteristic improvements. This present work thus seeks to gain an understanding of the role of nanoparticles in nanofluidic heat and mass transport characteristics through three experimental measurements: 1) thermal conductivity measurement, 2) thermophoretic motion measurement, and 3) evaporation measurement.

Using thermal conductivity, thermophoresis, and evaporation measurements of nanofluids, nanofluidic heat and mass transport has been studied, thermal conductivity model has been derived, and the roles of nanoparticles in nanofluids have been revealed. Thus, the present work contributes specifically towards an understanding of the fundamental role of nanoparticles in the heat and mass transport of nanofluids and generally towards the use nanofluids in heat and mass transport applications.

Keywords: Nanofluid, Nanoparticle, Thermal conductivity, Droplet evaporation, Heat transfer, Mass transfer, Particle motion, Brownian motion, Thermophoresis

TABLE OF CONTENTS

LIST OF TABLES

LIST OF FIGURES

FIGURE Page

FIGURE Page

FIGURE Page

FIGURE Page

FIGURE Page

NOMENCLATURE

Material properties

μ	-	Absolute viscosity ($N \cdot s/m^2$)
ρ	-	Density (kg/m^3)
k	-	Thermal conductivity ($W/m \cdot K$)
α_t	-	Thermal diffusivity (m^2/s)
C_p	-	Specific heat (J/kg·K)
α	-	Resistance-temperature coefficient (0.003715 K^{-1})
κ^*	-	Normalized thermal conductivity (k_p/k_{BF})
v	-	Kinematic viscosity (m^2/s)

Dimensional Variables

l	-	Mean free path (m)
d	-	Diameter (m)
L	-	Length (m)
A	-	Surface area, which heat transfer takes place on (m^2)
U_s	-	Particle settling velocity (m/s)
U	-	Velocity (m/s)
g	-	Gravitational acceleration (m/s^2)
Q	-	Applied electric power per unit length (W/m)
q	-	Heat transfer rate (W)
T	-	Temperature (K)

Δk	-	Thermal conductivity enhancement ($W/m \cdot K$)
∇T	-	Temperature gradient (K/m)
t	-	Time (s)
R	-	Resistance (Ω)
i	-	Current (A)
V	-	Voltage (V)
k_b	-	Boltzmann constant (J/K·molecule)
Δx	-	Distance between hot and cold plates (m)
D_{dif}	-	Diffusion coefficient (m^2/s)
P_s	-	Supplied electric power (W)
ρ_r	-	Resistivity (Ω·m)
w_{HT}	-	Heater array width (m)
d_{HT}	-	Heater array thickness (m)
D_w	-	Droplet wet diameter (m)
r_w	-	Droplet wet radius, $D_w/2$ (m)
h	-	Planck constant
R_g	-	Specific gas constant,
f_v	-	Vibration frequency (s^{-1})

<u>Dimensionless Variables</u>

τ	-	Nondimensional time
f	-	Volume concentration
Pr	-	Prandtl number

Re	-	Reynolds number
S	-	Slope of the linear portion of the temperature – ln t curve
γ	-	Euler constant (0.577216…)
C_γ	-	Constant value of exponential γ
ε_P	-	Precision error
ε_B	-	Bias error
ε_U	-	Uncertainty, mean square value of precision and bias errors
C_a	-	Accommodation coefficient
Kn	-	Knusen number
C_t	-	Dimensionless thermal slip coefficient
C_s	-	Dimensionless temperature jump coefficient
C_m	-	Dimensionless frictional slip coefficient
N	-	Number of particles
$\tilde{N}$	–	Molar Avogadro number

Subscript

p	-	Particle
BF	-	Base fluid
S	-	Sample
R	-	Reference
s	-	Stationary
w	-	Wire
o	-	Reference temperature

th	-	thermophoresis
Br	-	Brownian motion
HT	-	Heater
div	-	Voltage divider circuit
hp	-	Heat propagation

CHAPTER 1

INTRODUCTION

The twenty-first century is an era of technological advancement and has already seen dramatic changes in almost every industry. Above all, "miniturization" is perhaps the most important topic in technology and has led to the advent of micro-/nanotechnology that was first predicted by Nobel Price winner Richard Feynmann less than 50 years ago (Rohrer, 1996). In addition, market demands for higher work load and capacity have also increased and brought about technical advances. For example, the first generation digital computer ENIAC required 1800 square-feet and could multiply two 10 digit numbers with the speed of 300 multiplications per second (Goldstine & Goldstine, 1982). By the late 1980's, however, the desktop size personal computer could perform 4,000,000 multiplications per second. These technological advances of smaller size and higher performance require more efficient energy transport in many industries, from heavy duty vehicle engine to micro device cooling. To satisfy these needs, traditional coolant, such as water, oil, and ethylene glycol mixture are inherently poor heat transfer fluids. It is well known that metals have orders-of-magnitude higher thermal conductivities than those of fluids (Touloukian et al., 1970). For instance, the thermal conductivity of copper is about 700 times greater than that of water, as shown in Figure 1-1. The thermal conductivity of metallic liquids is much greater than that of nomnetallic liquids. Therefore, the significantly high thermal conducting fluid as a metallic liquid could be expected to be used for a future coolant and the fluids that contain suspended solid metallic particles

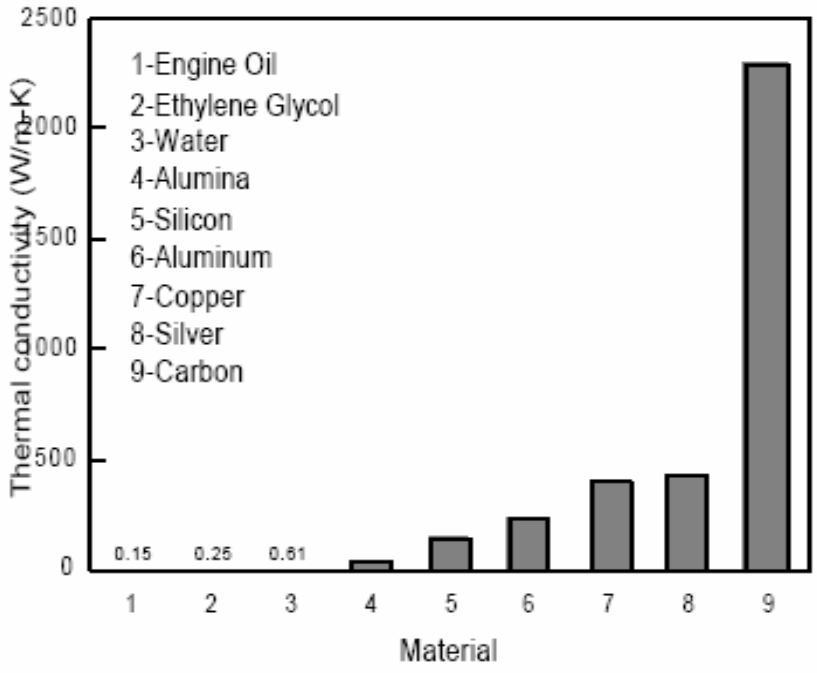

Figure 1-1. Thermal conductivities of typical materials (Eastman et al., 2004)

could be a candidate for achieving the significantly higher thermal conductivity than that of a conventional heat transfer coolant (Eastman et al., 2004).

1.1 Nanofluid

Nanofluid, first suggested by S.U.S. Choi of Argonne National Lab in 1995 (Choi), is a new, innovative working fluid for heat transfer created by dispersing highly thermal conducting solid particles smaller than 50 nanometers in diameter in traditional low thermal conducting heat transfer fluids such as water, engine oil, and ethylene glycol. Recently developed, highly efficient, small scale, heat transfer technologies such as the micro-refrigerator (Zhang et al., 2005), spray cooling (Vanam et al., 2005), and heat pipes (Peterson, 1994), have effective cooling rates but are limited to small scale cooling. On

the other hand, nanofluid can be used in microchannels as well as large scale cooling, such as heavy duty vehicle engines. This is possible, in part, due to current fabrication technologies that can produce nanoparticles down to a few nanometers in diameter.

Nanoparticles have many attractive characteristics to lend to the idea of a nanofluid. First of all, nanoparticles are free from the sedimentation. From Equation (1-1), the particle sedimentation speed depends on particle size, base fluid viscosity, and density difference between particle and base fluid. The easiest way to be free from sedimention is to minimize particle size and the speed goes to zero with nanometer-size particle.

$$U_s = \frac{2}{9}\frac{d_p^{\,2}}{\mu_{BF}}\left(\rho_p - \rho_{BF}\right)g \tag{1-1}$$

In addition, the surface area of a nanoparticle is 1,000 times larger than that of a microparticle. Since heat transfer occurs on the surface of a fluid, this feature greatly enhances the fluid's heat conduction. The smaller the particle, the greater the capacity for enhancing heat transfer. This was proven by initial research at Argonne National Lab with several nanoparticles and base fluids. The research indicates a dramatic enhancement of nanofluid thermal conductivity as shown in Figure 1-2.

1.2 Motivation and Objectives

Nanofluids attracted many researchers due to surprisingly higher thermal conductivities than those of the theoretical prediction by Maxwell (1904) and Hamilton-Crosser (1962), whose theories have good agreement to estimate the effective thermal conductivity of solid particles in continuum phase. To understand the mechanism of these abnormalities, many researches have been conducted and published by both numerical/

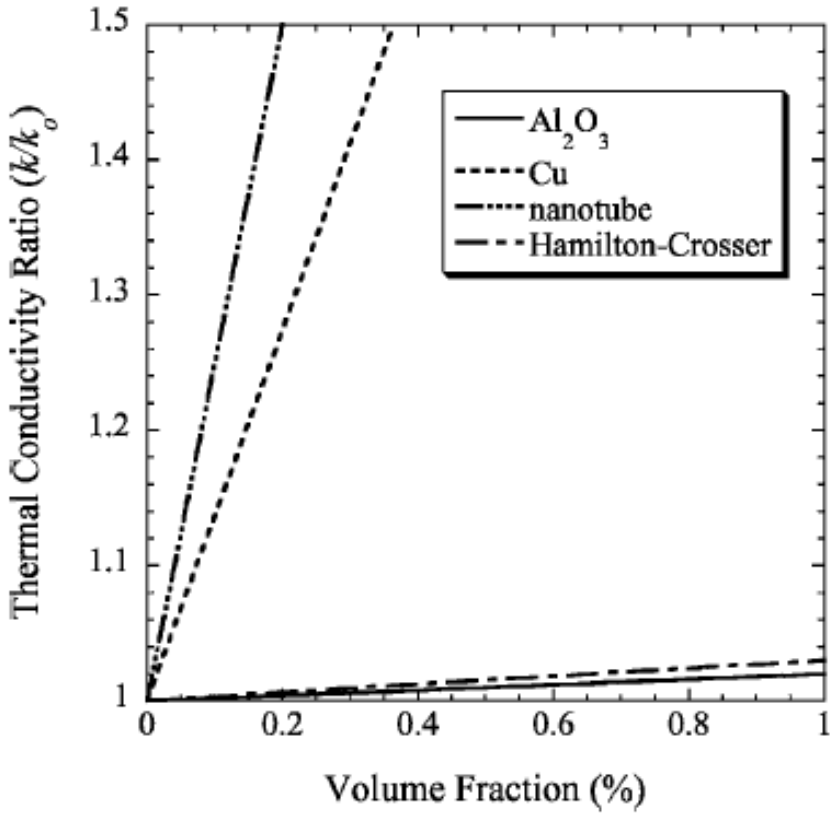

Figure 1-2 Thermal conductivity enhancements of example nanofluids depending on particle's volume fraction. The data originates from the published research output of Argonne National Lab. (Choi et al, 2004)

theoretical and experimental approaches. Recently, comprehensive theoretical (Keblinski *et al.*, 2002; Yu and Choi, 2003; Xuan *et al.*, 2003; Jang and Choi, 2004; Kumar *et al.*, 2004) and experimental (Das *et al.*, 2003; Patel *et al.*, 2003) studies have been announced. These studies suggest the nanoparticle plays an important role on thermal conductivity enhancement by way of microconvection, which is from the disturbance of a thermally driven nanoparticle against the base fluid molecules (Krishnamurthy et al., 2006). However, this theory is controvertial and cannot fully explain the fundamentals of heat characteristics of nanofluids such as nanofluid thermal conductivity control factors and theoretical thermal conductivity prediction. Therefore this study aims to reveal the physical and comprehensive understandings for the nanoparticle's role on nanofluid fluidic and thermal characteristics by three different experimental approaches: (1) thermal conductivity measurement, (2) thermophoretic velocity measurement, and (3) droplet evaporation measurement.

1.3 Literature Survey

The studies of the effective thermal conductivity have been started from Maxwell more than 100 years ago (Maxwell, 1904) for the case of spherical shaped-solid particle embedded in continum phase and extended for general shaped-solid particles by Hamilton and Crosser (1962). After Adler group's study (Wang et al., 1992), numerous theoretical and experimental studies of the effective thermal conductivity of dispersions that contain solid particles have been conducted. However, all of the studies on thermal conductivity of suspensions have been confined to millimeter- or micrometer-sized particles. The major problem with suspensions containing millimeter- or micrometer-

sized particles is the rapid settling of these particles. Furthermore, such particles are too large for micro systems.

Modern nanotechnology provides great opportunities to process and produce materials with average crystallite sizes below 50 nm. Recognizing an opportunity to apply this emerging nanotechnology to established thermal energy engineering, Choi (1995) proposed that nanometer-sized metallic particles could be suspended in industrial heat transfer fluids such as water, ethylene glycol, or engine oil to produce a new class of engineered fluids with high thermal conductivity.

After Eastman et al. produced the first nanofluid in 1997 (Eastman et al., 1997), nanofluid thermal conductivity was measured in 1999 and 2001 (Lee et al., 1999; Eastman et al., 2001; Choi et al, 2001). Keblinski et al. in 2002 published the first theroretical approach to understand the thermal conductivity enhancement mechanism and other numerous studies have been conducted experimentally and theoretically to explain the mechanism of thermal conductivity enhancement and other heat management using nanofluids (Keblinski *et al.*, 2002; Yu and Choi, 2003; Xuan *et al.*, 2003; Jang and Choi, 2004; Kumar *et al.*, 2004; Das *et al.*, 2003; Patel *et al.*, 2003; Xie et al., 2005; Buongiorno, 2006; Krishnamurthy et al., 2006; Ding et al, 2006). These researches were almost all concenred with the the effect of nanoparticle motion generating micro-convection, which is considered as a key factor to explain the thermal conductivity discrepancy between classical theory and experimental results. Vadasz et al. suggested other possibilities to explain nanofluid thermal conducitivity (2005) such as thermal wave effects via hyperbolic heat conduction.

1.4 Organization of the Study

This study consists of three different experimental approaches and presents findings from them. Chapter 2 presents a nanofluid thermal conductivity measurement, which is sytematically designed to find the control factors for thermal conductivity enhancement by changing several factors, and theoretical model for enhanced thermal conductivity. Chapter 3 shows a nanoparticle thermophoretic velocity measurement for an understanding of thermally driven nanoparticle motion. Chapter 4 discusses the nanofluid droplet evaporation measurement. Thermo-fluidic characteristics of nanofluid droplet depending on particle size is studied using a micro-heater array. Chapter 5 presents the conclusions derived from this study and provides recommendations for further research.

CHAPTER 2

ENHANCED THERMAL CONDUCTIVITY OF NANOFLUIDS

2.1 Objective

Abnormally increased thermal conductivities of nanofluids impressed many researchers. However, even the basic mechanism of thermal conducivity enchancement has not been revealed since the idea of the nanofluid was first announced by Choi. Over the last few years, a number of more comprehensive theoretical studies (Keblinski et al., 2002; Yu and Choi, 2003; Xuan et al., 2003; Jang and Choi, 2004; Kumar et al., 2004, Prasher et al., 2005) have been published to predict the thermal conductivity enhancement of nanofluids after basic approaches using existing theories (Wang et al., 1999; Lee et al., 1999; Eastman et al., 2001; Choi et al., 2001; Xie et al., 2002), however, they show excessively large discrepancies between each other and are far from being established as a formidable model that can comprehensively describe the physics of nanofluid conductivity. Table 2-1 shows the chronological presentation of published typical theories predicting conductivities either for particle-embedded solid materials (Maxwell, 1904; Hamilton and Crosser, 1962) or for nanofluids (Xuan et al. 2003, Jang and Choi, 2004; Kumar et al., 2004; Prasher et al, 2005).

The first attempt of modeling goes back to 1873 by Maxwell (1904), who presented the effective thermal conductivity for a heterogeneous solid material, consisting of spherical solid particles of thermal conductivity k_p embedded in a continuous solid

Table 2-1. Historical development of nanofluidic thermal conductivity models

Author	Thermal conductivity enhancement, k_{eff}/k_{BF}
Maxwell (1873)	$\frac{k_{eff}}{k_{BF}} = \left[\frac{k_p + 2k_{BF} - 2f(k_{BF} - k_p)}{k_p + 2k_{BF} + f(k_{BF} - k_p)}\right]$
Hamilton & Crosser (1962)	$\frac{k_{eff}}{k_{BF}} = \left[\frac{k_p + (n-1)k_{BF} - (n-1)f(k_{BF} - k_p)}{k_p + (n-1)k_{BF} + f(k_{BF} - k_p)}\right]$
Xuan et al. (2003)	$\frac{k_{eff}}{k_{BF}} = \left[\frac{k_p + 2k_{BF} - 2f(k_{BF} - k_p)}{k_p + 2k_{BF} + f(k_{BF} - k_p)}\right] + f\frac{\rho_p c_p}{2k_{BF}}\sqrt{\frac{2k_b T}{3\pi d_p \mu}}$
Jang & Choi (2004)	$\frac{k_{eff}}{k_{BF}} = \left[(1-f) + \frac{\beta k_p}{k_{BF}} f + 3C_\alpha \frac{d_{BF}}{d_p}\mathrm{Re}_{d_p}^2 \mathrm{Pr}\, f\right], \quad \beta = 0.01$
Kumar et al. (2004)	$\frac{k_{eff}}{k_{BF}} = \left[1 + C_\beta\left(\frac{2k_b T}{\pi\mu d_p^2}\right)\frac{f d_{BF}}{k_{BF}(1-f)d_p}\right]$
Prasher et al. (2005)	$\frac{k_{eff}}{k_{BF}} = (1 + C_\gamma \mathrm{Re}^m \mathrm{Pr}^{0.333} f) + \left[\frac{1 + 2\alpha + 2f(1-\alpha)}{1 + 2\alpha - f(1-\alpha)}\right], \quad \alpha = \frac{2R_k k_{BF}}{d_p}$

where n is the empirical shape factor (n=3 for sphere), R_k is Kapitza resistance between a nanoparticle and surrounding, and C_α, C_β, C_γ, and m are empirical constants. Suggested constants (Kumar et al. 2004; Prasher et al. 2005) are 2.9 to 3.0 for C_β, 40000 for C_γ, and 2.4 to 2.75 for m.

phase with thermal conductivity k_{BF}. The volume concentration f of the embedded spheres is taken to be sufficiently small that the spheres do not interact thermally and the effect of the particle size is assumed negligible. Hamilton and Crosser (1962) extended the Maxwell's model to incorporate a modification for non-spherical particles by the empirical shape factor *n*.

A number of alternative models have been proposed with the use of the Brownian motion-induced micro-convection in a nanofluid. By adding the second term to the Maxwell model, Xuan et al. (2003) proposed a model incorporating the Brownian motion of nanoparticles.

A year later, Jang and Choi (2004) introduced the Brownian-motion-driven convection model and attempted to describe the temperature-dependency of nanofluid thermal conductivity. They assumed the Nusselt number (Nu) is the multiplication of Reynolds number and Prandtl number based on the postulation of Reynolds number of an order of unity. However, as Prasher et al. (2005) pointed out and stated in their paper, it is little justifiable to neglect all the relevant terms in the Nusselt number by wrong postulation of Reynolds number, which is inconsistent with their own definition of Reynolds number in the paper.

Kumar et al. (2004) attempted to incorporate the nanoparticle thermal conductivity based on the Brownian velocity. However, their model totally failed as asserted by unphysical prediction for the Brownian motion mean free path of a nanoparticle in fluid as the order of 1 cm.

Prasher et al. (2005) developed a model combining the Maxwell-Garnett model (Nan et al., 1997) incorporating both the Kapitza resistance effect of particles with the

surrounding medium and the effect of the Brownian motion-induced convection. However, they introduced less justifiable Brownian velocity of nanoparticles as $V_{Brownian} = \sqrt{18k_bT/\pi\rho_p d_p^3}$ based on the kinetic theory of gas, which is generally valid only for dilute gases.

For experimental approaches, although there are several reported experiments for nanofluid thermal conductivity measurements, systematically available experimental investigations are scarce except that the temperature dependence of nanofluid thermal conductivity has been presented either for limited temperature range (Das et al., 2003) or for extremely low concentration ranges (Patel et al., 2003).

Even though those previous efforts have sought to understand abnormally enhanced thermal conductivities of nanofluids, the fundamental explanation for them is not yet clearly defined. To delineate the principal mechanism of thermal conductivity enhancement, in this chapter a systematic experiment has conducted using some control factors such as nanoparticle size, volume concentration, and nanofluid temperature for the case of Al_2O_3 nanofluids. From these experiments, an empirical correlation is functionalized and its physical interpretation is focused on the aforementioned effects. Furthermore, based on the introduced thermal propagation velocity concept, the thermal conductivity is predicted theoretically.

2.2 Thermal Conductivity and Measurement

2.2.1 Heat conduction and thermal conductivity

Heat conduction is the transport of energy in a medium due to a temperature gradient, and the physical mechanism is a random atomic or molecular activity governed by Fourier's law, Eq. (2-1).

$$q \propto A\nabla T \tag{2-1}$$

For different materials, the conduction equation Eq. (2-1) remains valid and we can re-write the Eq. (2-1) as Eq. (2-2) using the proportional constant, *k*.

$$q = kA\nabla T \tag{2-2}$$

However, at the same temperature gradient and conduction area, the heat transfer rate would be smaller for plastic than for metal. In Eq. (2-2) only the constant *k* is linearly dependent on heat transfer rate. The *k*, called thermal conductivity, only depends on material type and is an important property of the material. The range of thermal conductivities is enormous. As shown in Figure 2-1, the thermal conductivity of a solid may be more than four orders of magnitude larger than that of a gas. This trend is due largely to differences in intermolecular spacing for the two states. For a solid comprised of free electrons and of atoms bound in the lattice, transport of thermal energy is due to the migration of free electrons and lattice vibrational waves. The thermal conductivity of gases and liquids is generally smaller than that of solids since the intermolecular spacing is much larger and the motion of the molecules is more random. (Incropera and DeWitt, 2002; Bird *et al.*, 2002)

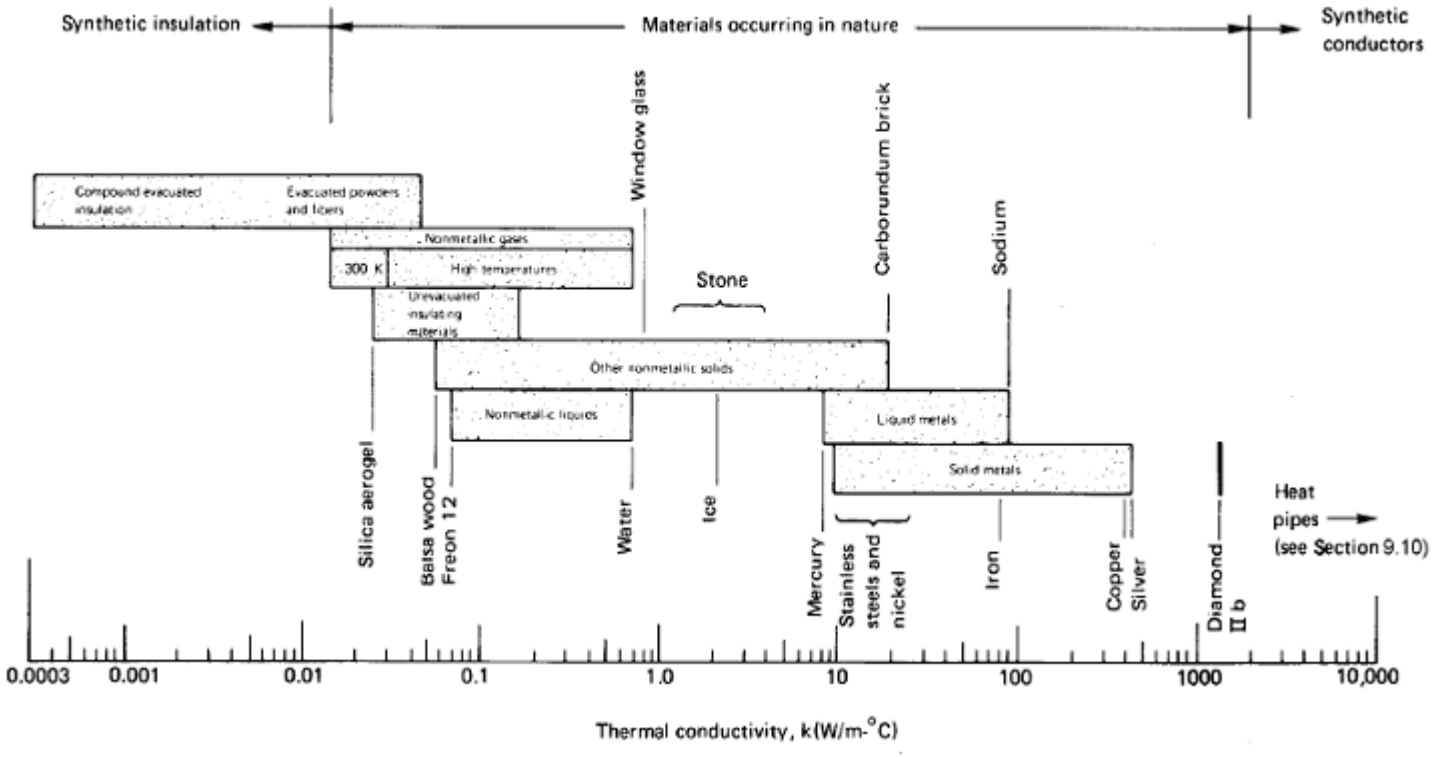

Figure 2-1. Thermal conductivity of sample materials. (Lienhard IV and Lienhard V, 2004)

2.2.2 Principal methods of thermal conductivity measurements

Based on Eq. (2-2), when an unknown material is inserted between a temperature difference $\Delta T(=T_1-T_2)$ with spacing ΔL, the thermal conductivity can be expressed as

$$k=\frac{q}{A\nabla T}=\frac{q\Delta L}{A\Delta T} \tag{2-3}$$

The measurement of thermal conductivity, therefore, always involves the measurement of the heat flux and temperature difference. Depending on heat flux measurements, the thermal conductivity measurements are divided in two categories: absolute and comparative measurements. The absolute measurement measures heat flux directly by measuring the electrical power going into the heater, and the comparative measurement is done indirectly by comparison.

In both cases, the entire heat flux must be uni-axial; that is it has to flow through the sample and the heat losses or heat gains must be minimized in the radial direction. To some degree, this can be accomplished with packing insulation around the sample. If the insulating guard is controlled to have the identical temperature gradient as the sample, then the radial heat flow will be minimized. When the specimen conductivity is high, the heat flux is usually fairly high so that heat losses from the large lateral surface area of the specimen are small and a long specimen in the direction of flow helps establish a reasonably high temperature gradient which can then be accurately measured. When the specimen conductivity is low and the heat flux correspondingly low, only a relatively small thickness is required to generate a large, accurately measurable gradient. Another independent parameter of fundamental importance is the magnitude of specimen conductivity relative to the surroundings. It is generally desired that the specimen effective

conductance be as high as possible relative to that of the surrounding insulation. The widely used three thermal conductivity measurement techniques are the axial flow, guarded hot plate, and hot-wire methods. (ASTM)

2.2.2.1 Axial Flow Methods. Axial flow methods have been long established and have produced some of the most consistent, highest accuracy results reported in the literature. It is the method of choice at cryogenic temperatures to minimize radial heat losses in the axial heat flow developed through the specimen from the electrical heater mounted at one end. For the comparative cut bar method (ASTM E1225 Test Method), it is the most widely used method for axial thermal conductivity measurement. The principle of the measurement lies with passing the heat flux through a known sample and an unknown sample and comparing the respective thermal gradients, which will be inversely proportional to their thermal conductivities shown as Figure 2-2.

Most commonly, the unknown is sandwiched between two known samples, "the references", to further account for minor heat losses that are very difficult to eliminate and thermal conductivity can be calculated as:

$$\frac{q}{A} = k_S \frac{\Delta T_s}{L} = k_R \frac{\Delta T_1 + \Delta T_2}{2L} \tag{2-4}$$

where k_S and k_R are the thermal conductivities of a sample and the references.

Another technique is the guarded or unguarded heat flow meter method (ASTM C518, E1530 Test Methods) which uses a flux gauge instead of the references in the comparative cut bar method. In practice, the reference material has a very low thermal conductivity and, therefore, it can be made very thin. Usually, a large number of

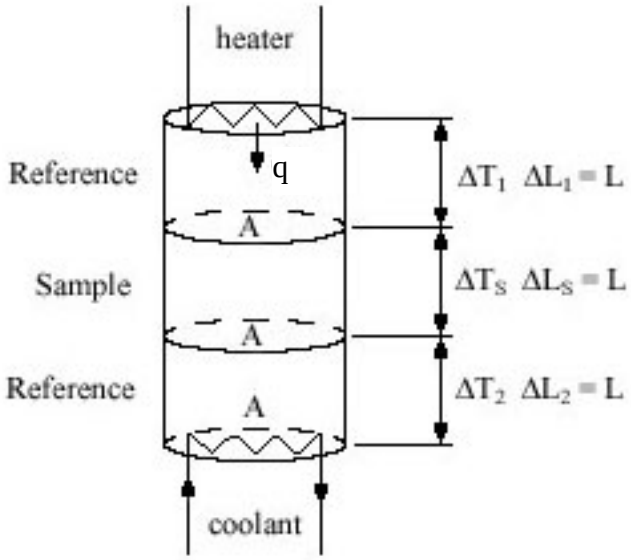

Figure 2-2. Axial flow thermal conductivity measurement method (ASTM E1225).

thermocouple pairs are located on both sides of the reference plate, connected differentially to yield directly an electrical signal proportional to the differential temperature across it. This type of flux gauge is mostly used with instruments testing very low thermal conductivity samples, such as building insulations.

2.2.2.2 Guarded Hot Plate Method (ASTM C 177 Test Method). The guarded hot plate is a widely used and versatile method for measuring the thermal conductivity of insulation. A flat, electrically heated metering section surrounded on all lateral sides by a guard heater section controlled through differential thermocouples supplies the planar heat source introduced over the hot face of the specimens. The most common measurement configuration is the conventional, symmetrically arranged guarded hot plate where the heater assembly is sandwiched between two specimens (Figure 2-3). This is an

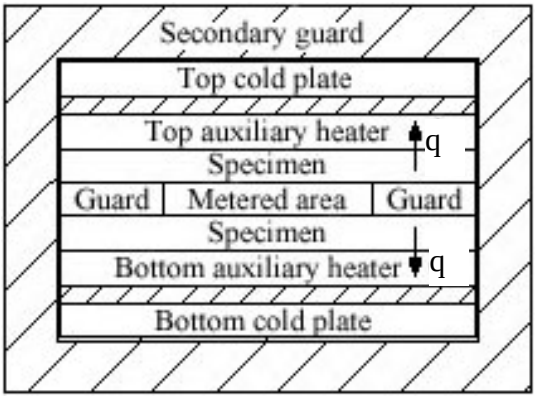

Figure 2-3. Guarded hot plate thermal conductivity measurement method (ASTM C177).

absolute and steady state method of measurement.

2.2.2.3 Hot Wire Method (ASTM C1113 Test Method). The hot wire method is basically a transient radial flow technique and is most commonly used to measure the thermal conductivity of "refractories" such as insulating bricks and powder or fibrous materials. The technique has been used in a more limited way to measure properties of liquids and plastics of relatively low thermal conductivity.

A probe containing a heater and a thermocouple is inserted in the test specimen and measures thermal properties such as thermal conductivity. When a certain amount of current is passed through the heater for a short period of time, the temperature history of the heater's surface will take on a characteristic form. In the initial phase, the temperature will rapidly rise, and as the heat begins to soak in, the rate of rise becomes constant. When the thermal front reaches the outer boundary of the sample, the rise will slow down or stop altogether due to losses into the environment. From the straight portion of the rate curve (temperature vs. time) the thermal conductivity can be calculated.

2.2.3 Transient Hot Wire Thermal conductivity measurement for Liquids

The transient hot wire method was introduced theoretically by Schieirmacher (1888) and practically by Van der Held and Van Drunen (1949). It is the most typical technique for fluid thermal conductivity measurement because it can neglect natural convection effects as well as provide the most accurate and very fast technique relative to steady state techniques. Very fine platinum wire is centered in the vertical test cell surrounded by an unknown fluid. The wire is used as a temperature sensor as well as a heat source (Roder, 1981). An ordinary transient hot wire technique is not adequate for nanofluids, however, because nanofluids are electrically conductive.

Nagasaka and Nagashima (1981) first proposed a new transient hot wire technique to overcome the ordinary transient hot wire technique to measure electrically conducting liquids. By coating electrical insulating material around the wire, the transient hot wire technique was extended to electrically conducting liquids. Many researches for nanofluids, which are likely to be electrically conducting, have therefore been adopted to the new transient hot wire technique.

2.2.3.1 Mathematical Analysis. In rectangular coordinates, temperature rise θ at time t and the origin of coordinates in an infinite solid due to a quantity of heat of being instantaneously generated at t=0 and the point (x, y, z) is given by Carslaw and Jaeger (1959; Maglic et al., 1984) as

$$\theta = \frac{q}{8\rho C_p (\pi \alpha_t t)^{3/2}} \exp\left(-\frac{x^2 + y^2 + z^2}{4\alpha_t t} \right) \tag{2-5}$$

where α is the thermal diffusivity expressed as $\alpha = k/\rho C_p$, k is the thermal conductivity, ρ is

the density, and C_p is the specific heat. If a quantity of heat, $Q'dz$,is instantaneously generated at $t=0$ and continued on the infinite line parallel to the z-axis and passing through the point ($x, y, 0$) , the temperature rise at the origin is

$$\begin{aligned}\theta &= \frac{Q}{4\pi k}\int_{r^2/4\alpha t}^{\infty}\frac{e^{-u}}{u}\cdot du, \qquad r = x^2 + y^2 \\ &= \frac{Q}{4\pi k}\left[-\left(E_1\frac{-r^2}{4\alpha_t t}\right)\right] \\ &= \frac{Q}{4\pi k}\cdot E_1\left(\frac{r^2}{4\alpha_t t}\right)\end{aligned} \tag{2-6}$$

where $E_1(x) = \int_x^{\infty} x^{-1}\exp(-x)dx$ and Q is the applied electric power as the line heat source per unit length. The exponential integral in (2-6) can be calculated by expressing the integrand as a McClaurin series and integrating term by term. For values of x small compared with unity it is sufficient to retain only the first two terms. Thus to a very good approximation the solution becomes

$$\theta = \frac{Q}{4\pi k}\cdot\ln\left(\frac{4\alpha_t t}{r^2 C_\gamma}\right) \tag{2-7}$$

where C_γ = exp γ, and γ = 0.577216… is the Euler constant. Therefore, the temperature rise θ_2 - θ_1 over a time interval t_2 - t_1 is

$$\theta_2 - \theta_1 = \frac{Q}{4\pi k}\cdot\ln\left(\frac{t_2}{t_1}\right) \tag{2-8}$$

and the thermal conductivity between times t_1 and t_2 using applied power is

$$k = \frac{Q}{4\pi(\theta_2 - \theta_1)}\cdot\ln\left(\frac{t_2}{t_1}\right) \tag{2-9}$$

which can be written as

$$k = \frac{Q}{4\pi S} \tag{2-10}$$

where S is the slope of the linear portion of the temperature – ln t curve.

Figure 2-4 shows how the temperature rise of a thin hot wire deviates from the ideal line heat source solution (Johns et al., 1988). At small times the temperature rise is less than that of the ideal case because of the finite heat capacity of the wire. At long times the temperature rise is also less than that of the ideal case because of the finite outer boundary of the cell or natural convection. Therefore the central portion of the curves, which is close to the ideal case, is utilized in the transient hot wire method.

2.2.3.2 Types of Transient Hot Wire Method. The transient hot wire method practically used in a real experiment has high accuracy and well meets with an idealized model. However, it has still some deviations from the ideal model as shown in Table 2-2 and needs some corrections in practical uses. For more accurate analysis Jones *et al.* (1988), Kestin and Wakeham (1978), and Hammerschmidt and Sabuga (2000) analyzed each effect of the parameters to make different between a real and an ideal model and all deviation in Table 2-2 are not significant especially for liquids except the end effect from the finite lengths. As shown in Figure 2-5, the temperature rise in a practical experiment is not identical to that of the ideal. If the heat line source is long enough, temperature rises at the ends are negligible but they are significant in short wire length. To improve the existing end effects in the single-wire transient hot wire method, the two-wire transient hot wire method, which uses two wires that have same diameter but different length is developed based on Hinze's analysis (1975). In addition, Lee *et al.* have also applied a new method

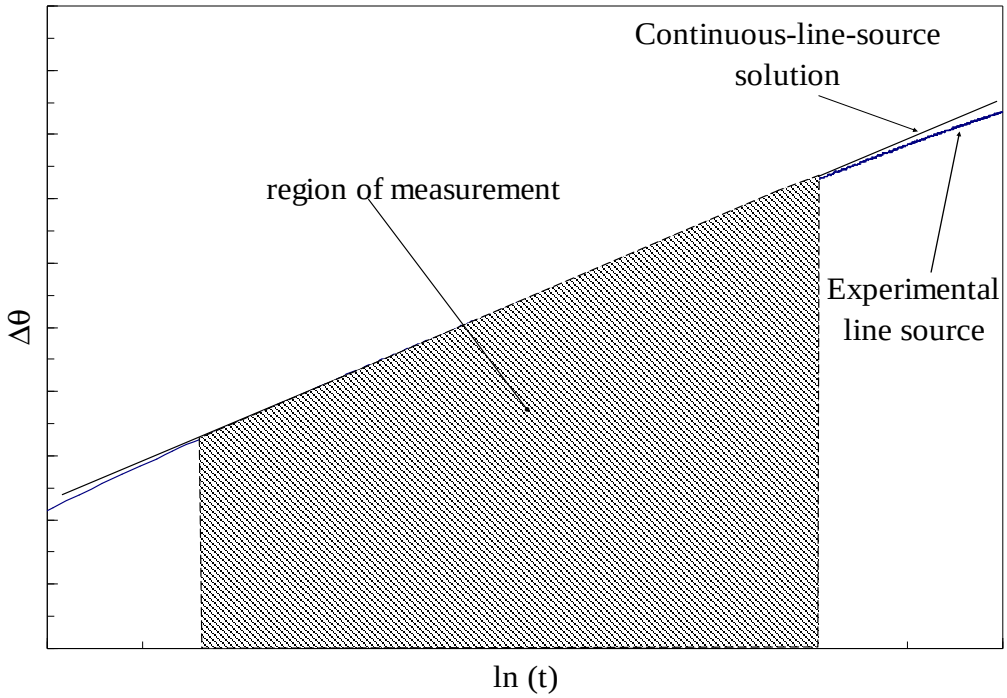

Figure 2-4. Typical plot of temperature rise against time for a hot wire experiment.

Table 2-2. Typical differences between ideal and real situation in a hot wire method

Ideal line source	Real hot wire line source
zero radius	finite radius
infinite lengths, no end effects	finite lengths, end effects
infinite medium	finite test section
conduction only mode of heat transfer	radiation and convection at long times

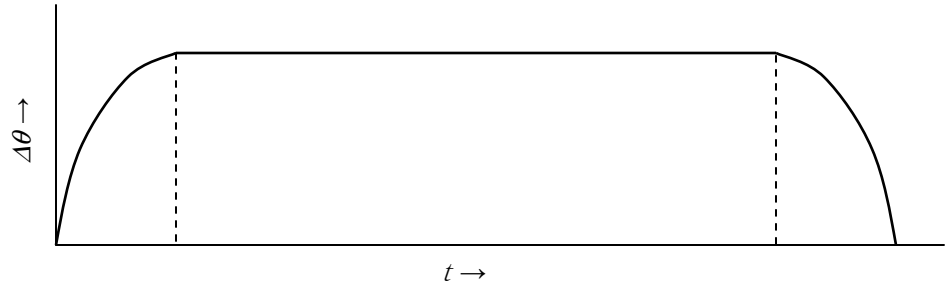

(a) practical temperature rise

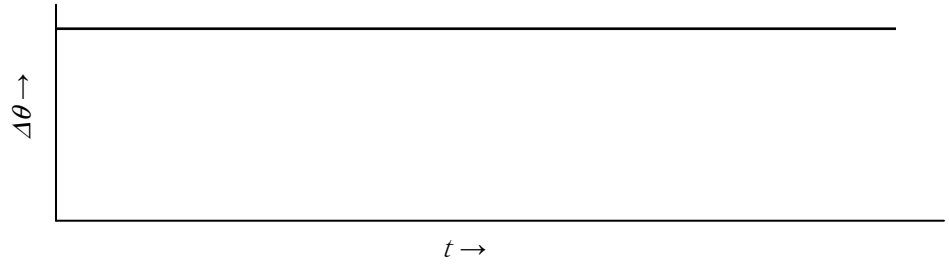

(b) ideal temperature rise

Figure 2-5. Temperature distribution along wires at time *t*

that uses the same priciple as the two-wire transient hot wire method, but with four or more wires (2004).

2.3 Experimental Setup and Verification Test

2.3.1 Experimental Setup

For the nanofluid thermal conductivity measurement, a single-wire transient hot wire method has been used with a miniaturized test chamber. This thermal conductivity measurement system consists of three parts: voltage divider circuitry, data acquisition, and

test chamber. The voltage divider is a series of two resistors with a known resistance, R_s, and an unknown platinum wire resistance, R_w, that varies with temperature. The heat generated from the platinum wire of Eq. (2-10) is calculated from the power calculation, $P_s = i^2 R_w$. The current i comes from Ohm's law, $i = V_s / R_s$ with known resistance, R_s, and supply voltage, V_s. The proper wire resistance is chosen to maximize the sensitivity of the voltage calculation, $\frac{dV_w}{dR_w} = \frac{R_s}{(R_s + R_w)^2} V_s$, and is maximum when $R_w = R_s$ as shown in Figure 2-6.

The test chamber contains less than 10 cc of nanofluid. In the center of the test chamber, a thin platinum wire acts as both a hot wire and a thermometer. Due to its well-known linear resistance-temperature relationship over a wide temperature range, the platinum wire is widely used in the transient hot wire technique. The platinum wire used in this experiment is 50 um in diameter with electrical insulation and is soldered to rigid electrical conducting supports. It is placed in the center of the closed container and positioned vertically to minimize convective effects. The ewire and welded spots are coated with an epoxy adhesive to insulate against electrical and heat conduction to the surrounding fluid.

Switching the power supply to the voltage divider initiates the voltage change in the hot wire, and the time varying voltage is recorded by NI PCI-6033 analog-digital (A/D) converter with a resolution of 1.22mV at a sampling rate of 50 Hz for 10 seconds. Due to insufficient signal resolution, the signal must first be amplified using operational

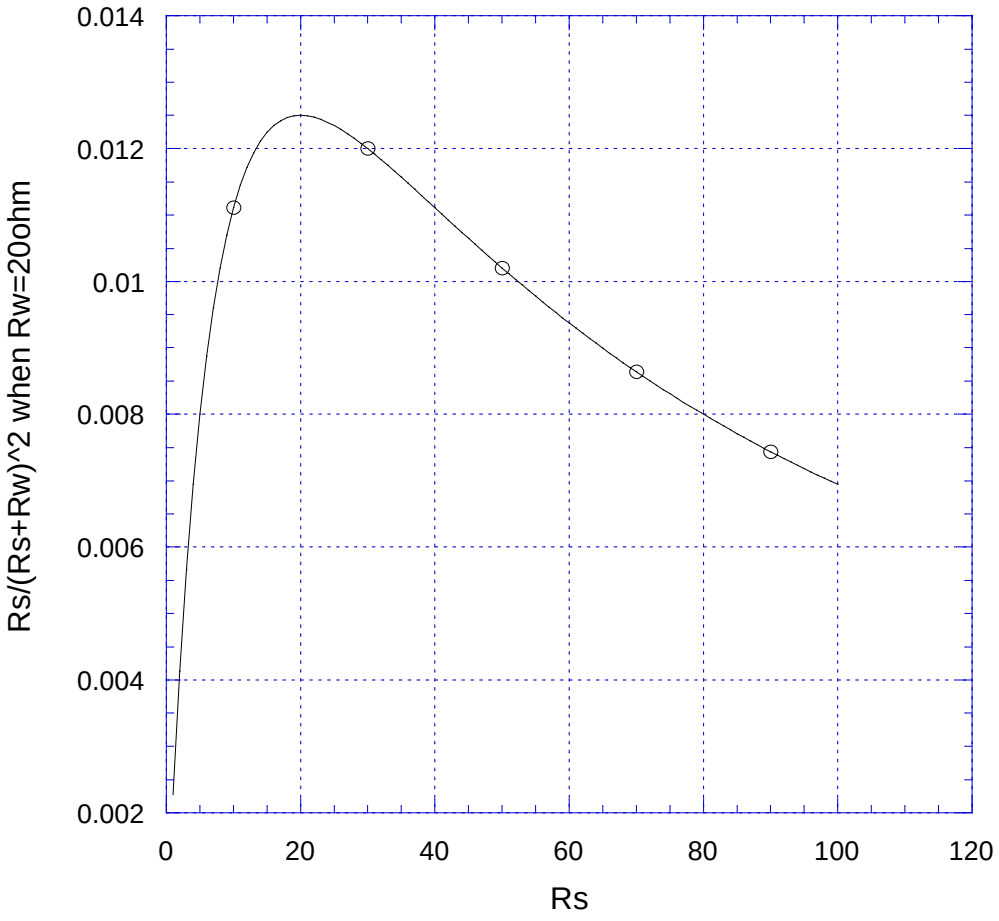

Figure 2-6. Sensitivity of voltage-divider circuit.

amplifiers. The measured voltage change is converted to resistance change and the heating current through the wire and the temperature variation of the wire can be calculated by the temperature-resistance relationship of the platinum wire.

Figure 2-7 shows the experimental setup scheme. From measured and calculated temperatures, measured times, and applied current, thermal conductivity can be calculated.

Figure 2-8 shows the schematic diagram of the signal amplifier and signals before and after the signal amplifier. The amplification magnitude is set by the fraction of two resistors. The amplification here is around 100 times over the raw signals and makes the signal resolution 100 times higher than that of the raw signal. A photo of the experimental setup is shown in Figure 2-9, which has a signal amplifier, a dc power supply, test chamber, etc.

2.3.2 Experiment Validation and Uncertainty Analysis

Validation tests of distilled water have been performed with the operating temperature ranging from 21 to 71 ºC. These experimental data were compared to the water thermal conductivity table by Incropera and DeWitt (2002). Figure 2-10 shows the test result with referece values. The measured thermal conductivities of water exist within 1.09% deviation of referece values at each temperature.

$$U = \sqrt{\left(\frac{\varepsilon_{Pq}^2 + \varepsilon_{Bq}^2}{q^2}\right) + \left(\frac{\varepsilon_{lw}^2 + \varepsilon_{lw}^2}{l_w^{\,2}}\right) + \left(\frac{\varepsilon_S^2 + \varepsilon_S^2}{s^2}\right) + \varepsilon_{Ui}^2} \qquad (2\text{-}11)$$

where ε_P, ε_B, and ε_{Ui} represent the precision error, bias-error, and uncertainty from the ideal model, respectively. Originally, the heat flux, q, and slope, S, are associated with

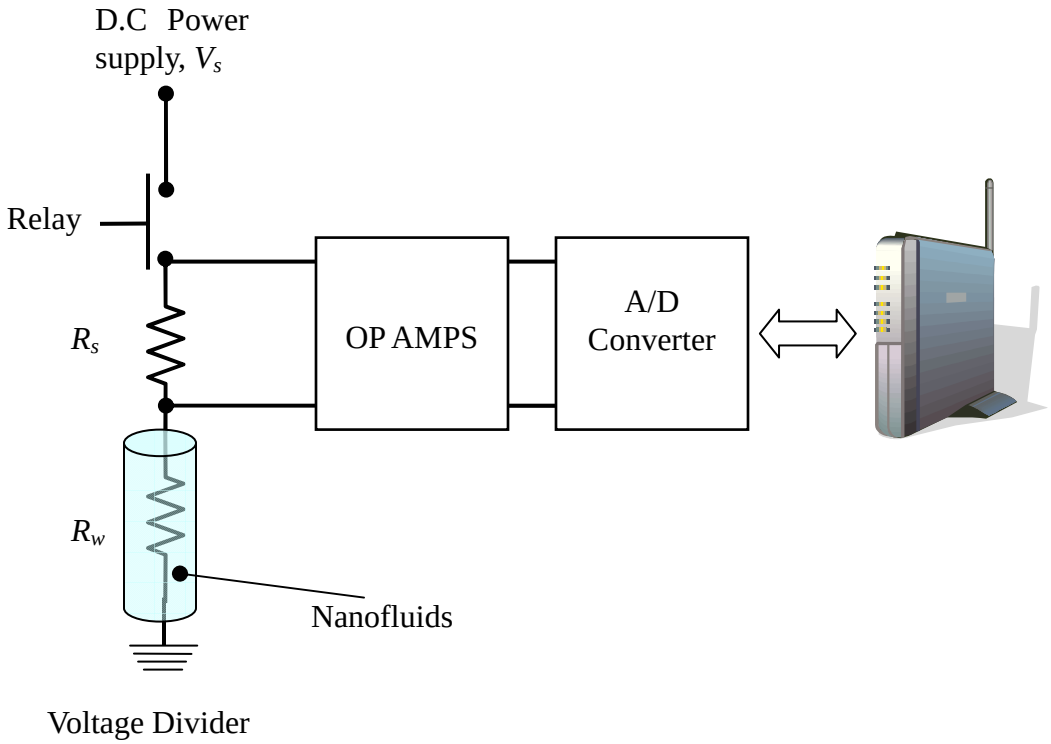

Figure 2-7. Experimental setup for nanofluid thermal conductivity measurement.

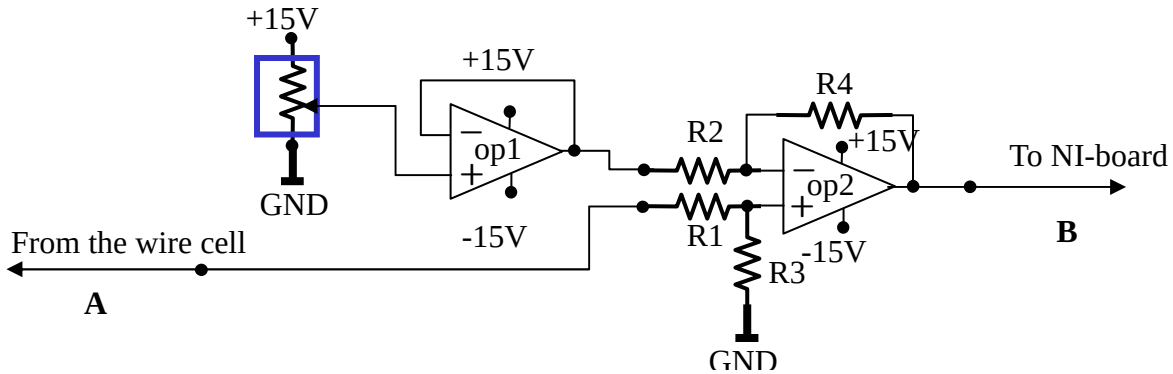

(a) signal amplifier

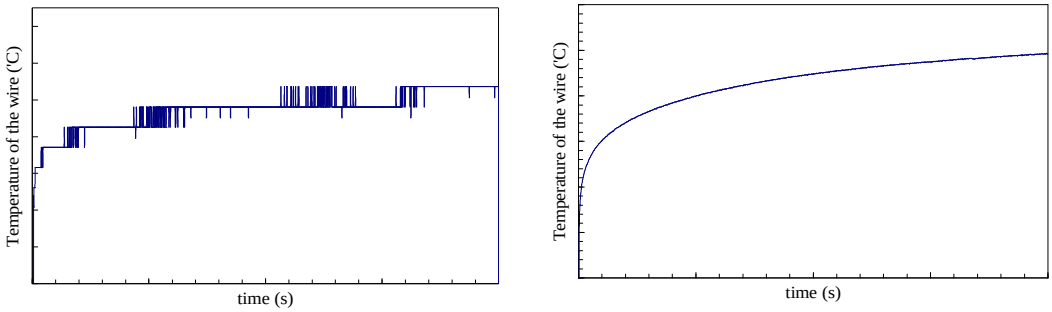

(b) signal at point A (c) signal at point B

Figure 2-8. Signal amplifier circuit diagram (a) and signals before (b) and after (c) the signal amplifier.

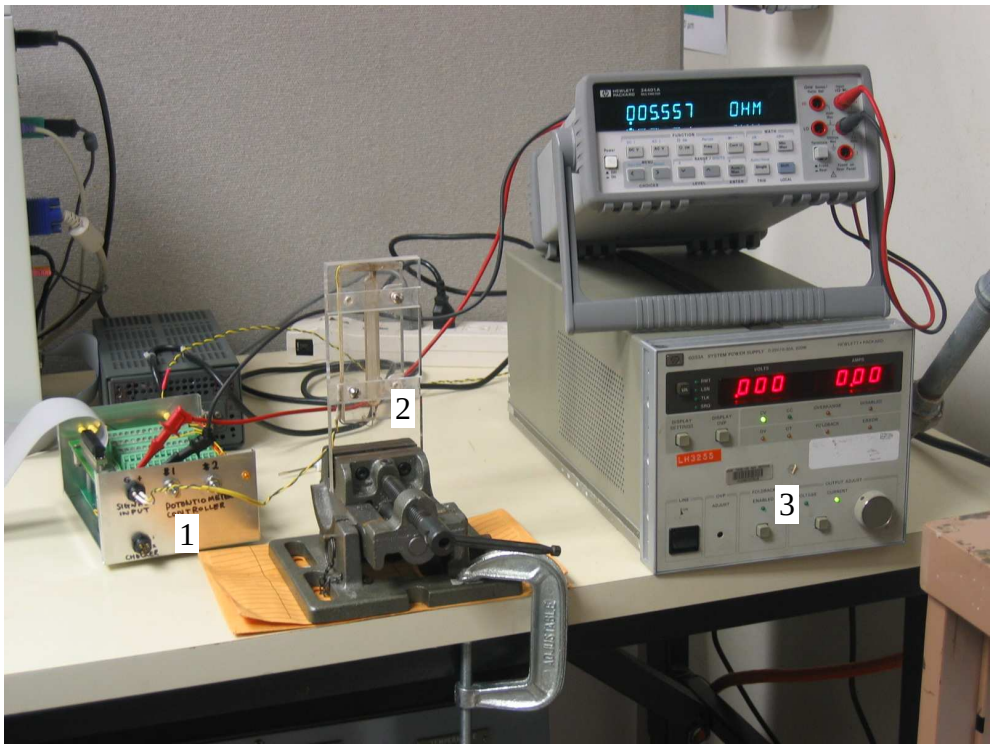

(a) Overview of the experimental setup

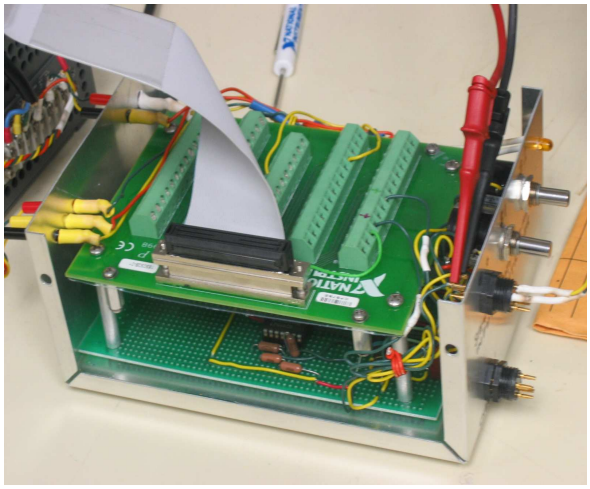

(b) Signal amplifier

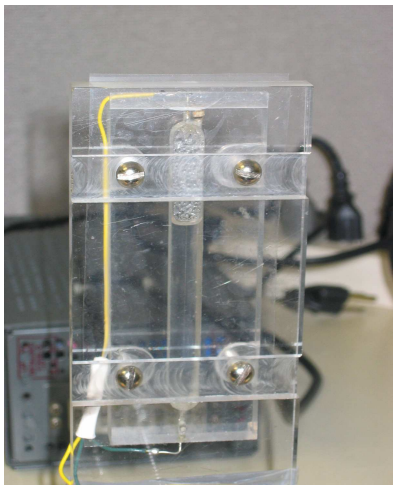

(c) test chamber

Figure 2-9. Picture of nanofluid thermal conductivity measurement test setup: 1. Signal amplifier, 2. Test chamber (< 10cc), 3. D.C Power supplier

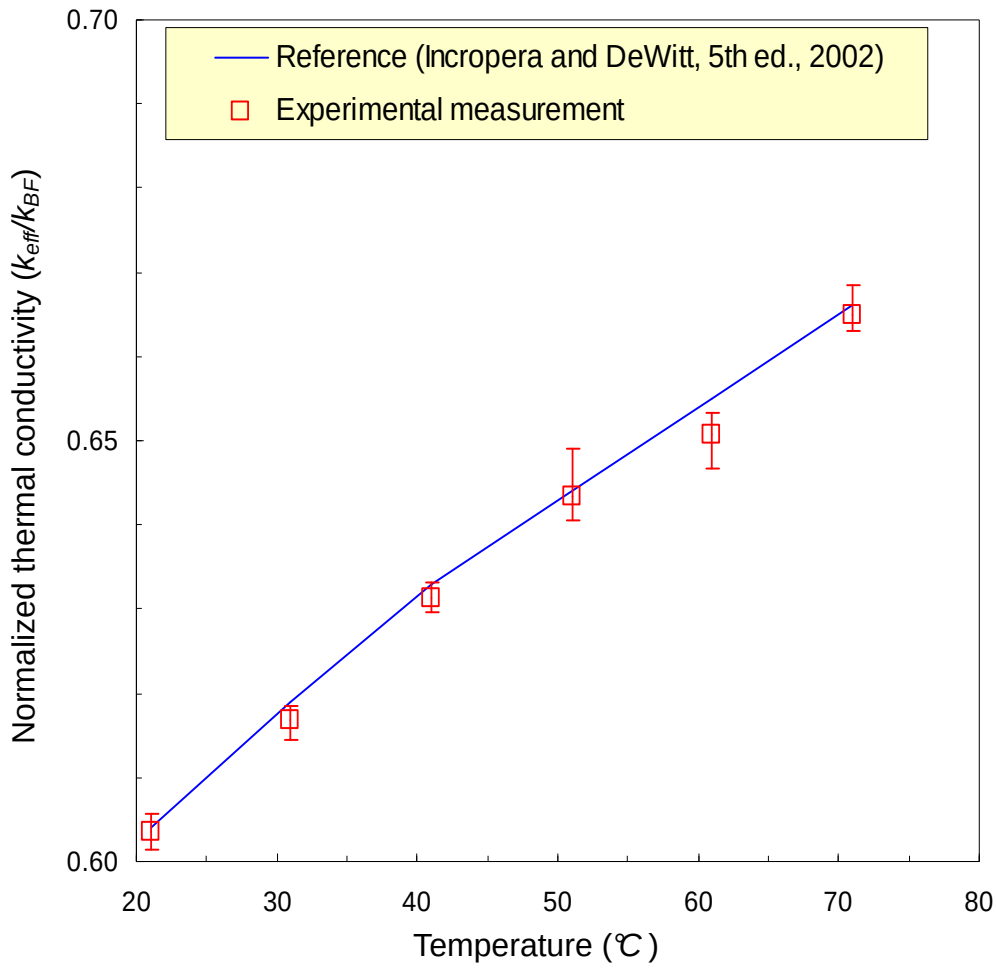

Figure 2-10. Thermal conductivity comparison of water reference data (line) with measurement results (square) over a temperature range of 21 °C to 71 °C with standard deviations (vertical lines in squares).

measured voltages and resistances of a voltage-divider circuit. These values are coupled, however, and cannot be used to calculate individual uncertainties. Therefore a perturbation technque is used for predicting uncertainties of heat flux and slope from measured errors. Table 2-3 lists the measured errors and Table 2-4 gives the uncertainties predicted from these measurement errors

The uncertainty from the ideal model of the thermal conductivity equation (Eq. 2-9) is about 2.5%, due mainly to the platinum wire end effect. With all uncertainties, the overall thermal conductivity measurement uncertainty is 3.19%. The uncertainty from the ideal model of the thermal conductivity equation (Eq. 2-9) is about 2.5%, due mainly to the platinum wire end effect. With all uncertainties, the overall thermal conductivity measurement uncertainty is 3.19%.

2.4 Experimental Conditions and Result

2.4.1 Sample preparation and test condition

Three nanofluid samples have been used for nanofluid thermal conductivity measurements: (1) 11-nm nominal diameter sample (Nanostructured & Amorphous

Table 2-3. Error ranges of measuring devices

	Precision error	System error
Voltage (V)	0.00756	0.0546% of reading
Resistance (Ω)	0.003	0.0001% of reading
Temperature (°C)	0.01	0.25

Table 2-4. Sources of uncertainty

	Measured value	Uncertainty	
		System, ε_{Bx}	Measurement, ε_{Px}
Supplied heat (W), q	0.9624	0.0005	0.0001
Wire length (m), l	0.090	0.001	0.001
Slope, S	1.2361	0.01486	0.0008

Materials Inc.), (2) 47-nm nominal diameter sample (Nanopahse Inc.), and (3) 150-nm nominal diameter (Nanostructured & Amorphous Materials Inc). The preparation of nanofluid must ensure proper dispersion of nanoparticles in the liquid. In the present experiment, ultrasonic vibration is used to mono-disperse the particles. To validate the average particle size, sonicated nanoparticles suspended in nanofluid samples have been visualized using a Transmission Electron Microscope (TEM) at 50000-magnification. The volume-weighted particle size distributions (Friedlander, 2000) are given in Figure 2-11. Volume-weighted average nanoparticle sizes are 12.92 nm, 49.47 nm, and 182.40 nm, respectively.

To evaluate the nanofluid control factors, three different factors are considered for Al_2O_3 nanofluids: temperature, particle size, and volume concentration. Temperature ranges are from 21ºC to 71ºC, which are controlled by placing test chamber inside a circulating thermal bath with ± 0.01ºC accuracy at each specified temperature. Nominal diameters of nanoparticle samples are 11 nm, 47 nm, and 150 nm with averaged volume-

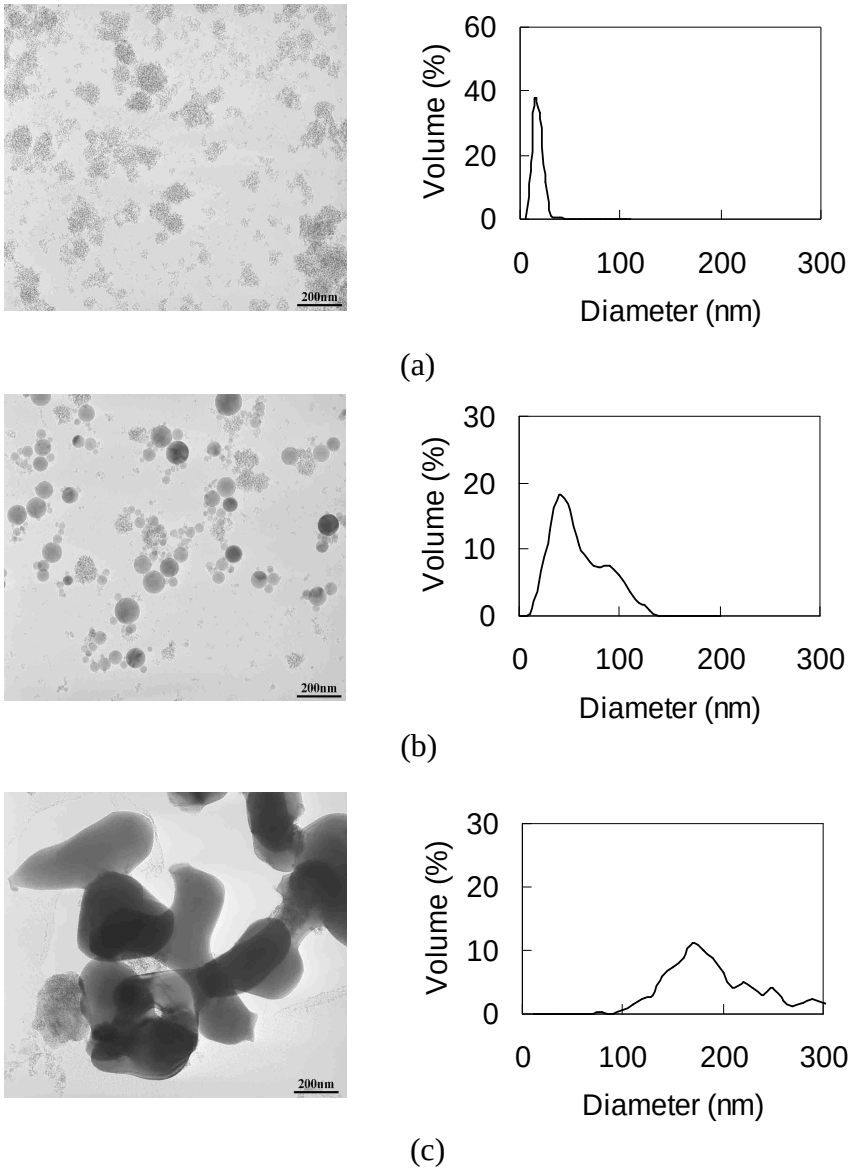

Figure 2-11 TEM photographs (50,000X) and volume-weighted particle size distributions of Al_2O_3 nanoparticles based on the equivalent diameter conversion: (a) 12.92-nm volume-weighted average diameter (11-nm nominal diameter by Nanostructured & Amorphous Materials Inc.), (b) 49.47-nm (47-nm nominal diameter by Nanophase Inc.), and (c) 182.40-nm (150-nm nominal diameter by Nanostructured & Amorphous Materials Inc.).

weighted diameters 12.92 nm, 49.47 nm, and 182.40, respectively. Volume concentrations are 1 vol.% and 4 vol.% for a 47 nm nanofluid sample.

2.4.2 Test result

Figure 2-12 shows the measured thermal conductivity depending on particle size, temperature, and volume concentration. The graph simply indicates the thermal conductivity of nanofluids as a function of particle size, volume concentration, and fluid temperature. Further interpretation is limited except for a quantitative assessment of how fast thermal conductivity is enhanced along each factor.

To arrive at a more physical explanation of the enhanced thermal conductivity mechanism, the data have been analyzed and expressed with empirical correlations of nanofluid thermal conductivity control factors.

To apply dimensional analysis to the thermal conductivity enhancement of nanofluids, the physical factors need to be identified. Here, the main factors chosen are temperature, particle size, and volume concentration. For the dimensional analysis, relevant properties are also selected and the thermal conductivity enhancements are expressed as a function of these parameters:

$$\frac{k_{eff}}{k_{BF}} = g\left(f, d_{BF}, d_p, k_p, k_{BF}, \mu_{BF}, \rho_{BF}, C_{p,BF}, T, l_{BF}, k_b\right) \qquad (2\text{-}12)$$

where f [-] is the volume concentration, d_{BF} [L] is the diameter of a base fluid molecule, d_p [L] is the diameter of a nanoparticle, k_p [$MLT^{-3}\Theta^{-1}$] is the thermal conductivity of a nanoparticle, k_{BF} [$MLT^{-3}\Theta^{-1}$] is the thermal conductivity of a base fluid,

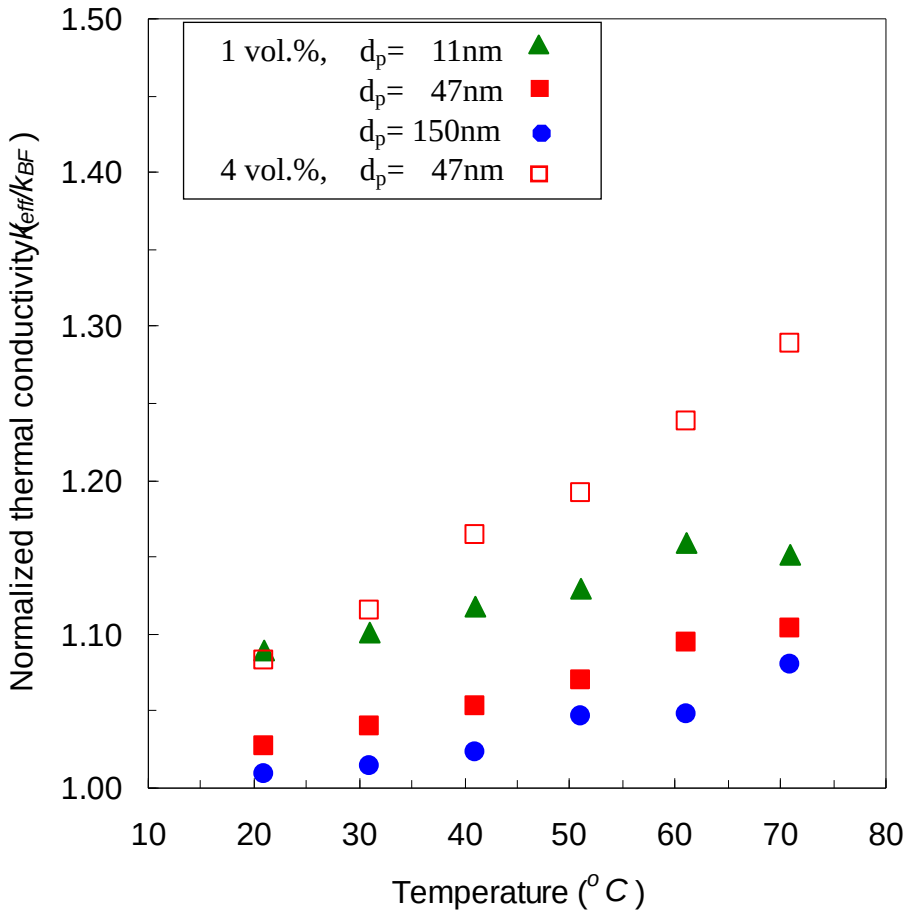

Figure 2-12. Temperature dependence of the thermal conductivity enhancement of three different Al_2O_3 nanofluids with 11-nm, 47-nm, and 150-nm sized nanoparticles at 1 and 4 vol.% concentration, normalized by the thermal conductivity of the base fluid at the specific temperature.

μ_{BF} [$ML^{-1}T^{-1}$] is the viscosity of a base fluid, ρ_{BF} [ML^{-3}] is the density of a base fluid, $C_{p,BF}$ [$L^2T^{-2}\Theta^{-1}$] is the specific heat of a base fluid, and T [Θ] is the base fluid temperature, l_{BF} [L] is mean free path of a base fluid molecule, and k_b [$ML^2T^{-2}\Theta^{-1}$] is the Boltzmann constant. Brackets indicate the parameter dimensions: L (Length), M (Mass), T (Time), and Θ (Temperature).

From the Buckingham-Pi theorem, 6 pi groups can be formed by power products since there are 10 variables and 4 dimensions. In this research, d_{BF}, k_{BF}, μ_{BF}, and T are designated as repeating variables. The final form of correlation is set up as

$$\frac{k_{eff}}{k_{BF}} = \frac{k_{enh}}{k_{BF}} + 1 = Const \cdot f^a \left(\frac{d_{BF}}{d_p}\right)^b \left(\frac{k_p}{k_{BF}}\right)^c Pr^d \, Re^e \tag{2-13}$$

The Prandtl number (*Pr*), and the Reynolds number (*Re*) are respectively defined as,

$$Pr \equiv \frac{\mu C_{p,BF}}{k_{BF}} \tag{2-14}$$

$$\mathrm{Re} \equiv \frac{\rho_{BF} U_{Br} d_p}{\mu_{BF}} = \frac{\rho_{BF} k_b T}{3\pi\mu_{BF}^2 l_{BF}} \tag{2-15}$$

where U_{Br} is defined as the Brownian velocity of nanoparticles based on the Einstein diffusion theory (Einstein, 1956):

$$U_{Br} \equiv \frac{k_b T}{3\pi\mu_{BF} d_p l_{BF}} \tag{2-16}$$

where k_b is the Boltzmann constant, 1.3807×10^{-23} *J/K*, and a constant value of 0.17 nm for the mean free path (l_{BF}) is used for water for the entire tested temperature range (Tien and Lienhard, 1971; Vincenti and Kruger, 1965).

For Eq. (2-13), one constant and five components can be obtained using a linear regression method of statistics with 95% confidence level as:

$$\frac{k_{eff}}{k_{BF}} = 1 + 64.7 \cdot f^{0.7460} \left(\frac{d_{BF}}{d_p} \right)^{0.3690} \left(\frac{k_p}{k_{BF}} \right)^{0.7476} Pr^{0.9955} Re^{1.2321} \qquad (2\text{-}17)$$

A detailed assessment of the Buckingham-pi theorem and linear regression scheme is given in Appendices A and B.

Figure 2-13 shows the empirical correlation equation for the enhanced thermal conductivity of nanofluids compared with experimental results. The emipircal correlation equation properly represents the experimental data.

Figure 2-14 shows the measured Al_2O_3 nanofluid thermal conductivity normalized by the base fluid conductivity at each specified temperature (symbols) and the experimental correlation of Eq. (2-17) (curves) for different nanoparticle sizes and volume concentrations. It is clearly seen that the nanofluid conductivity increases with increasing nanofluid temperature and with decreasing nanoparticle size. The gradually accelerating temperature dependence with increasing temperature is manifested as the slightly non-linear function of Eq. (2-17) for temperature. The only deviation from the empirical correlation comes from the 11-nm nanoparticles at 71°C. Agglomeration of particles is a possible cause since this effect becomes more severe for smaller nanoparticles (via increased surface area) and at higher temperatures (via higher particle activity).

The base fluid viscosity depends on temperature and can be expressed only in terms of temperature:

$$\mu_{BF} = A \cdot 10^{\frac{B}{T-C}} \qquad (2\text{-}18)$$

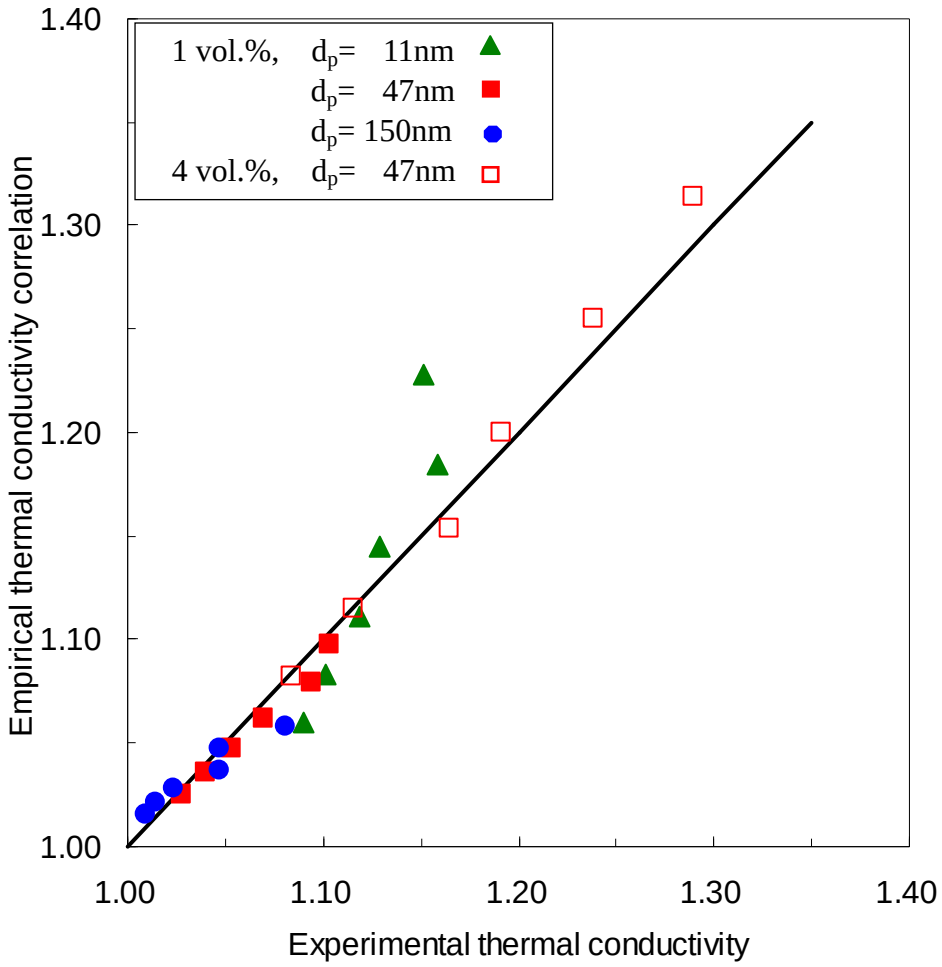

Figure 2-13. Comparison of the empirical correlation with experimental data for Al_2O_3 nanofluid thermal conductivity. The empirical correlation is determined by Buckingham-Pi analysis in association with a linear regression scheme with 95 % confidence level.

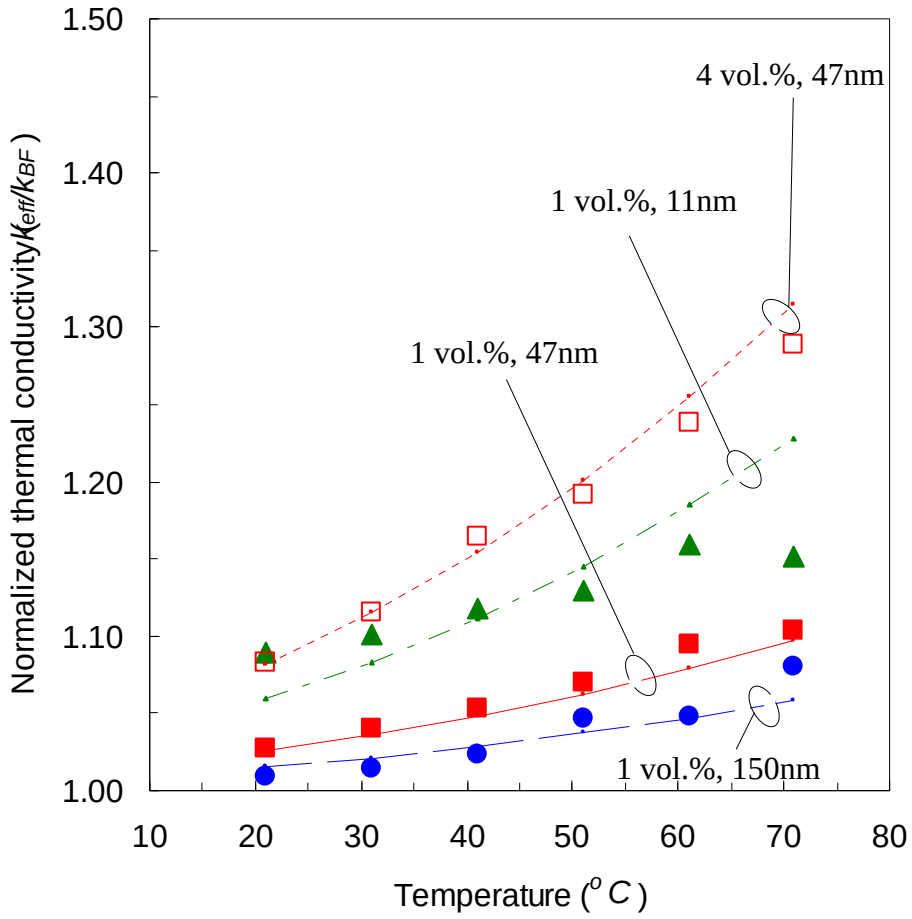

Figure 2-14. Temperature dependence of the thermal conductivity enhancement of three different Al_2O_3 nanofluids with 11-nm, 47-nm, and 150-nm sized nanoparticles at 1 and 4 vol.% concentration, normalized by the thermal conductivity of the base fluid at the specific temperature. Symbols represent experimental data and the corresponding curves represent empirical correlation, Eq. (2-17). At a fixed concentration, nanofluid conductivity increases with decreasing nanoparticle sizes and increases with increasing temperature.

where *A*, *B*, and *C* are constants, given as 2.414×10^{-5}, 247.8, and 140, for the case of water (Fox et al., 2004). The Brownian velocity also can be expressed as

$$U_{Br} \equiv \frac{k_b T}{3\pi\mu d_p l_{BF}} = \frac{k_b}{3\pi d_p l_{BF}} \cdot \frac{T}{A \cdot 10^{\frac{B}{T-C}}} \tag{2-19}$$

Under specified f and d_{BF}, and assuming constant k_p, constant ρ_{BF} for the tested temperature range, the correlation Eq. (2-17) can be rewritten exclusively in terms of nanoparticle diameter and suspension temperature as:

$$\frac{k_{eff}}{k_{BF}} = 1 + Const \cdot \left(\frac{\mathrm{Pr}(T)^{0.9955} T^{1.2321}}{d_p^{0.369} k_{BF}(T)^{0.7476} \mu^2} \right) = 1 + Const \cdot \left(\frac{\mathrm{Pr}(T)^{0.9955} T^{1.2321}}{d_p^{0.369} k_{BF}(T)^{0.7476} 10^{\frac{2.4642\,B}{T-C}}} \right) \tag{2-20}$$

where *Const* represents all specified or invariant experimental parameters.

Figure 2-15 shows the temperature dependence of the three primary parameters in Eq. (2-12), namely k_{BF}, *Pr*, and *Re* with the subscript *o* referring to the reference temperature of 21°C for the case of 47-nm nanoparticles at 1 vol.%. The Reynolds number that represents the mobility of nanoparticles shows dominating temperature dependence whereas *Pr* shows slightly decreasing dependency and k_{BF} shows practically no dependence on temperature. Note that the nanoparticle Brownian velocity (Eq. (2-15)) directly represents the nanoparticle mobility, or equivalently *Re*, as seen in Eq. (2-14).

By approximating the weak temperature dependence of kBF and Pr as invariant in Eq. (2-19), the empirical correlation can explicitly show the effects of nanoparticle size and nanofluid temperature as:

$$\frac{k_{eff}}{k_{BF}} = 1 + const \cdot \left(\frac{1}{d_p} \right)^{0.369} \left(\frac{T^{1.2321}}{10^{\frac{2.4642\,B}{T-C}}} \right) \tag{2-21}$$

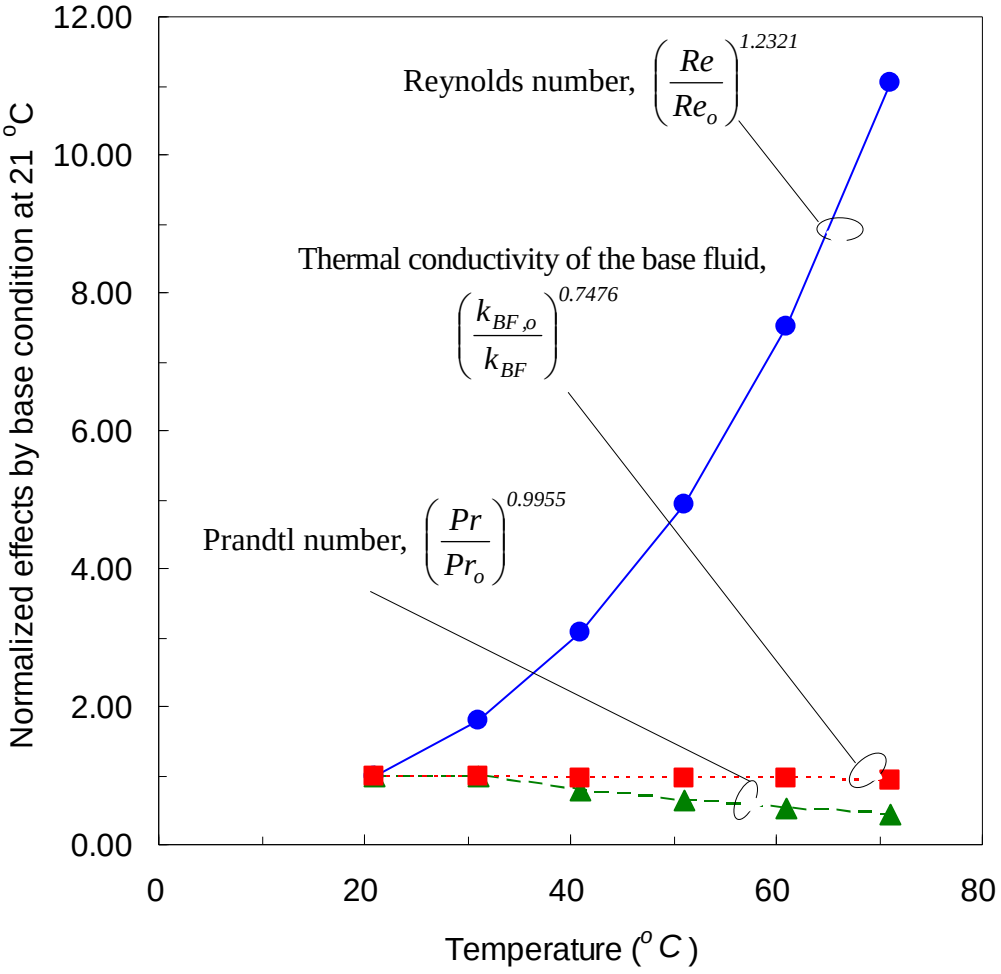

Figure 2-15. Comparison of temperature dependencies of the three primary parameters (k_{BF}, Pr, and Re) of the empirical correlation for the case of the Al_2O_3 nanofluid sample with 47-nm nanoparticles at 1 vol.% concentration. *Re* shows the dominating dependency on temperature while k_{BF} shows nearly negligible dependence on temperature and *Pr* shows slightly negative dependence on temperature. Therefore, the conjecture of the dominating role of nanoparticle Brownian mobility, embedded as Brownian velocity (V_{Br}) in *Re*, is experimentally validated.

Figure 2-16 shows the effect of the nanoparticle Brownian velocity as a most dominant function of temperature for a given particle size at the constant nanoparticle volume concentration, 1 vol.%.

2.5 Heat Propagation Velocity and Thermal Conductivity

Most theories of thermal conductivity enhancement are based on Brownian motion based on the kinetic theory, which well describes the thermal conductivity of gas as the gas molecules are assumed freely moving due to their relatively lean distributions (Carey, 1999). For liquids, however, their stronger intermolecular forces, primarily because of the higher packing density, will make it necessary to modify the kinetic theory. In addition, the molecular collision velocities of gases are too low to explain liquid thermal conductivities that are one or more order higher than the gas conductivities. Hence, the thermal conductivities of denser liquids were conjectured to be more properly expressed by the faster sound propagation for the case of liquids and the phonon velocity for the case of solids (Bird et al., 2002).

The enhanced thermal conductivity of a liquid suspension containing highly conductive metal particles, such as nanofluids with Al_2O_3 or CuO, is believed to be attributed to the interaction of nanoparticles with the base fluid molecules.

Henceforth, the thermal conductivity enhancement by the molecular interaction with nanoparticles can be given as (Bird et al., 2002):

$$\Delta k_{enh} \sim f \cdot \rho_p \cdot c_p \cdot U_{hp} \cdot l \tag{2-22}$$

where the heat propagation velocity U_{hp} represents the heat propagation rate by the

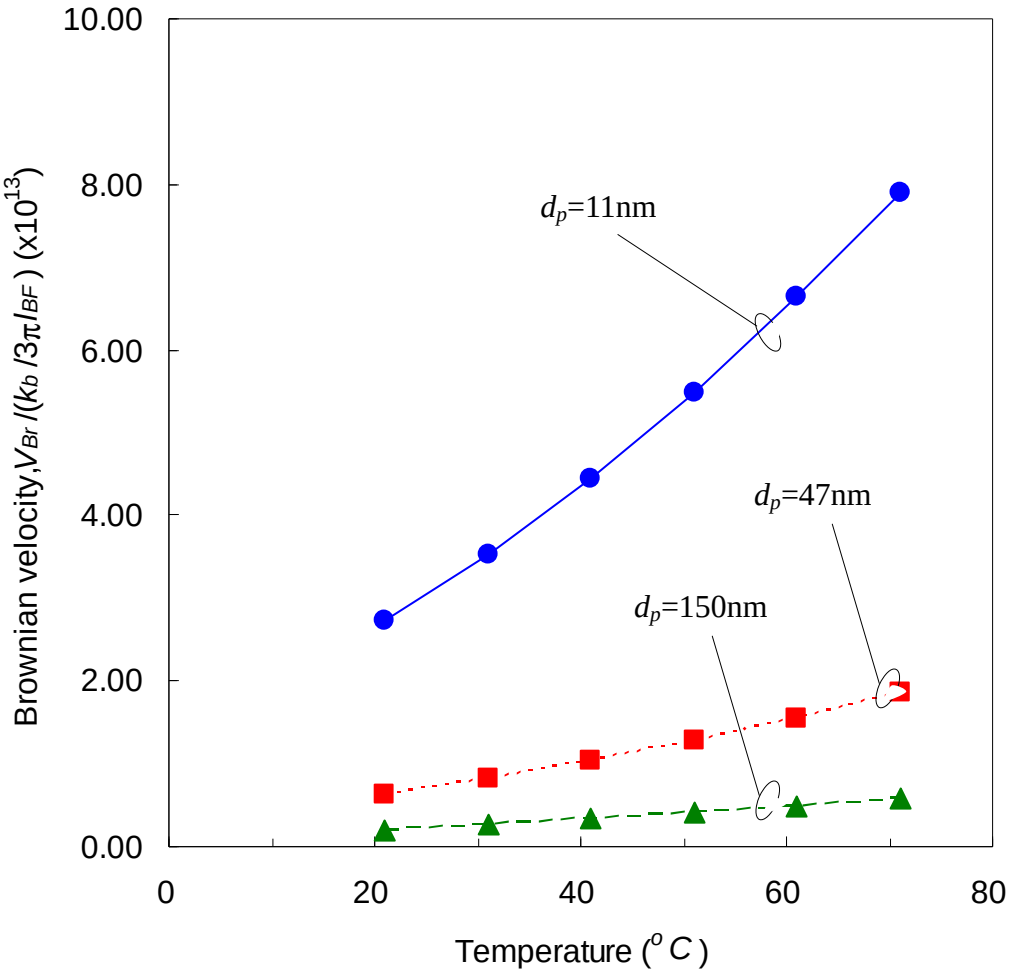

Figure 2-16. Correlation between the Brownian velocities and nanofluid temperature for different nanoparticle sizes for Al_2O_3 nanofluids at 1 vol.%. As expected, the Brownian velocities increase with increasing temperature and decreasing nanoparticle size, which is consistent with the temperature and nanoparticle size dependency of nanofluid thermal conductivity.

vibration of base fluid molecules, and the heat travel distance *l* is defined as the freely traveling distance of heat energy during the interaction of base fluid molecules and nanoparticles (Xuan et al., 2003) as:

$$l = C_1 \cdot \sqrt{\frac{T}{\mu d_p}} \tag{2-23}$$

where μ is the viscosity of the base fluid and C_1 is a proportional constant.

For example, for 47-nm Al_2O_3 at 1 vol. % concentration ($f \cdot \rho_p \cdot c_p \sim 3.2\times10^4$), the thermal conductivity enhancement Δk_{enh} is measured to range from 0.025 to 0.100 (Chon et al., 2005). Assuming *l* being the same order of magnitude as the mean free path of water molecules, i.e., *l* = 0.170 nm, the heat propagation velocity U_{hp} is estimated to be on the order of 10^3. Note that this estimation is persistent with the conjectures of the characterisitc heat propagation velocity being the scale of the sound propagation velocity in a colloidal medium (Bird et al., 2002; Keblinski et al., 2002)

In a stationary liquid, individual molecules are constantly moving and their motions are largely confined within a “cage” formed by the closely-packed neighboring molecules (Glasston et al., 1941). This virtual cage is conceived by the energy barrier of height $\Delta\tilde{G}_0^+ / \tilde{N}$ where $\Delta\tilde{G}_0^+$ is the molar free energy of activation for escaping from the cage and $\tilde{N}$ denotes the molar Avogadro number. The molecular vibrational frequency f_v is given as:

$$f_v = \frac{k_b T}{h} \exp\left(-\Delta\tilde{G}_0^+ / R_g T\right) \tag{2-24}$$

where h and R_g are the Planck constant and the specific gas constant, respectively,

and T is the fluid temperature. The free energy of activation, $\Delta\tilde{G}_0^+$, is assumed constant for a specified fluid and also assumed directly related to the internal energy of vaporization at the normal boiling point (Kincaid et al., 1941). The internal energy is given from the Trouton's rule (Digilov and Reiner, 2004) as, $\Delta\tilde{U}_{vap} \approx \Delta\tilde{H}_{vap} - RT_b \cong 9.4RT_b$:

$$\Delta\tilde{G}_0^+ \approx 0.408\Delta\tilde{U}_{vap} \cong 3.8RT_b \tag{2-25}$$

where $\Delta\tilde{H}_{vap}$ is the enthalpy of vaporization at the normal boiling point T_b. Combining Eqs. (2-24) and (2-25) gives an expression for the heat propagation velocity as:

$$U_{hp} = l_{hp} \cdot \frac{k_b T}{h} \exp\left(-3.8T_b/T\right) \tag{2-26}$$

where l_{hp} represents the heat propagation length scale. The heat propagation velocity can be estimated by examining the order-of-magnitudes of the involved parameters.

Figure 2-17 shows comparison of three different types of velocities used in nanofluidic thermal conductivity models to date: (1) heat propagation velocity of the present model, (2) the Brownian velocity of water molecules, and (3) three differently defined Brownian velocities for 47-nm Al_2O_3 nanoparticles (Jang and Choi, 2004; Kumar et al., 2004; Prasher et al., 2005).

The presently defined heat propagation velocity, Eq. (2-26), shares the same order of magnitude with the speed of sound and this is consistent with the conjecture of the sound velocity to use to describe thermal conductivities in liquid medium (Bird et al., 2002). Figure 2-17 also shows the phonon velocities for selected solid mediums of α–Fe and silicons.

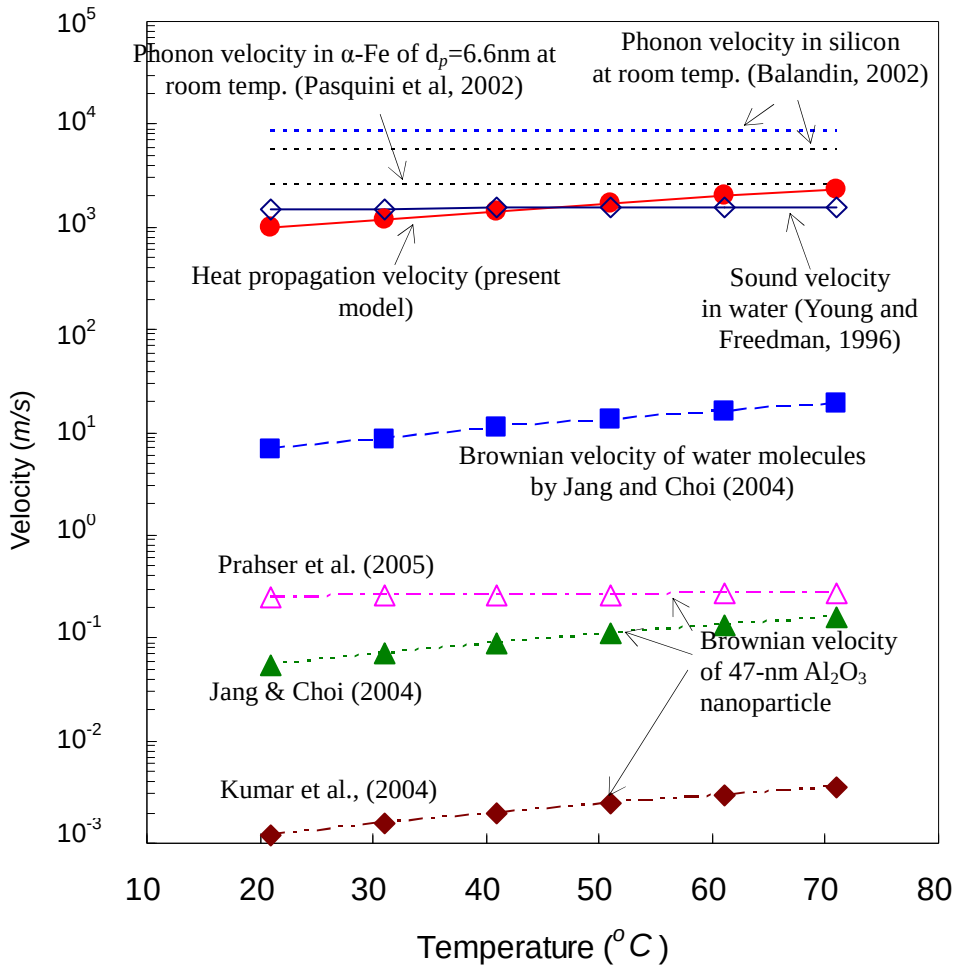

Figure 2-17. Temperature dependence of Brownian velocities of nanoparticles and water molecules (Jang and Choi, 2004; Kumar et al., 2004; Prahser et al., 2005), speed of sound in water (Young and Freedman, 1996), phonon velocities in selected solid mediums (Balandin, 2002; Pasquini et al, 2002), and the present modeled heat propagation velocity.

The phonon velocities are expected to be faster than the heat propagation velocity in liquid because of the relatively higher heat conductivities in solid mediums.

Substituting Eqs. (2-26) and (2-23) into Eq. (2-22) gives:

$$\frac{k_{eff}}{k_{BF}} = 1 + C \cdot \frac{f\rho_p c_p}{k_{BF}} \cdot \frac{\lambda_{ht} k_b T}{h} \exp\left(-3.8 T_b / T\right) \cdot \sqrt{\frac{T}{\mu d_p}} \tag{2-26}$$

where C is a proportional constant. Further modifications of Eq. (2-26) are implemented to account for both the nanoparticle heat dissipation to the surrounding liquid and the effect of nanoparticle coagulation. Nanoparticle heat dissipation into the base fluid medium is known to affect the effective thermal conductivity (Wilson et al., 2002; Ge et al, 2004), and the heat dissipation time increases with increasing nanoparticle heat capacity and decreases with increasing heat capacity of the surrounding fluid. In other words, nanoparticles with higher heat capacity require longer heat dissipation time to the base fluid and this results in slower thermal diffusion and lower effective thermal conductivity.

In additioin, nanoparticle coagulation is inevitable to an extent and the coagulation becomes generally more severe with increasing particle concentrations. According to Keblinski et al. (2002), the surface to surface distance of nanoparticles are two times of particle size at 1 vol. %, however, it can decrease to half of particle size at 5 vol. %. The coagunlation of nanoparticles can effectively decrease the volume concentration to f^a with a being less than unity. Therefore the effective thermal conductivity of nanofluids of Eq. (2-26) is modified as:

$$\frac{k_{eff}}{k_{BF}} = 1 + C \cdot \frac{f^a \rho_p c_p k_b T^{1.5}}{k_{BF} h \cdot \mu^{0.5} d_p^{0.5}} \exp\left(-3.8 T_b / T\right) \cdot \left(\frac{C_{p,BF}}{C_{p,p}}\right)^b \tag{2-27}$$

where $C_{p,BF}$ is the base fluid specific heat. The superscripts *a* and *b* are empirical constants that represent the effect of nanoparticle coagulation and the effect of nanoparticle heat dissipation, respectively. A regression analysis of the experimental data in previous section (Chon et al., 2005) determines $a = 0.70$, $b = 1.5$, and $C = 1.33 \times 10^{-25}$ for the case of Al_2O_3 (11-nm, 47-nm, 150-nm diameters) nanoparticles in water under various experimental conditions of volume concentrations from 1 to 4 vol. % and the tested temperature range from 21 to 71 °C.

Figure 2-18a shows the predictions based on the present model (the solid line) in comparison with the published four different models for the case of 47-nm Al_2O_3 at 1 vol. % in water. The symbols show the corresponding experimental data (Chon et al., 2005). The Xuan et al. (2003) excessively overestimates and their model shows the limitations of the simple modification of the Maxwell's model (1904) to apply for nanofluids. The Jang and Choi's model (2004) shows closeness with experimental data up to about 50°C and substantially deviates thereafter. The deviation beyond 50°C is believed attributing to their incorrect postulation in determining the Nusselt number as previously pointed out. The model by Kumar et al. (2004) wrongly postulates the mean free path of the base fluid and completely fails to predict nanofuidic thermal conductivities.

The model by Prahser et al. (2005) shows good aggreement with the experiment for the case of Al_2O_3 nanofluid as shown in Figure 2-18a. However, for the case of CuO nanofluid (Figure 2-18b) their model breaks down showing excessive underestimation of the corresponding experimental data presently taken by the authors.

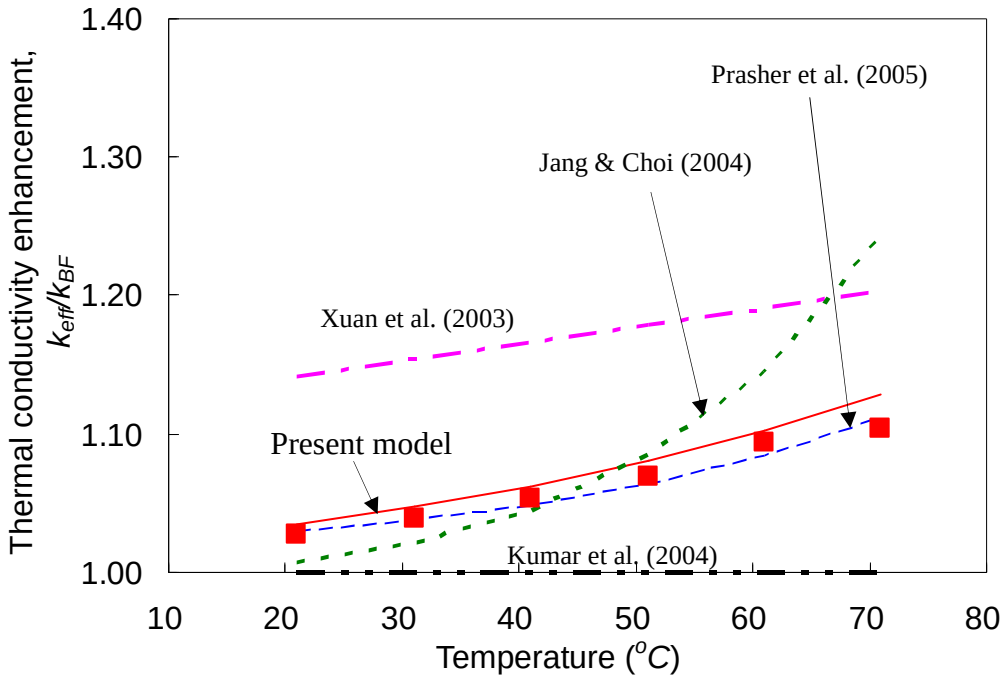

(a) 1 vol. % 47-nm sized Al_2O_3

Figure 2-18. Comparison of the present model (solid curves) with published models (Xuan et al., 2003; Jang and Choi, 2004; Kumar et al., 2004; Prasher et al., 2005) for nanofluidic thermal conductivity enhancement. The symbols represent the corresponding experimental data: (a) 1 vol. % Al_2O_3 nanofluid (Chon et al.), and (b) 1 vol. % CuO nanofluid (present experiment).

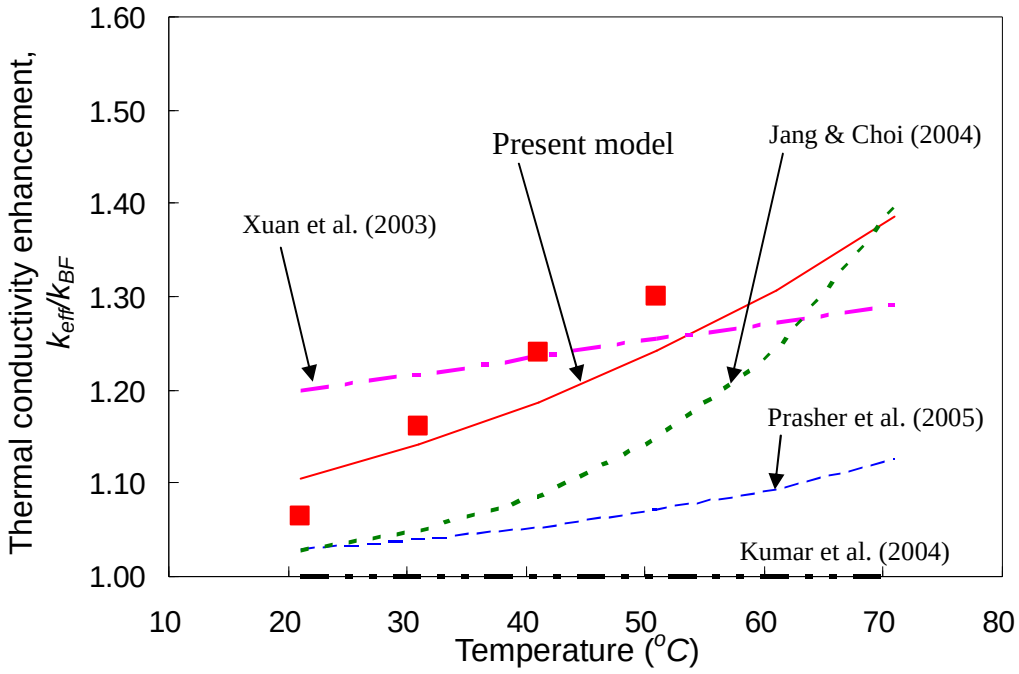

(b) 1 vol. % 30-nm sized CuO

Figure 2-18. Continued

Their model inherently lacks the dependency of the material properties of nanoparticles other than incorporating their sizes and concentrations. Jang and Choi (2004) also shows large discrepancies possibly because of the same reason of incomprehensive parametric dependency. Xuan et al. (2003) does not show agreeable temperature dependency, and Kumar et al.'s model (2004) does not show any physically meaningful representation. The present model of Eq. (2-27) shows fairly good agreement comprehensively for both nanofluids and for all the tested conditions of temperatures and volume concentrations.

Figure 2-19 shows the comparison of the theoretical predictions for nanofluid thermal conductivities based on the present model with published experimental data for both Al_2O_3 and CuO nanofluids (Lee et al., 1999; Das et al, 2003; Chon et al., 2005). The present model shows persistently good agreement with all the available experimental data, and thus, the model is considered more comprehensive than any of the previously published models.

2.6 Conclusion

In an effort to understand the mechanism of thermal conductivity enhancement in nanofluids, systematically prepared thermal conductivity measurements have been conducted with three different fairly mono-dispersed Al_2O_3 nanofluid samples: 11-nm, 47-nm, and 150-nm, and thermal conductivity has been predicted theoretically.

Based on experimental results, the empirical correlation of nanofluid thermal conductivity has been derived using the Buckingham-pi theorem and a linear regression scheme to evaluate the each control factor for nanofluid thermal conductivity enhancement. The most important finding from the experiments is the effect of the

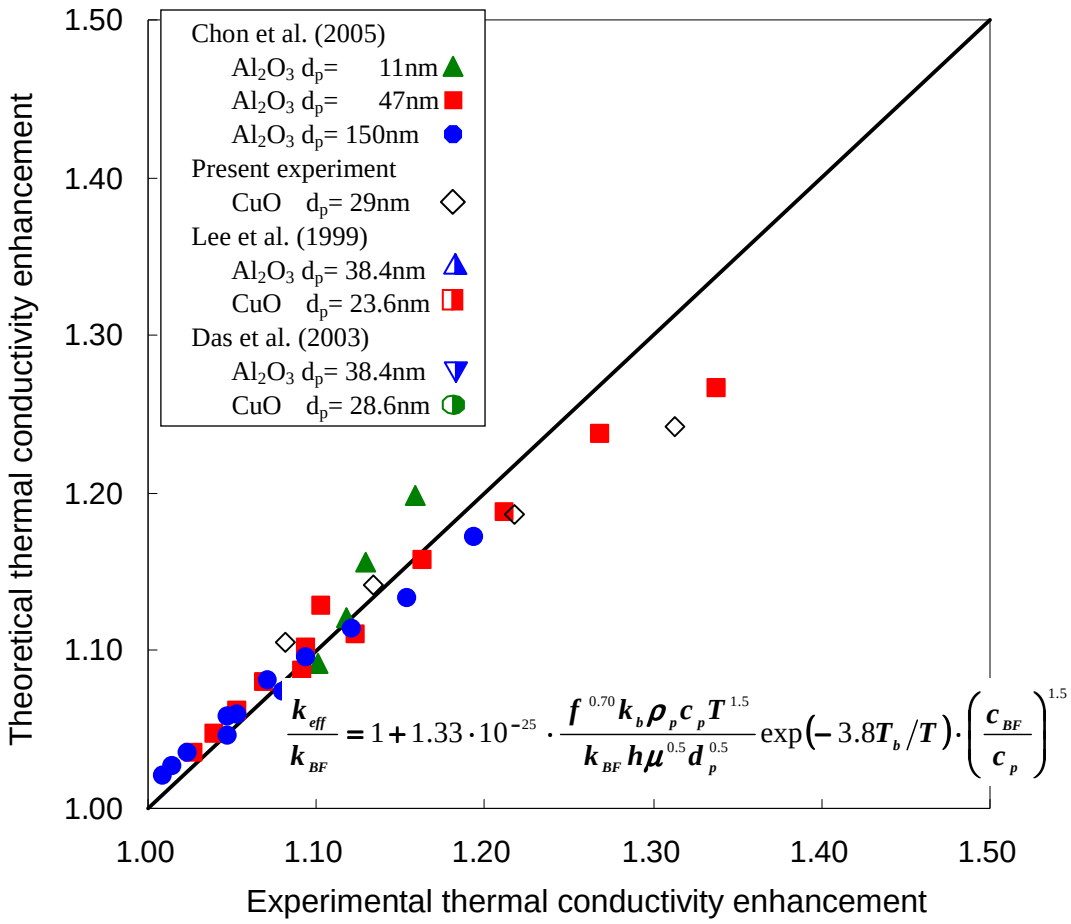

Figure 2-19. Predictions of the present model with corresponding experimental data (Lee et al., 1999; Das et al, 2003; Chon et al., 2005) for various Al_2O_3 and CuO nanofluid samples (Lee et al., 1999; Das et al, 2003; Chon et al., 2005). The present model associates with the experimental data with 95 % confidence level.

Brownian velocity that is single most dominant function of temperature for a given particle size (Figures. 2-15 and 2-16).

This Brownian velocity was theoretically conjectured as a key role in determining the temperature effect on nanofluid thermal conductivity enhancement in a previous study. The present study validates the conjecture by experimentally showing that the mobility of nanoparticles, which includes temperature dependency, is the most dominating factor for the thermal conductivity enhancement of nanofluids. Therefore, it can be stated that at higher temperature, the nanofluid thermal conductivity increases primarily as a result of increasing nanoparticle Brownian motion.

However, Brownian motion itself is very slow compared to heat transfer velocity and nanofluid thermal conductivity needs more fundamental cause to explain its enhancement. In theoretical approach, the propagation velocity is newly introduced for describing properly fast heat transfer of a nanofluid, which is order of sound velocity of a base fluid and comparably faster than the Brownian velocity. As shown in Figures 2-18 and 2-19, the present model predicts experimental results well and shows persistently good agreement with all the available experimental data. It is evidenced that the new model based on the faster heat propagation velocity, in association with the modifications for both nanoparticle heat dissipation and coagulation, can more accurately and comprehensively describes the effective nanofluidic thermal conductivities.

CHAPTER 3

THERMALLY DRIVEN NANOPARTICLE MOBILITY

3.1 Objective

Even though a significant research effort has been committed to exploring the mechanism of nanofluid thermal conductivity enhancement, the fundamental mechanism has not yet been revealed. As we studied in the previous chapter, the final result is to define the key control factors of enhancing thermal properties such as particle size, temperature, and volume concentration. The Brownian motion is expected to be most dominant in thermal conductivity enhancement of nanofluids. However, we do not know how these factors are working or how Brownian motion affects the thermal conductivity enhancement. According to Keblinski et al. (Keblinski et al., 2002; Evans et al., 2006), the thermal diffusion is several orders higher than Brownian diffusion and this Brownian diffusion is not said to directly enhance the nanofluid thermal conductivity. On the contrary, other research groups (Jang and Choi, 2004; Krishnamurthy et al., 2006) proposed micro convection which has a higher thermally driven motion compared to Brownian motion's thermal diffusion.

Besides Brownian motion, there exists another typical thermally driven motion called thermophoretic motion, which is in the temperature gradient field. Because every thermal and heat transfer system as well as thermal conductivity measurement system experiences a temperature gradient field, nanoparticles in it move from the high temperature to cold region, regardless of the temperature gradient intensity. This can

introduce highly active thermal motion between base fluid molecules and surrounding nanoparticles and may increase micro convective motion around nanoparticles to enhance thermal conductivity (Jang and Choi, 2004; Krishnamurthy et al., 2006).

Both thermally driven Brownian and thermophoretic particle motions are important for nanofluidic thermal conductivity enhancement (Buongiorno, 2006). While the study for Brownian motion have been actively conducted (Jang and Choi, 2004; Kumar et al, 2004; Xuan et al., 2003; Prasher et al., 2005; Krishnamurthy et al., 2006), thermophoretic motion has rarely been studied and for nanoparticles no thermophoretic studies have been conducted. Therefore, in this chapter, nanoparticle thermophoretic motion has been experimentally studied to give a guide for further research for revealing the mechanism of nanofluid thermal conductivity enhancement by micro convective heat transfer of thermally driven particle motions.

3.2 Thermophoretic Particle Motion

The atoms or molecules that make up a liquid or gas are in constant thermal motion, and their velocity distribution is determined by the temperature of the system. The motion of the molecules of the fluid, due to the fact that the fluid contains heat, causes the molecules to strike the suspended particles at random. The impact makes the particles move. The net effect is an erratic, random motion of the particle through the fluid called ‘Brownian motion’ (Brown, 1966; Einstein, 1905, 1956; Perrin, 1990). When the small particles are in a temperature gradient field, particles are subject to the unbalanced impacts of the media atoms or molecules and it drives the particles towards

the cold end of the temperature gradient from regions of higher temperature. Figure 3-1 indicates particle movement by thermophoresis.

Over a century ago, Tyndall (1870) observed that dust particles suspended in a gas with inhomogeneous temperature tend to move out of the hot regions. This constitutes constituted the pioneering experimental study of thermophoresis in a gas. Fifty years later, Einstein (1924) and Cawood (1936) made theoretical analyses based on kinetic theory of gases for particles with small size compared with the mean free path of gas, that is $Kn >> 1$. Waldman (1959) and Bakanov and Derjaguin (1959) improved the analyses of the free molecule regime. For the free molecule regime, $Kn >> 1$ the thermophoretic velocity can be calculated from the kinetic theory (Waldman and Schmitt, 1966) as independent of particle size

$$U_{th} = -\frac{3\nu\nabla T}{4T(1+\pi C_a/8)} \tag{3-1}$$

where C_a, the accommodation coefficient, is usually about 0.9, ν is the kinematic viscosity, and T is the fluid temperature at the particle center if the particle were not there.

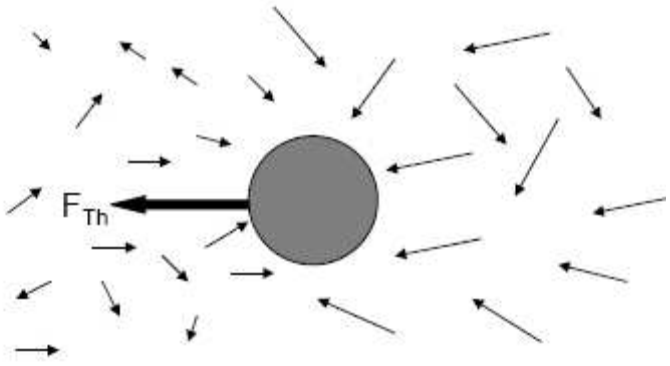

Figure 3-1. Schematic of the physical process causing a thermophoretic force

For the larger particle than the mean free path, $Kn << 1$ with assumptions of small Reynolds and Peclet numbers and taking into account the temperature jump, frictional slip, and thermal slip at the particle surface, the thermophoretic velocity of an isolated aerosol particle in a constant temperature gradient was derived by Brock (1962) as

$$U_{th} = -\frac{2\nu C_s (1+\kappa^* C_t Kn)}{(1+2C_m Kn)(2+\kappa^* + 2\kappa^* C_t Kn)} \frac{\nabla T}{T} \tag{3-2}$$

where κ^* is the thermal conductivity of particle normalized with that of the fluid, and C_t, C_s, and C_m are the dimensionless thermal slip, temperature jump, and frictional slip coefficients, respectively, at the particle surface. A set of well accepted values for C_t, C_s, and C_m is 1.14, 1.17, and 2.18, respectively (Talbot et al., 1980). Figure 3-2 (Friedlander, 2000) shows the calculation of the thermophoretic velocity based on presented equations.

Some research has been published concerning the temperature gradient effect in liquid, however, almost all of these experiments concentrated on thermal diffusion and qualitative studies. Putnam and Cahill (2005) studied nanoscale latex spheres in a temperature gradient field but only focused on thermodiffusion and Soret coefficients.

Nambu et al. (2004) published polymer pattern formation under a temperature gradient by micro convection based on natural convection. Rusconi et al. (2004) researched thermal lensing measurement of particle thermophoresis in aqueous dispersions focused on measurement of the Soret coefficient similar to Parola and Piazza (2004). McNab and Meisen (1973) uniquely derived the thermophoretic velocity in liquid as mentioned by Buongiorno (2006). In liquid thermophoretic motion, the velocity is a function of the temperature and temperature gradient of the flow field and is independent

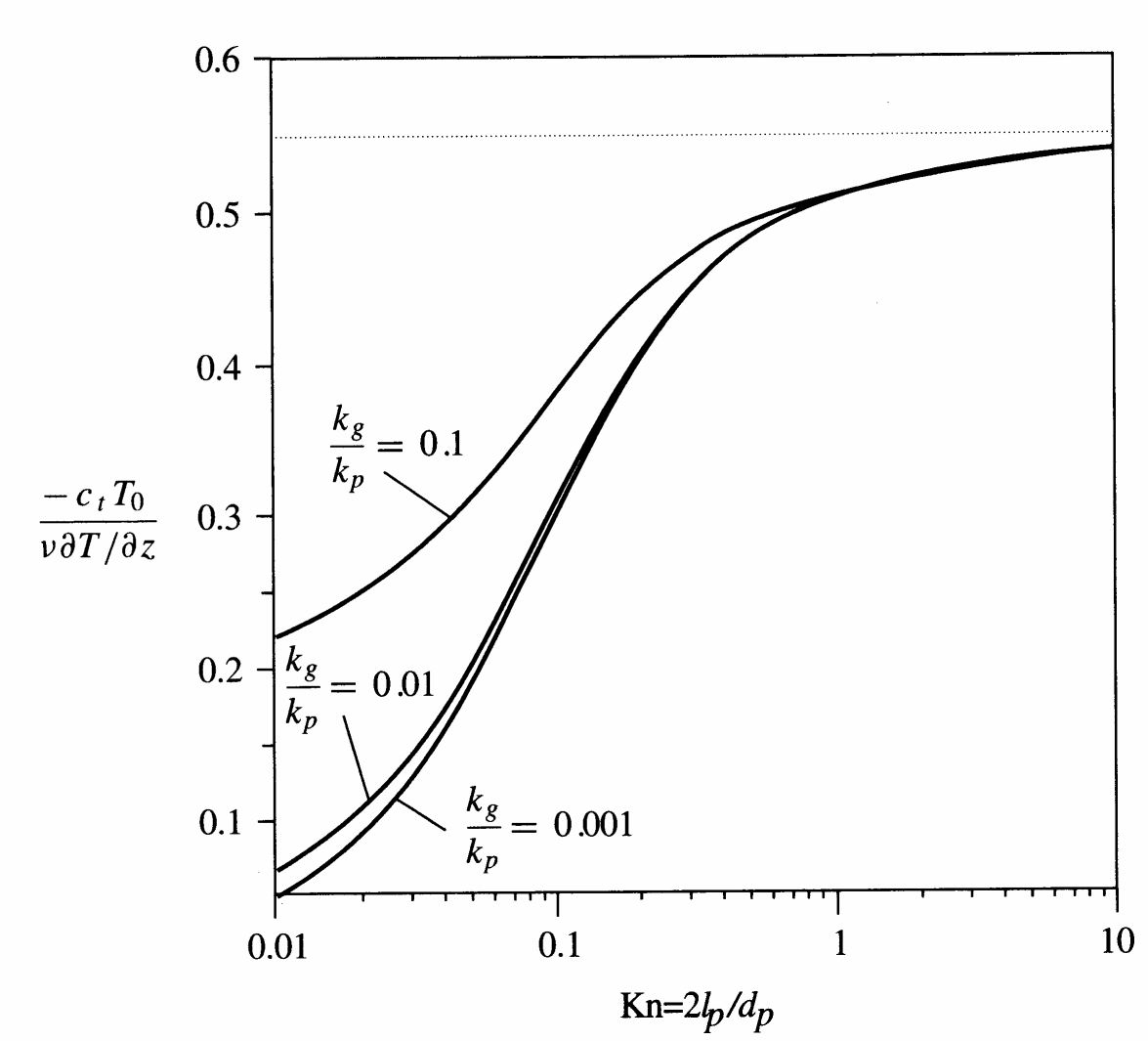

Figure 3-2. Dimensionless thermophoretic velocity calculation from Eq. (3-2) (Friedlander, 2000)

of particle size. The effect of suspended particles is negligible. The empirically derived thermophoretic velocity in liquid by McNab and Meisen (1973) is expressed as

$$U_{th} = -\lambda \frac{k_{BF}}{2k_{BF} + k_p} \frac{\mu}{\rho} \frac{\nabla T}{T} \tag{3-3}$$

where λ is an empirical numeric value of 0.26.

3.3 Experimental Setup

3.3.1 Particle Image Velocimetry

Thermo-fluidic areas are one of the most difficult areas to understand because thermal and fluid pheonomena are difficult to understand without conceptual visualization, however, the associated thermal processes are invisible to human eyes. Consequently, visualization methods play an important role in grasping such concepts. In thermal fluid sciences, the understanding of the physical thermal/flow processes can be greatly improved if the flow pattern of interest can be visually observed. For quantitative flow visualization techniques, a flow is visualized by seeding the fluid with small particles that follow the instantaneous changes of the flow, which is most widely named Particle Image Velocimetry (PIV).

The PIV technique consists of seeding particles, illumination light, image recording system, and optical devices. In most cases, tracer particles are added into the object flow field. These particles are illuminated in a plane of the flow at least twice within a short time interval. Light emitted from glowing particles are recorded on a sequence of frames. A digitized video recording system stores particle images in the

computer and the displacement of the particles can be calculated by mathematical post-processing techniques. Figure 3-3 shows a typical set-up for PIV recording in a wind tunnel (Raffel et al., 1998).

For calculation of particle velocity, an image is divided in small sub-areas called "interrogation windows". The overall velocity of a flow field is statistically calculated based on the local displacement vector of tracer particles for two consecutive images, which is determined for each interrogation window by means of statistical methods such as auto-correlation and cross-correlation (Adrian, 1988 and 1991; Kearne and Adrian, 1990 and 1992). It is assumed all particles in one interrogation window move homogeneously.

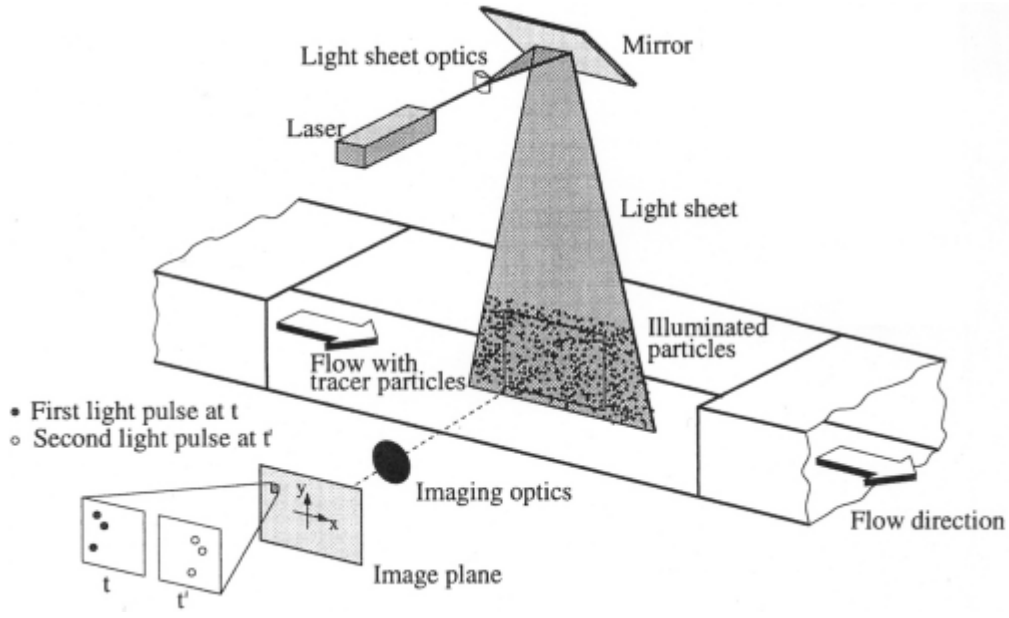

Figure 3-3 Typical set-up for PIV recording in wind a tunnel (Raffel et al., 1998).

3.3.2 Experimental setup

As shown in Figures 3-4 and 3-5 the experimental apparatus consists of a cylindrical optical tube to contain the fluid and seeding particles, hot and cold plates, an a Ar-ion laser, a pair of lenses, and a digital CCD to record particle movements. To improve the visibility, small windows were placed on the optical tube, which has an inner diameter of 1 inch. Top and bottom plates are fit into the optical tube with a distance of 1.3mm and are maintained at a set temperature by precisely controlled thermal baths. To avoid natural convection, the lower plate is maintained at a lower temperature than the upper plate (Incropera and DeWitt, 2002). A pair of plane-concave and convex lenses was were arranged to make a thinner light sheet. Seeding particles were three sizes of carboxilated fluorescent (Invitrogen Inc.) particles: 100 nm, 200 nm, and 500 nm. The particles were excited by an Ar-ion laser with 488 nm wavelength and re-emitted light with 512 nm wavelength which was recorded through a Hamamatsu EM CCD camera (C8800).

3.4 Experimental Conditions and Result

3.4.1 Samples and experiment condition

Three different nanometer sized particles of 100nm, 200nm, and 500nm were dispersed into distill water. The nanoparticles were carboxylated fluorescent particles with a specific gravity of 1.05 and were excited by a light of 488nm wavelength and re-emitted at 512 nm. Ar-ion laser of 488 nm wavelength generated light to illuminate the nanoparticles and formed a laser sheet by the combination of plain-concave and convex

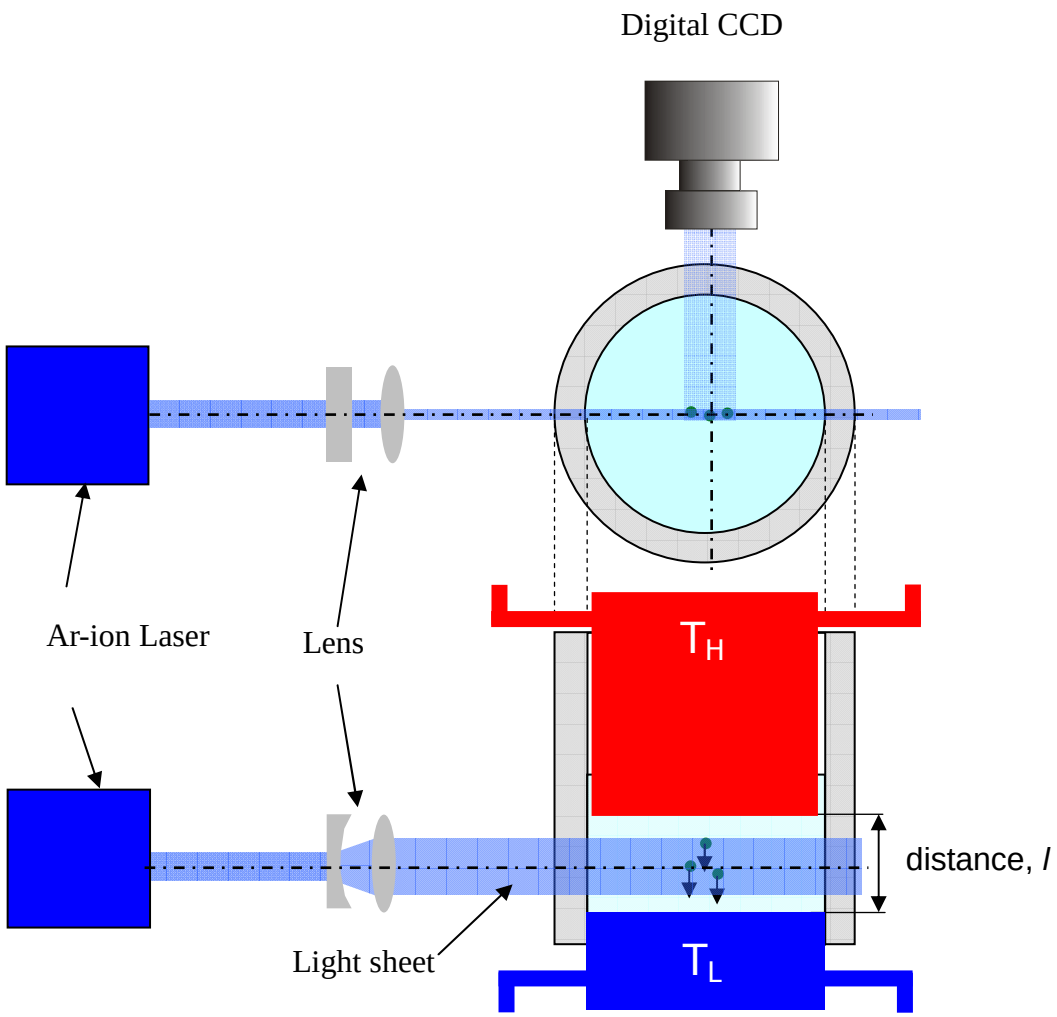

Figure 3-4 Diagram of experimental set-up

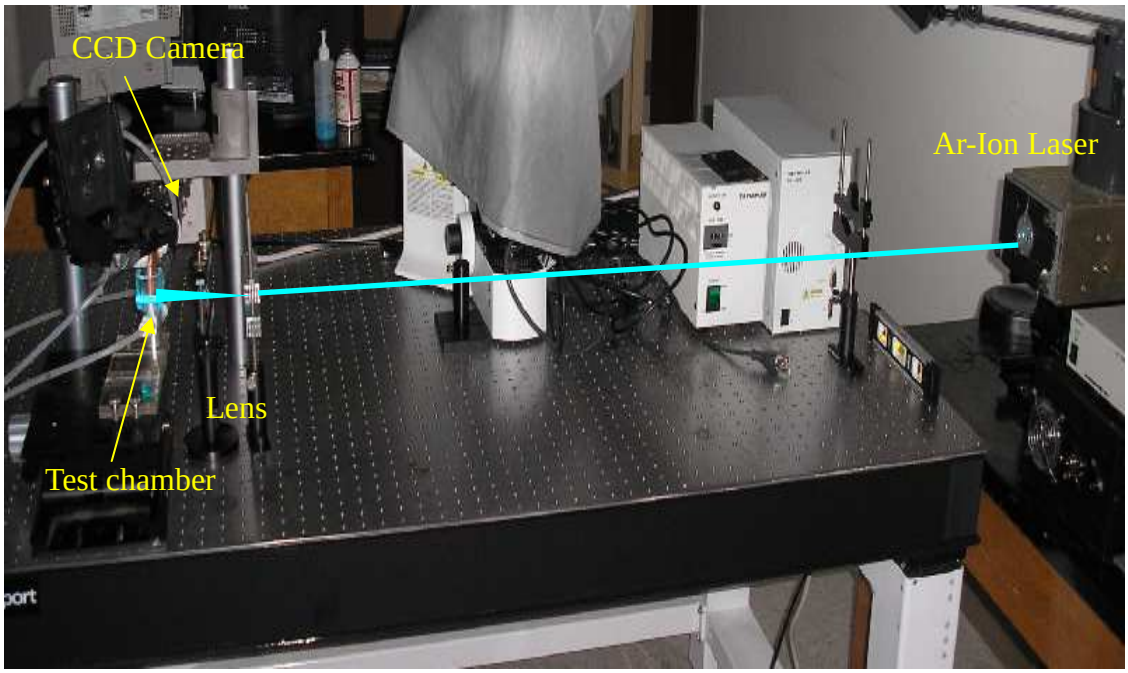

(a)

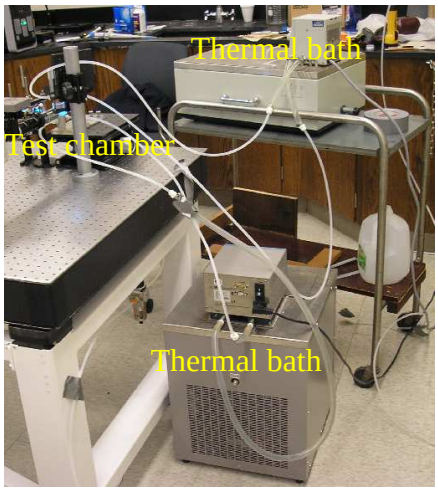

(b)

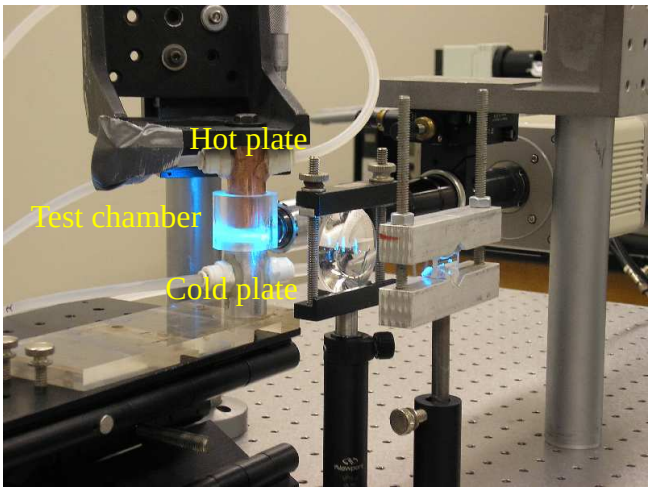

(c)

Figure 3-5 Photographs of experimental set-up: (a) Overview of experimental set-up, (b) thermal baths to maintain constant temperatures of upper hot and lower cold plates, (c) hot and cold plate installation in the test chamber.

lenses. A digital Hamamatsh EM CCD (C8800) recorded the illuminated particle images on the laser sheet with 5~10 frames per second. The image size was 2.2mm x 2.2mm with 1k x 1k pixel resolution. A pair of cold and hot plates generated three different temperature gradients: 100 K/cm, 200 K/cm, and 300 K/cm by thermally controled water baths. When the upper plate tempeature was higher than the lower, there was no flow motion. In other words, temperatures were stratified along the elevation. Therefore, the temperature in the flow field could be simply calculated. For the comparison with published data of McNab and Meisen (1973), a temperature of 303K was chosen at three different temperature gradients.

Digitized image information stored in a computer was analyzed by the PIV-Sleuth© (Christensen et al., 2000), PIV software to calculate particle velocity of each image within a 64k x 64k interrogation window. With coding and TechPlot®, each velocity vector was ensemble-averaged along the elevation for each temperature gradient.

3.4.2 Test result

Figures 3-6 to 3-8 show captured images of downward nanoparticles under thermophoretic temperature gradients of 100 K/cm, 200 K/cm, and 300 K/cm for three different nano-meter sized particles: 100-nm, 200-nm, and 300-nm. Because the upper plate is hotter than the lower plate for minimizing natural convection, particles are pushed from the hotter base fluid molecules to those of the colder region and generate a downward stream. The velocity of nanoparticles was calculated using the PIV-Sleuth, PIV analysis program, ensemble-averaged using an in-house program, and expressed as numeric values.

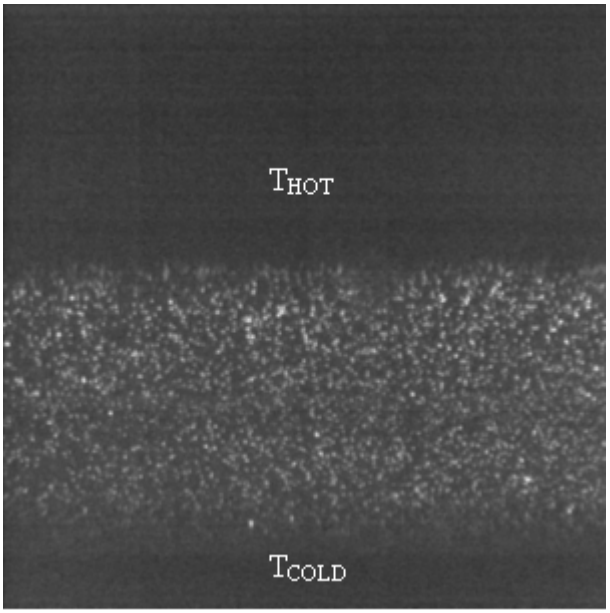

(a) $\Delta T/\Delta x$ = 100 K/cm

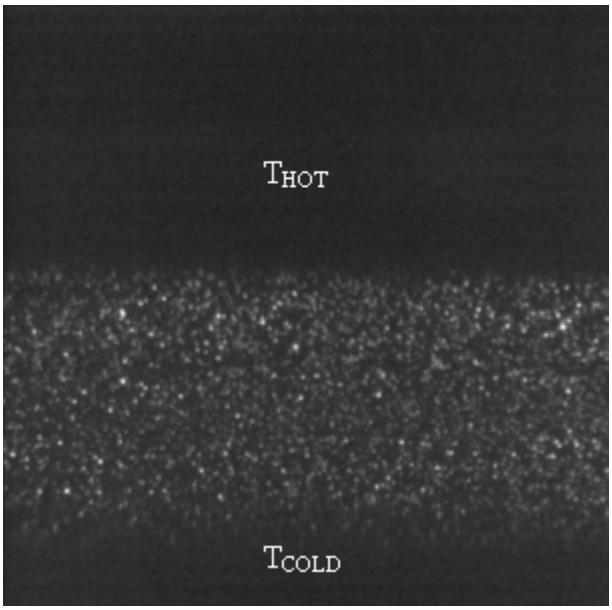

(b) $\Delta T/\Delta x$ = 200 K/cm

Figure 3-6. Photographic images of thermophoretically moving particles of 500-nm diameter at different temperature gradients: (a) $\Delta T/\Delta x$ = 100 K/cm, (b) $\Delta T/\Delta x$ = 200 K/cm, and (c) $\Delta T/\Delta x$ = 300 K/cm.

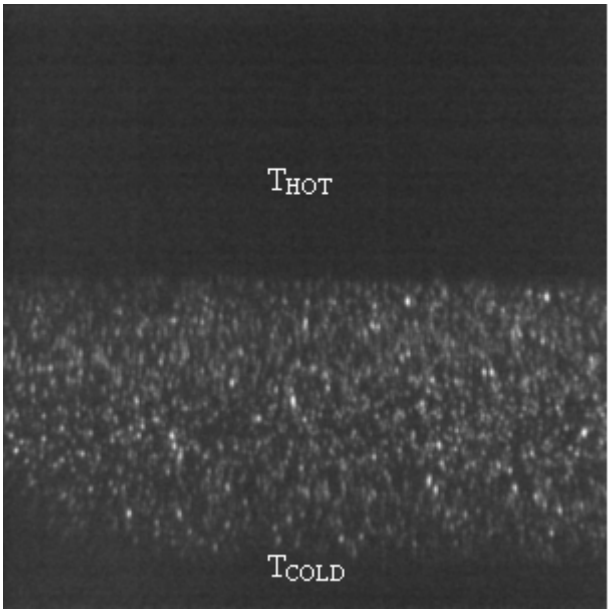

(c) $\Delta T/\Delta x$ = 300 K/cm

Figure 3-6. Continued

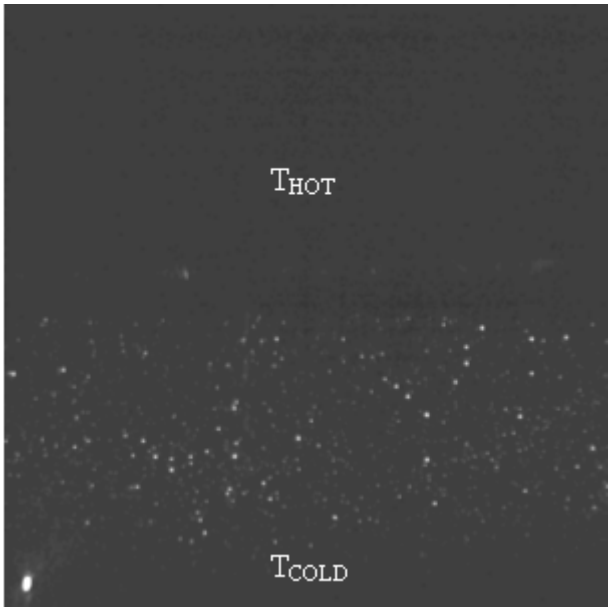

(a) $\Delta T/\Delta x$ = 100 K/cm

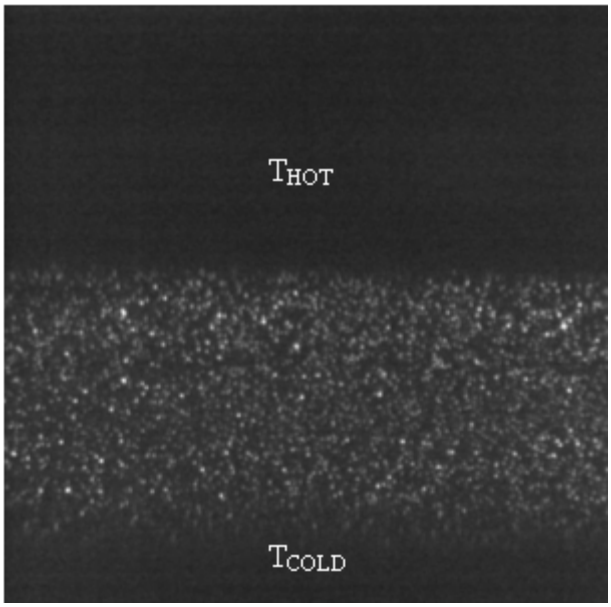

(b) $\Delta T/\Delta x$ = 200 K/cm

Figure 3-7. Photographic images of thermophoretically moving particles of 200-nm diameter at different temperature gradients: (a) $\Delta T/\Delta x$ = 100 K/cm, (b) $\Delta T/\Delta x$ = 200 K/cm, and (c) $\Delta T/\Delta x$ = 300 K/cm.

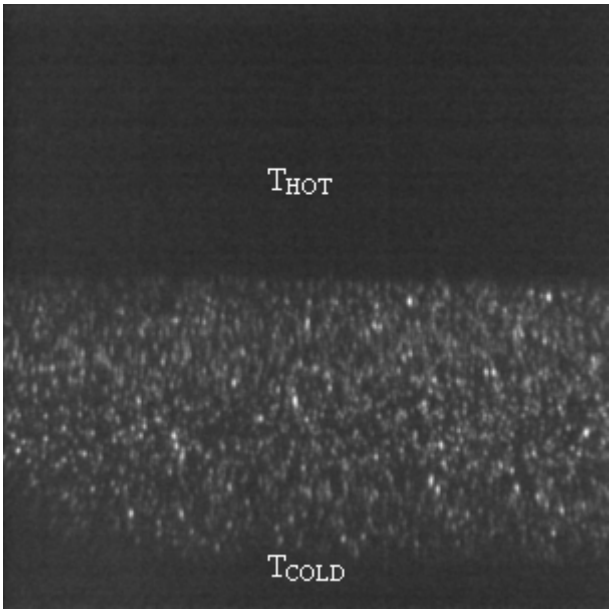

(c) $\Delta T/\Delta x$ = 300 K/cm

Figure 3-7. Continued

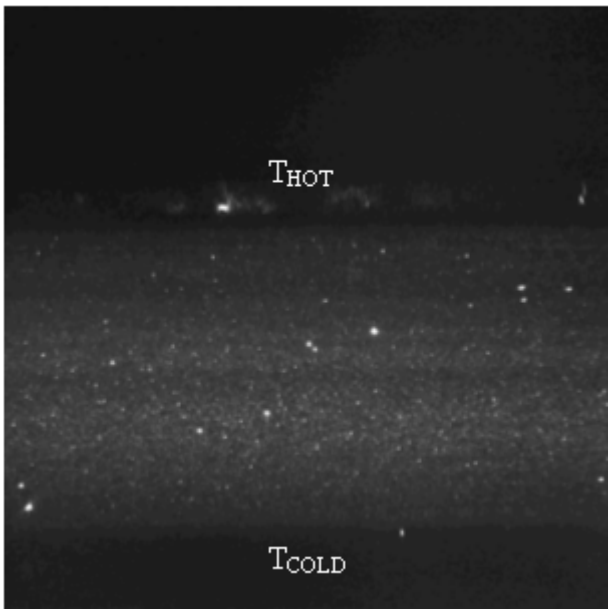

(a) $\Delta T/\Delta x$ = 100 K/cm

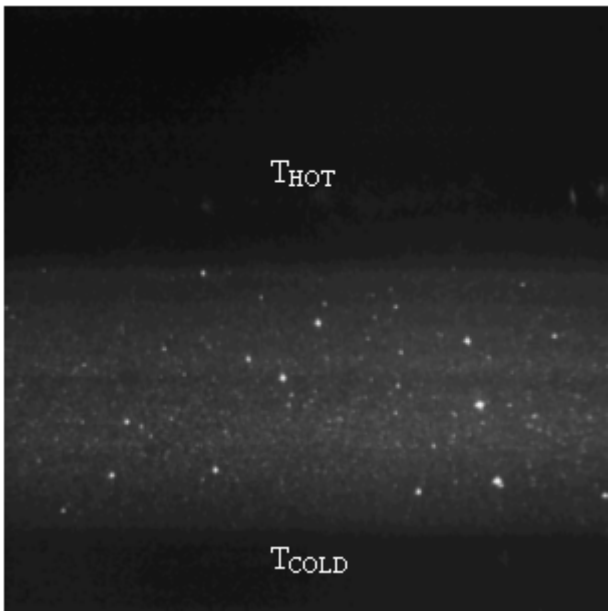

(b) $\Delta T/\Delta x$ = 300 K/cm

Figure 3-8. Photographic images of thermophoretically moving particles of 100-nm diameter at temperature gradients of (a) $\Delta T/\Delta x$ = 100 K/cm and (b) $\Delta T/\Delta x$ = 200 K/cm.

Figure 3-9 is the line average thermophoretic velocity at T = 303 K, in which the temperature position is decided based on a linearly stratified temperature field between the upper hotter temperature and lower colder temperature. Velocities in Figure 3-9 are compared with the the existing empirical theory of McNab and Meisen (1973). Line averaged thermophoretic velocities are close enough to the empirical theoretic prediction by McNab and Meisen. Only the 100-nm nanoparticle show a large deviation from prediction. This may be a result of the captured image quality. The smaller nanoparticle has higher Brownian motion and is thus more sensitive to flow instabilities, which generate side flow motions during imaging.

Based on the thermophoretic velocity equation, Eq (3-3) in liquid by McNab and Meison, an uncertainty analysis is conducted. Equation (3-3) can be divided into two terms, a temperature dependent term and a temperature gradient dependent term. If the temperature dependent term is set as ζ,

$$\varsigma = \frac{k_{BF}}{2k_{BF} + k_p} \frac{\mu}{\rho T} \tag{3-4}$$

then Equation (3-3) can be rewritten as

$$U_{th} = -\lambda \varsigma \frac{\Delta T}{\Delta x} \tag{3-5}$$

where Δx is the distance between two hot and cold plates. The measured temperature gradient has a range of 13 to 39 K and its uncertainty is dependent on the thermometer, which has a specification of 0.01 K system and 0.25 K reading errors. The gap distance is measured as 1.3 mm with 0.01 mm and 0.005 mm system and reading errors, respectively. To check the temperature uncertainty, Equation (3-4) is plotted along temperature

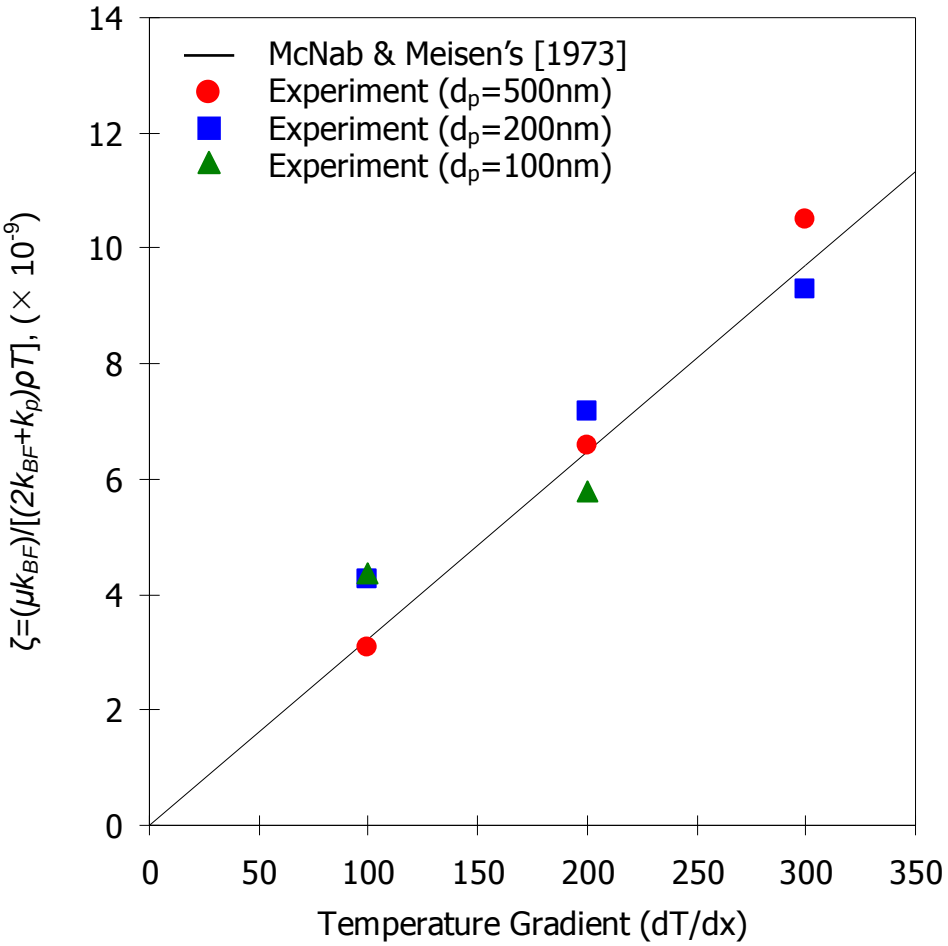

Figure 3-9. Line averaged thermophoretic velocities dependent on temperature gradient at the T = 303 K for three different size nanoparticles.

changes in Figure 3-10. While thermophoretice velocity is calculated at T = 303 K, possible temperature variation is ± 0.5 K, so that the temperature term uncertainty is calculated to be 2.42% within ± 0.5 K deviation from Figure 3-10. The resulting uncertainty from the thermophoretic velocity is 3.21 %.

From the imaging process, there is another uncertainty factor by Brownian motion. Because the thermophoretic velocity of nanometer size particles is of a similar scale as Brownian motion, the deviation by Brownian motion (Santiago et al., 1998) will be larger. However, this uncertainy can be dramatically reduced by tracking a higher number population in each image. The Brownian motion uncertainty can be expressed mathematically

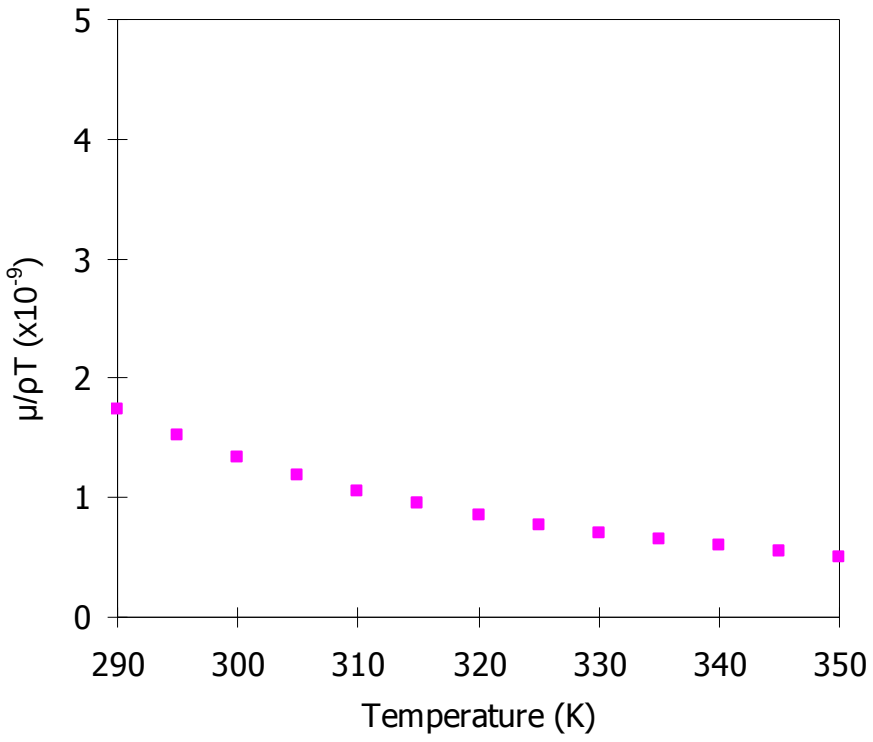

Figure 3-10 Temperature effect on only the temperature dependent term.

as (Kim et al., 2002)

$$\varepsilon_{U_{Br}} = \frac{U_{Br}}{U_{th}} \frac{1}{\sqrt{N}} = \frac{\sqrt{2D_{dif}/\Delta t}}{U_{th}\sqrt{N}} \tag{3-6}$$

where U_{th} and U_{Br} measure the thermohoretic velocity and Brownian velocity at the same temperature condition, respectively, N is the total number of particles (the combination of number of images and particle number in each image), and D_{dif} is the diffusion coefficient, $k_bT/3\pi\mu d_p$. If there are one thousand total particles, the uncertainty of Brownian motion will be less than 0.45 %. In reality, however, there are more than one hundred times more particles in total. Thus Brownian uncertainty will be negligible. For the case of one thousand particles, the maximum total uncertainty is 3.66 %.

3.5 Conclusion

Thermophoretic velocity for nanometer size particles has been measured under different temperature gradients and compared with an existing theoretical prediction, which was validated for only micro-meter size particles.

A well-defined temperature and temperature gradient field was controlled by a precision thermal bath, and nanometer size seeding particles were illuminated by a 488 nm wavelength Ar-ion laser. Re-emitted light from the fluorescent seeding particles along the laser sheet focused by a pair of optical lens was captured by a cooled CCD camera and analyzed using the PIV technique.

The experimental result shows the thermophoretic velocity of nanometer size particles is in good agreement with existing theory. Thus, the empirical theory for thermophoretic velocity can be extended to nanometer size particle motion.

The thermophoretic velocity in liquid is independent of floating particle size and different from that in gas. The thermophoretic velocity is a weak function of temperature inversely and a strong function of temperature gradient.

CHAPTER 4

NANOFLUID DROPLET EVAPORATION

When a particle-laden liquid droplet evaporates, such as in colloidal fluids and nanofluids, uneven progress of dryout tends to deposit the residual particles in a ring-shaped pattern along the original wet surface boundary (Deegan *et al.*, 1997). These ring-like dryout patterns can be seen in many practical examples ranging from soap water droplet stains to the recent DNA mapping techniques where particle (DNA)-laden microscale flows stretch and deposit the DNA molecules onto a substrate, also termed as "fluid fixation" (Dugas *et al.*, 2005; Wang *et al.*, 1998).

The history of published interest in the ring stain formation goes back to Denkov et al. (1992) who analytically described the mechanism of particle formation as the capillary effect existing between particles, and about a decade later they comprehensively studied these capillary forces and particle ring formation (Kralchevsky and Denkov, 2001). A series of publications by Deegan *et al.* (1997, 2000, 2000) presented physical explanations of colloidal fluid evaporation and ring formation and growth in such naturally occurring events as a coffee ring stain. Uno *et al.* (1998), and Tay and Edirisingre (2002) studied the particle deposition on both hydrophilic and hydrophobic surfaces, Conway *et al.* (1997) studied the size and concentration effects of polystyrene beads on the ring formation, and Maenosono *et al.* (1999) studied the ring growth of semiconductor nanoparticles in liquids. While these studies focused on how the ring stain is formed and which parameters can alter ring growth, a systematic heat transfer study to

quantitatively explain the unique evaporation/dryout has not been published to the author's knowledge.

In contrast, for the case of single phase liquid dryout/evaporation, an extensive publication list is available for both experimental and numerical investigations on the highly detailed heat and mass transfer phenomena. Birdi *et al.* (1989, 1993) examined the mass transfer rate for evaporating water droplets and presented observation of pinned contact lines on a glass surface. Shanahan and Bourges (1994, 1995, 1995) measured the time-varying heights, contact angles, and contact-line radii of evaporating water droplets and presented an explanation for "stick-slip" evaporation. Hisatake *et al.* (1993) experimentally studied the evaporation rate as a function of temperature, humidity, air velocity, and vessel dimensions. Anderson and Davis (1995) performed numerical predictions for the effects of capillarity, thermocapillarity, vapor recoil, viscous spreading, contact angle hysteresis, and mass loss during liquid droplet evaporation. Fisher (2002) and Hu and Larson (2002, 2005) studied the internal flow fields inside evaporating droplets using lubrication theory and computational methods, respectively.

With regard to heat transfer of liquid droplet evaporation, Michiyoshi and Makino (1978, 1984) examined the heater surface temperature profiles underneath an evaporating droplet contacting different heated surfaces. Klassen *et al.* (1990, 1993) presented measurements of the temperature distribution of an evaporating droplet with infrared thermography and Chandra *et al.* (1996) evaluated the effect of initial contact angle on evaporation and calculated surface temperature and heat flux during droplet evaporation. Xiong and Yuen (1991) experimentally studied the plate bulk temperature and overall heat flux during droplet evaporation. In 1999, Rule and Kim (1999) fabricated a complex

microheater array to achieve spatially resolved heat flux measurements for the case of pool boiling of FC-72. More recently, Paik *et al.* (2005, 2006) fabricated a 32-linear microheater array to study the microscale heat and mass transport for slowly evaporating sessile water droplets.

4.1 Objective

A nanofluid is a mixture of metallic nanoparticles (Au, CuO, Al_2O_3, etc.) with a base fluid (water, ethylene glycol, etc.), which is known to have substantially enhanced thermal conductivity with relatively small concentration of nanoparticles. (Lee *et al.*, 1999) Nanofluids have broad potential as a next-generation coolant in various energy saving applications where effective cooling, small scale heat dissipation, and high density power system management are required. In addition, recently emerging applications include nano-patterning and electrical circuitry fabrication by nanofluid evaporation. (Szczech *et al.*, 2002; Yarin *et al.*, 2006) These applications require commanding knowledge of the fluidic and heat transfer mechanisms peculiar to nanofluid droplet evaporation, dryout, and nanoparticle deposition.

In this chapter, in an effort to elucidate nanofluid droplet evaporation characteristics, experimental results are presented of dryout and heat transfer characteristics for evaporating nanofluid droplets using a microfabricated linear heater/detector array consisting of 32 gold heater lines, 100-μm wide and 0.5-μm thick.

4.2 Microheater Fabrication

A microheater array was designed and fabricated by Dr. Paik (2005) using standard MEMS lithography techniques within a class-1000 clean room facility. As shown in Figure 4-1, the microheater array consists of 32 gold line heaters that are 100-μm wide, 0.5-μm thick, and 1.5-cm long, individually, and are spaced 100-μm apart. More detailed heater design and fabrication processes are presented in the dissertation work of Dr. Paik (2005), and also in a previous publication (Paik *et al.*, 2006). The 32 linear heaters provide the total heated area of 0.946 cm^2 (0.63-cm wide x 1.5-cm long).

Over the tested temperature range from 40 to 80°C, the temperature-resistance relation of gold is approximated to be linear as (Young and Freedman, 1996)

$$R = R_o\left(1 + \alpha\left(T - T_o\right)\right) \tag{4-1}$$

where the resistance-temperature coefficient α = 0.003715 K^{-1} for gold and R_o is the resistance of gold at the reference temperature T_o = 25°C. Equation (1) implies that the same gold heater can serve as a temperature sensor via measurement of the resistance. The resistance value uncertainty occurring from the linearization approximation of Eq. (4-1) is estimated as 0.0062 Ω, and the resulting temperature uncertainty is estimated as 0.12 %. (Paik *et al.*, 2006)

The experimental setup consists of two sub-systems, (1) the heater power control and recording unit for constant voltage operation, and (2) the imaging unit with Canon Macrolens FD 50-mm CCD camera (640 × 480 pixels at 1-fps) to record the droplet evaporation and dryout progress. The constant voltage circuit consists of a parallel arrangement of the 32 heater lines, each line connected in series with a fixed 51 Ω resistor.

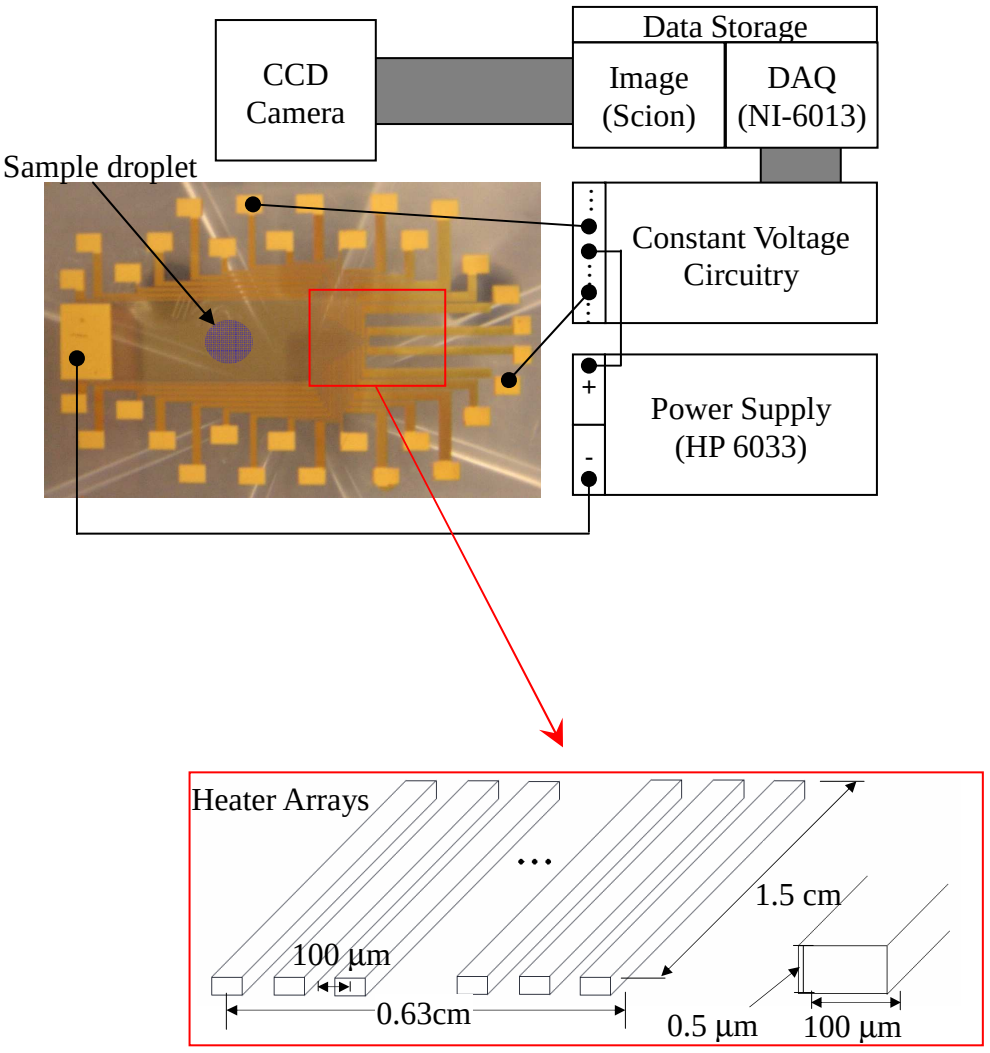

(a)

Figure 4-1. Schematic illustration of the constant-voltage experimental system for the droplet evaporation with (a) experimental setup and a detailed microheater array with 32-gold line heaters, which are 100-µm wide, 0.5 µm thick, and 1.5 cm long, individually, and are spaced 100 µm apart, and (b) a voltage divider circuit diagram.

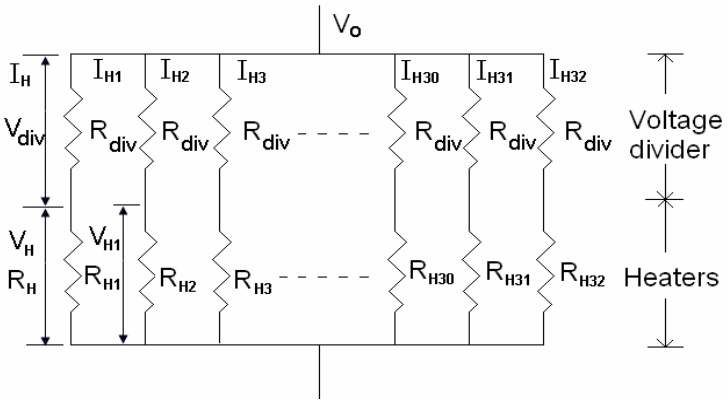

(b)

Figure 4-1. Continued

Since each fixed resistor R_{div} acts as a voltage divider, the current may be calculated as $i_H = V_{div}/R_{div}$ with knowledge of the supply voltage and the voltage drop V_{div} across the fixed resistor. When a droplet contacts the heater array, the resistance of each line heater R_H varies accordingly and can be calculated as $R_H = V_H/i_H$ by measurement of the voltage across each heater line V_H. Subsequently, the line heater temperature is calculated using Eq. (4-1), and the heat flux from each heater element is calculated as:

$$P_H = i_H^2 R_H = \frac{V_{div}^2}{R_{div}^2} R_H(T) \tag{4-2}$$

Before each evaporation test, the microheater array surface was thoroughly cleaned with 99.9 % isopropyl alcohol and a specified supply voltage was provided to ensure a steady heater surface temperature condition. Once a micro pipette was used to gently place a 5-μl water or nanofluid droplet onto the heater surface, the history of the heater voltage drop was recorded during the entire evaporation/dryout progress, and the development of the evaporating droplet shape was simultaneously recorded.

4.3 Tomographic Deconvolution

Strictly speaking, a single measurement of the line heater temperature (Eq. (4-1)) and the heat flux (Eq. (4-2)) as determined from the heater voltage drop measurements described above is valid only if the heater is imposed to have a uniform temperature at any given instant of time. In reality, however, substantial temperature gradients exist since the different heat transfer characteristics between the dry and wet sections prevail

on a single heater surface and the temperature gradient distribution varies in time as the droplet evaporation progresses. In order to determine the distributed temperature profiles of the droplet considering the temperature gradients, tomographic conversion (Kak and Slaney, 1987) was conducted to deconvolute the line-averaged temperature into radially distributed temperature profiles assuming axi-symmetric evaporation and heat transfer.

The axi-symmetric tomographic conversion considers 16 concentric deconvolution zones corresponding to the 16 heater lines beneath and surrounding one half of the droplet. To present this process with clarity and simplicity, Figure 4-2 only gives 8 concentric tomographic deconvolution zones. Zone I covers only the central region of heater line A, and Zone II extends to cover the central regions of lines B (to the left) and C (to the right) as well as the two sub regions of line A. In a similar manner, zone VIII then includes partial regions of all lines, from A to O. The entire tomographic conversion domain covers a circular region 6.3 mm diameter, corresponding to the width of the 32-element heater array.

The sixteen unknown concentric zonal temperatures must be calculated from the sixteen known line-average measured resistances. Thus, sixteen linear algebraic equations are established to correlate the line-average measured resistances with unknown concentric temperatures. The k-th line heater, as represented by the heater line C in Figure 4-2 (b), consists of concentric zones i = k, k+1, … , N (N = 16). Beginning with the linear temperature-resistance relation of Eq. (4-1), it then follows that

$$\begin{aligned} R_k &= \sum_{i=k}^{N} R_{k,i} = \sum_{i=k}^{N} \left\{ R_o \left[1 + \alpha \left(T - T_o \right) \right] \right\}_{k,i} \\ &= \sum_{i=k}^{N} \rho_o \left[1 + \alpha \left(T_{k,i} - T_o \right) \right] \frac{L_{k,i}}{w d_r} = \frac{\rho_{r,o} L}{w d_r} - \frac{\rho_{r,o} \alpha L T_o}{w d_r} + \frac{\rho_{r,o} \alpha}{w d_r} \sum_{i=k}^{N} T_{k,i} L_{k,i} \end{aligned} \tag{4-3}$$

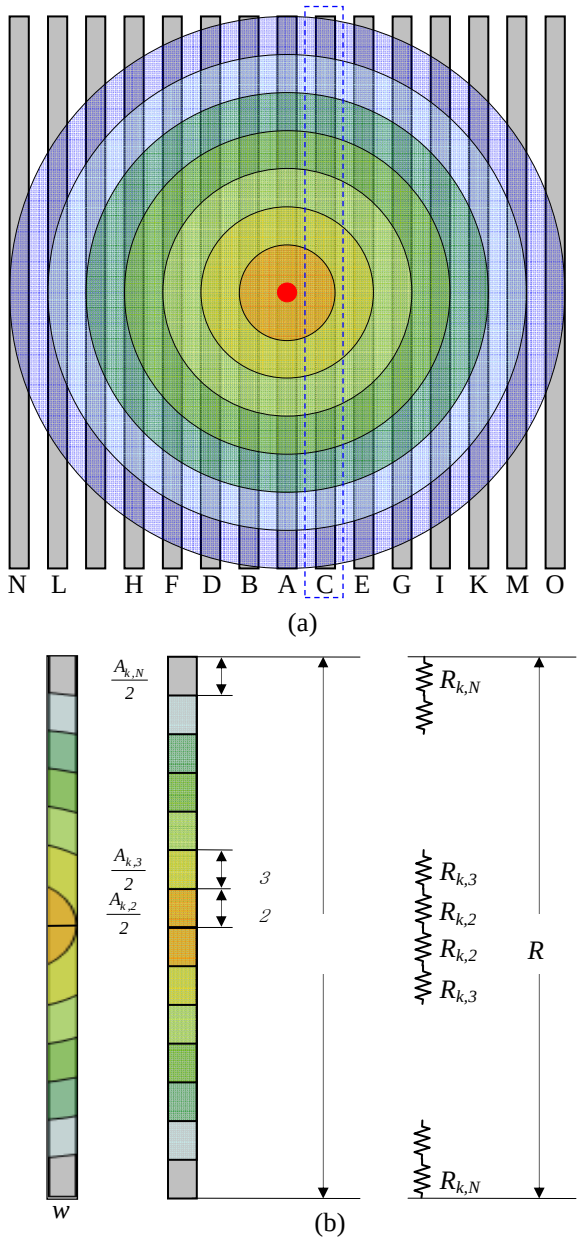

Figure 4-2. Schematic of the deconvoluted tomographic temperature zones illustrated with (a) the eight-zone tomographic deconvoluted heater area and (b) reconstructed zones for temperature calculation with electric resistance.

with the resistivity ρ_r defined by $\rho_r = R\, w_{HT}\, d_{HT} / L$ where w_{HT} and d_{HT} are the line heater width and thickness, respectively, and $L = \sum_{i=k}^{N} L_{k,i}$. The equivalent heater length of each sub-zone may be represented as $L_{k,i} = A_{k,i} / w_{HT}$ with the assumption of a rectangular area. Equation (4-3) then becomes

$$R_k = \frac{\rho_{r,o} L}{w_{HT} d_{HT}} - \frac{\rho_{r,o} \alpha L T_o}{w_{HT} d_{HT}} + \frac{\rho_{r,o} \alpha}{w_{HT}^2 d_{HT}} \sum_{i=k}^{N} T_{k,i}\, A_{k,i} \tag{4-4}$$

Using the resistivity definition, the measured line-average resistance is expressed as

$$R_k = \rho_{r,o} \left[1 + \alpha (T_k - T_o)\right] \frac{L}{w_{HT} \cdot d_{HT}} \tag{4-5}$$

Combining Eqs. (4-4) and (4-5), the measured line-average temperature can be re-expressed as a deconvoluted temperature for each concentric zone Tk,i,

$$T_k = \frac{1}{L \cdot w_{HT}} \sum_{i=k}^{N} T_{k,i}\, A_{k,i} \tag{4-6}$$

Each of the 16 zonal deconvoluted temperatures can then be calculated using Eq. (4-6). This is accomplished in a sequential fashion beginning with the outmost heater where the temperature of heater zone 16 is simply equal to the line-averaged temperature of heater line 16. Heat flux to the droplet is readily calculated from the measured circuit voltages with Eq. (4-2) and deconvoluted with Eqs. (4-3) and (4-6).

4.4 Nanofluid Droplet Evaporation Test

Four different nanofluid samples containing 0.5 vol. % nanoparticles were tested: (1) 2-nm Au nanoparticles (nanoComposix Inc.), (2) 11-nm Al_2O_3 nanoparticles

(Nanostructured & Amorphous Materials Inc.), (3) 30-nm CuO nanoparticles (Nanophase Inc.), and (4) 47-nm Al2O3 nanoparticles (Nanophase Inc.).

4.4.1 Evolution and Dryout of Evaporating Nanofluid Droplets.

Figure 4-3 details the evolution of 11-nm Al_2O_3 nanofluid droplet evaporation as one representative example. Immediately after placement on the microheater substrate, the droplet is pinned along the wet perimeter due to the capillary forces between nanoparticles that are close to the surface and the irregularity of the surface including its roughness and contact potential (Deegan *et al.*, 2000; Deegan, 2000) (Figure 4-3 (a)). During the liquid dominant evaporation (Figure 4-3 (b)), the strong pinning of nanoparticles acts to congregate them to the rim and the droplet thickness and contact angle decrease while the wet diameter remains constant. With further evaporation of liquid, the contact angle exceeds the critical angle (Shanahan and Bourges, 1994, Bourges and Shanahan, 1995, Hu and Larson, 2002) and the thin core liquid region begins to break away from the rim (Figure 4-3 (c)). Note that the rim region, where most nanoparticles are distilled with little water, dries out first because of the expedited evaporation by the higher thermal conductivity of nanoparticles than that of water. The de-pinned core liquid then shrinks toward the center as the evaporation further progresses (Figure 4-3 (d)). The resulting ring-shaped nanoparticle stain is formed along the rim and the evaporation is completed (Figure 4-3 (e)).

Figure 4-4 shows evolvement of droplet wet diameters (D/Do) as functions of evaporation time for water and four tested nanofluids heated by the microheater array at

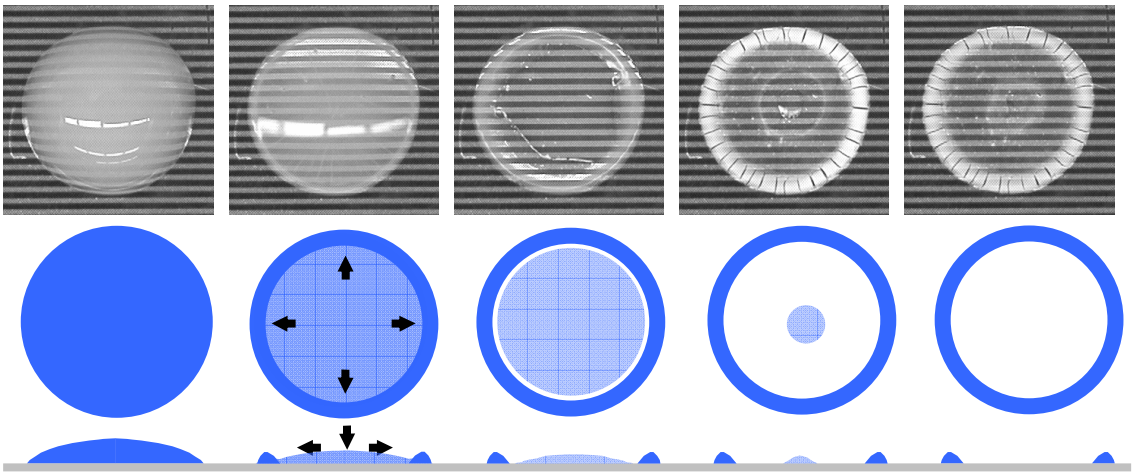

(a)	(b)	(c)	(d)	(e)
Pinning	Liquid Dominant Evaporation	Depinning	Dryout Progress	Formation of Nanoparticle Stain

Figure 4-3. Evolution of 11-nm Al_2O_3 nanofluid droplet evaporation/dryout with sequential photographs and schematic sketches. Just after placement on the microheater substrate, the droplet is pinned at the edge (Pinning, a). During the liquid dominant evaporation, the strong pinning of nanoparticles acts to congregate them to the rim and the droplet thickness and contact angle decrease while its wet diameter remains constant (Liquid Dominant Evaporation, b). With further evaporation of liquid, the contact angle exceeds the critical angle and the thin core liquid region begins to break away from the rim (Depinning, c). The de-pinned core liquid then shrinks toward the center as the evaporation further progresses (Dryout Progress, d). Finally the resulting ring-shaped nanoparticle stain is formed along the rim and the evaporation is completed (Formation of Nanoparticle Stain, e).

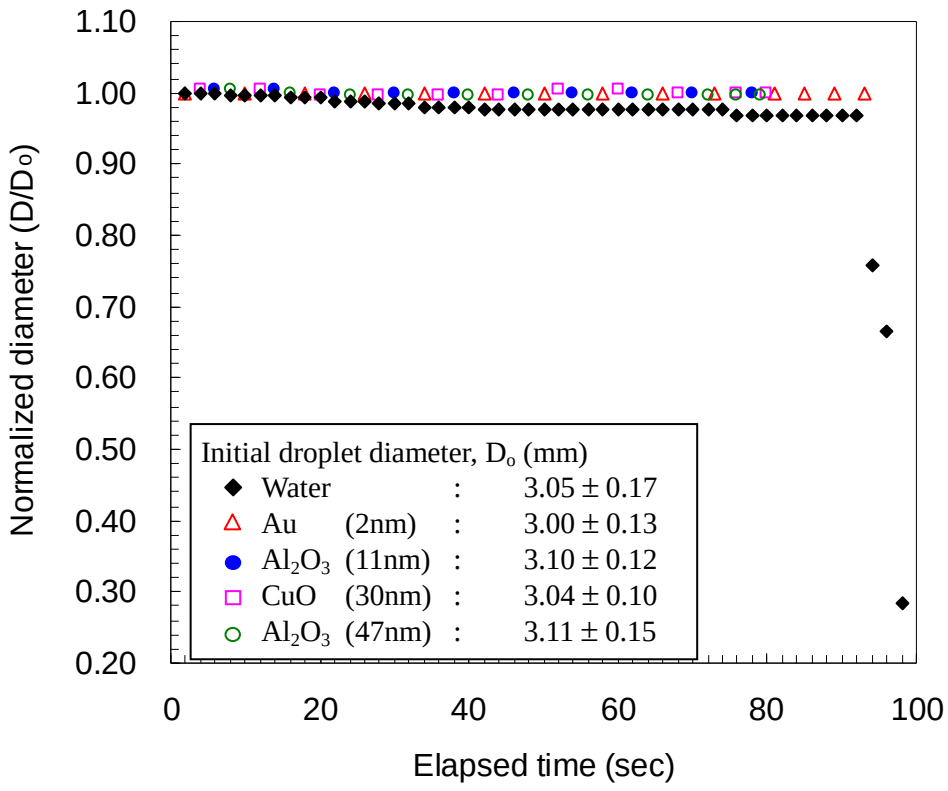

Figure 4-4. Evolvement of droplet wet diameters (D/D_o) as functions of evaporation time for water and four different nanofluids placed on the hydrophilic microheater surface at 80°C initial temperature. The strong pinning of nanofluid droplets sustains their wet diameters to remain the same as the initial wet diameter (D_o) until their completion of dryout. The water droplet diameter remains unchanged during the pool evaporation of water, which occupies more than 90% of the total evaporation time, and drastically shrinks during the dryout as the peripheral thin film rapidly recedes toward the center.

80°C initial temperature. Note that the heater array is coated with SU-8 for electrical insulation and protection and the SU-8 surface is plasma treated to convert its original hydrophobic surface into hydrophilic surface (Vijayendran *et al.*, 2003). The strong pinning of all nanofluid droplets sustains their wet diameters to remain the same as the initial wet diameter (D_o) until their complete dryout (Tay and Edirisinghe, 2002). The water droplet diameter remains unchanged during the pool evaporation of water, which occupies more than 90% of the total evaporation time, and drastically shrinks during the dryout as the peripheral thin film rapidly recedes toward the center.

Figure 4-5 shows different dryout patterns for the case of an 80°C initial heater temperature primarily depending on the nanoparticle sizes at the same volume concentration of 0.5 vol. %: (a) 2-nm Au particles, (b) 11-nm Al_2O_3 particles, (c) 30-nm CuO particles, and (d) 47-nm Al_2O_3 particles. The greatly increased number density of the finer gold particles enhances the resulting viscosity (Pak and Cho, 1998) and inter-particular capillary actions (Son and Kihm, 1998), which in turn make the nanoparticle distillation less pronounced and tend to spread the nanoparticles out as the evaporation progresses to dryout (Figure 4-5 (a)). The relatively higher specific gravity of gold (SG = 19.3) additionally contributes to hinder the distillation of nanoparticles to the rim. A thicker and more uniform dryout pattern results in the core with a loosely defined, wider ring in the rim as schematically illustrated in Figure 4-6 (a). At the other extreme among the tested, the dryout pattern of the largest Al_2O_3 nanoparticles (Figure 4-5 (d) and Figure 4-6 (b) for schematic illustration), which are about 12,000 times less populated than the gold particles, shows a highly distinctive ring-shaped stain because of the lower viscosity and less capillary actions between nanoparticles. The low SG of 3.6 also makes the Al_2O_3

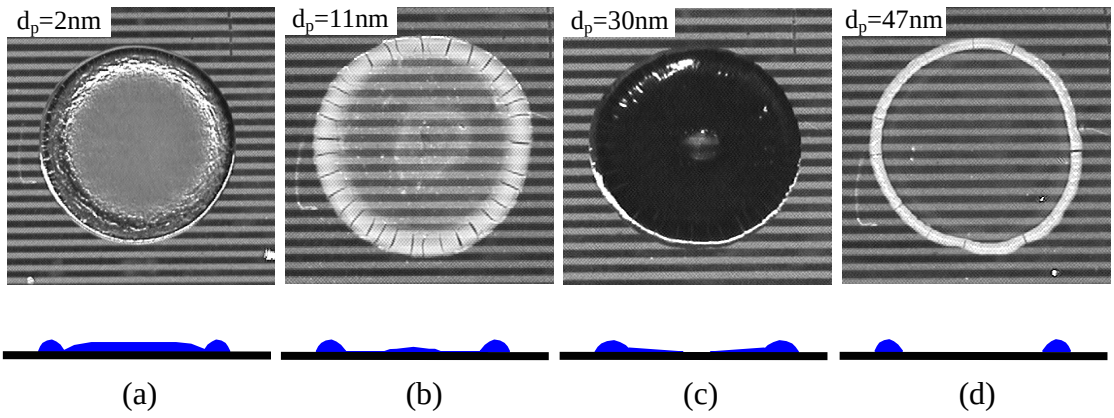

Figure 4-5. Nanofluid dryout patterns for the case of 80°C initial heater temperature, primarily depending on the nanoparticle sizes at the same volume concentration of 0.5 vol. %: (a) 2-nm Au particles, (b) 11-nm Al_2O_3 particles, (c) 30-nm CuO particles, and (d) 47-nm Al_2O_3 particles. Smaller nanoparticles are deposited thicker and more globally and uniformly in the droplet inner region. Larger nanoparticles show more distinctive ring-shaped nanoparticle stain at the droplet edge.

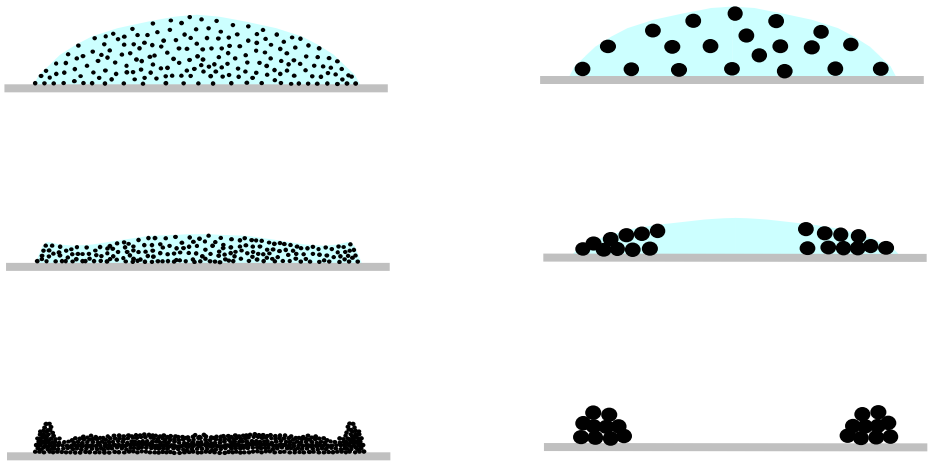

Figure 4-6. Conjectured nanofluid droplet evaporation and dryout processes depending on particle sizes: (a) smaller nanoparticles (2-nm Au), and (b) larger nanoparticles (47-nm Al_2O_3). Higher populated smaller nanoparticles have slower outward capillary flow by higher viscosity, and a thicker and more uniform dryout pattern results in the core with a loosely defined wider ring in the rim. Larger nanoparticles, with lower viscosity and less capillary actions, readily move to the rim during the distillation and show a highly distinctive ring-shaped stain.

nanoparticles readily move to the rim during the distillation. The in-between cases of 11-nm Al_2O_3 and 30-nm CuO nanofluids (Figures. 4-5 (b) and (c)) display thin dryout layers in the core and loosely defined wide ring stains in the rim which reflect a cross between the two extreme cases.

4.4.2 Temperature and Heat Flux Characteristics of Evaporating Nanofluid Droplets

Figure 4-7 plots the average temperature and average heat flux of different nanofluids and water droplets for initial microheater surface temperatures of (a) 80 and (b) 60°C. Tomographically deconvoluted thermal properties, either temperature or heat flux, are multiplied by the ratio of each concentric ring area to the initial droplet wet area, and the summation of all these weighted properties provides the average properties.

The last stage of water droplet evaporation shows more gradual recovery in temperature as well as heat flux than those of nanofluids. The last stage of nanofluids reveals substantially more rapid temperature and heat flux recovery. It is believed that this is attributed to the strongly pinned nanoparticles which keep the droplet diameter constant during evaporation and hold water molecules between nanoparticles until sudden release after the depinning process upon liquid depletion.

The temporally developed average temperature and heat flux data of nanofluids can be conceptually divided into three periods: (I) Liquid Dominant Evaporation showing the constant temperature from the initial sharp drop of the data to the point of discontinuity (Figures 4-3 (a) and (b)), (II) Dryout Progress from the discontinuity to the recovery of initial temperature and heat flux (Figures. 4-3 (c) and (d)), and (III) Formation

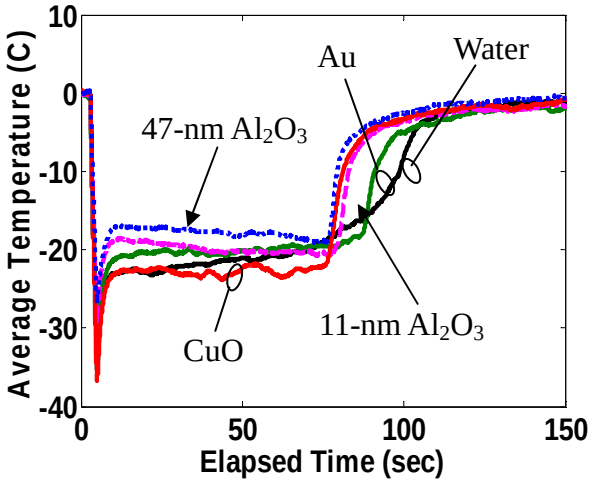

(a)

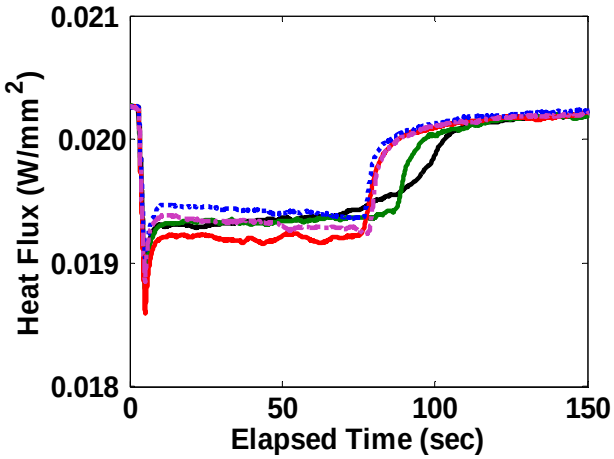

(b)

Figure 4-7. Average temperature (a and b) and average heat flux (c and d) of different nanofluids and water droplets for initial microheater surface temperatures of 80 °C (a and c) and (b) 60°C (b and d).

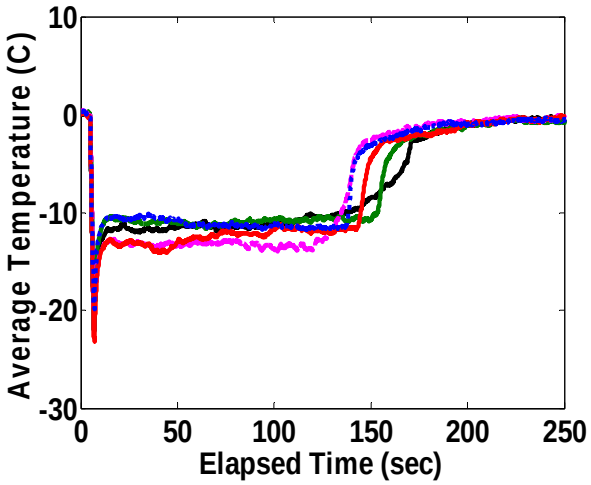

(c)

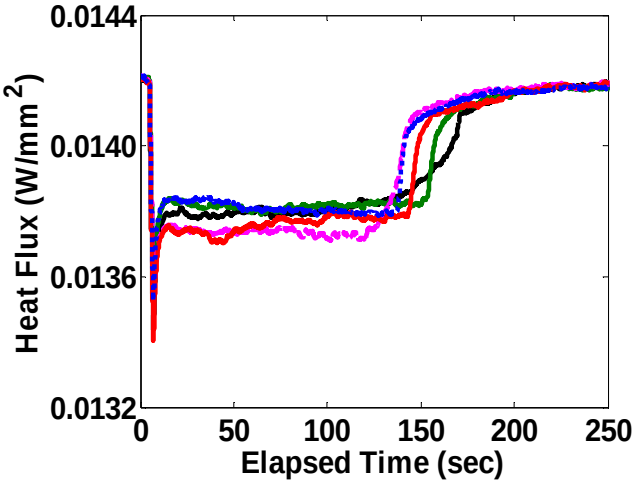

(d)

Figure 4-7. Continued

of Nanoparticle Stain after completion of dryout (Figure 4-3 (e)). The data discontinuity occurs due to the competing evaporation/dryout process in that the high thermal conductivity of nanoparticles dramatically expedites the evaporation of the surrounding liquid. The water droplet, on the other hand, does not show any discontinuity in the data and displays a smooth transition from the constant temperature pool evaporation to the gradually increasing dryout evaporation because of the phase change nature of a pure liquid.

For the case of the smallest Au nanoparticles (2-nm average diameter), the delayed transition from period (I) to period (II) is persistently observed while virtually no distinction is seen for the rest of the nanofluids containing nanoparticles ranging from 11 to 47-nm in diameter. It is conjectured that the high population of Au nanoparticles and the increased nanofluid viscosity are expected to slow down the convective heat/mass transport inside the droplet resulting in a slower evaporation of the surrounding liquid.

Figure 4-8 shows deconvoluted temperature profiles for (a) and (d) 2-nm Au, (b) and (e) 30-nm CuO, and (c) and (f) 47-nm Al_2O_3 nanofluids for the case of an initial microheater surface temperature of T_o = 80°C. The first three Figures (a) to (c) present developing temperature profiles with time at different radial locations from the center (r/r_o = 0), through the edge of wetted droplet (r/r_o = 1, in bold), to the outside of the droplet (r/r_o = 2), progressively from the bottom to the top profiles. Figures (d) to (f) present the same data as temporal evolvement of radial profiles for the time span from t/τ_o = 0.01, with τ_o being the dryout time, to after completion of evaporation (t/τ_o = 2.0).

As shown in the left column, the span of the lower three temperature profiles, corresponding to the inside of the nanofluid droplet wet area, increases with increasing

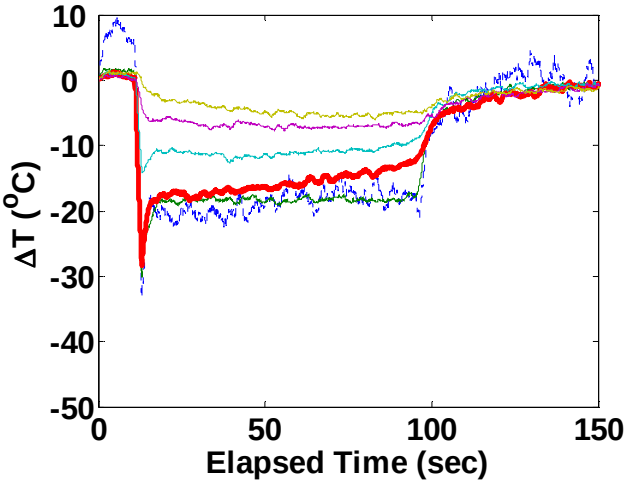

(a)

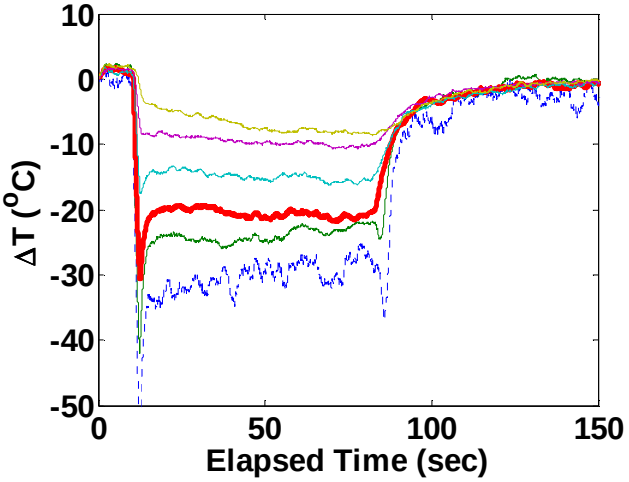

(b)

Figure 4-8. Deconvoluted temperature profiles for (a) and (d) 2-nm Au, (b) and (e) 30-nm CuO, and (c) and (f) 47-nm Al_2O_3 nanofluids for the case of initial microheater surface temperature of T_o = 80°C. (a) ~ (c) present temporal temperatures at the nondimensional positions r/r_o = 0, 0.5, 1.0 (the wetted droplet edge), 1.2, 1.5, 2 (from bottom to top) and (d) ~ (f) present spatial temperatures at nondimensional time t/τ_o = 0.01 (+), 0.1 (○), 0.5 (□), 0.9 (◇), 0.95 (△), 0.99 (▽), 1.1 (✳), 2 (x).

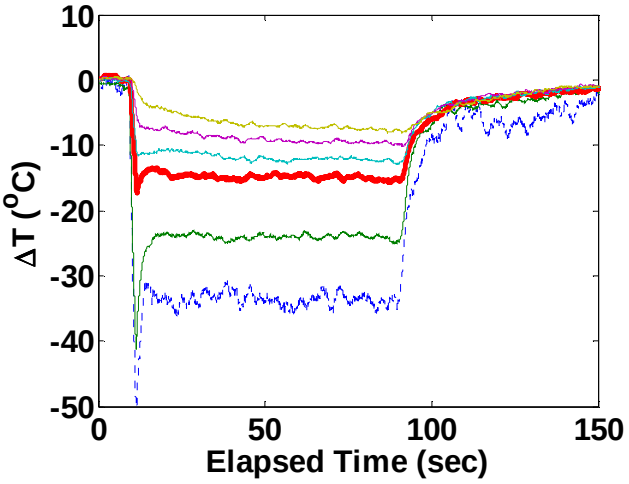

(c)

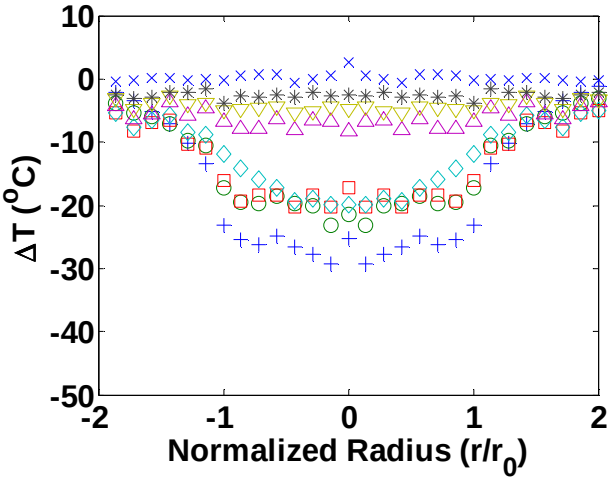

(d)

Figure 4-8. Continued

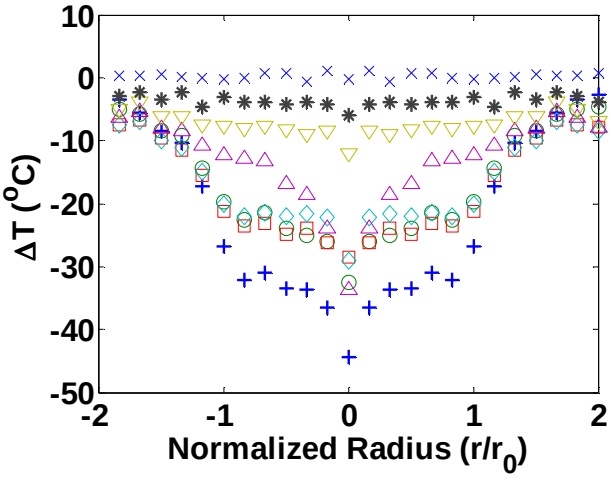

(e)

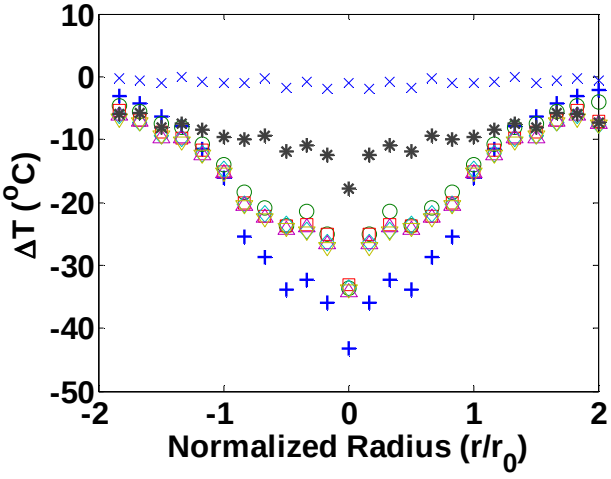

(f)

Figure 4-8. Continued

nanoparticles size. The larger population and increased nanofluid viscosity of the smaller Au nanoparticles distributes nanoparticles more evenly during the evaporation and makes the evaporation slower with the relatively small temperature span between the center and the edge. With increasing nanoparticle size, the more aggressive convective motion of the surrounding liquid with lower viscosity tends to separate the nanoparticles to the rim area, which results in a more distinctively increased temperature at the edge where the high thermal conductivity of nanoparticles prevails. These findings are supplemented by the right column results showing the temperature spans increasing with increasing nanoparticle sizes.

Figure 4-9 shows the temperature spans between the droplet center and edge, averaged over the period from 10 to 90 % of the evaporation time. The largest 47-nm Al2O3 nanofluid shows the largest temperature difference reflecting more distinct separation of deposited particles in the edge area. During evaporation, the high thermal conductivity of pinned nanoparticles enhances the edge temperature over the center water region temperature. The temperature spans for both the 11-nm Al_2O_3 nanofluid and the 30-nm CuO nanofluid are approximately the same as also shown (Figures 4-5 (b) and (c)) for their similar deposition patterns: loosely defined wider rim areas and thin coated nanoparticle stains in the center region. The slight coating of nanoparticles in the central area, which slightly narrows the thermal conductivity difference between the center region and the edge region, is consistent with the temperature difference being less than the case of the 47-nm Al_2O_3 nanofluid. For the case of the 2-nm Au nanofluid, due to the high population of nanoparticles and the nanofluid viscosity, both nanoparticle concentrations and temperature distributions deviate less between the center and edge

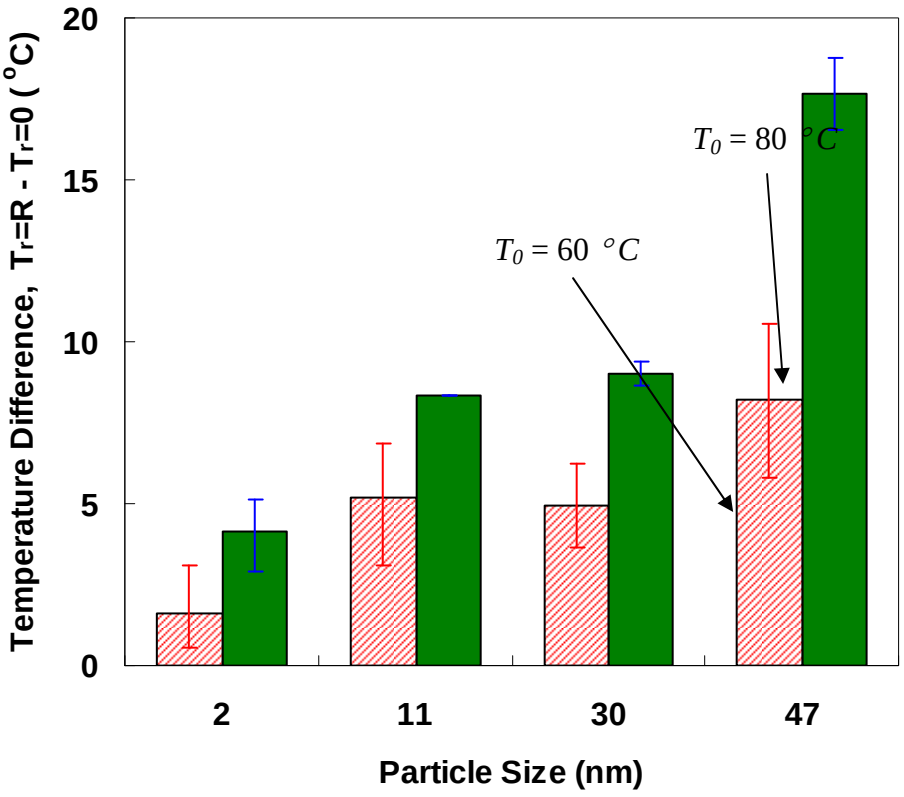

Figure 4-9. Temperature spans between the droplet center and edge, averaged over the period from 10 to 90 % of the evaporation time. The largest 47-nm Al_2O_3 nanofluid shows the largest temperature difference reflecting more distinct separation of deposited particles in the edge area. For the case of the 2-nm Au nanofluid both nanoparticle concentration and temperature distribution deviate less between the center and edge regions. The corresponding dryout pattern shows a loosely defined rim with relatively thick coated nanoparticle stain in the center. Both the 11-nm Al_2O_3 nanofluid and the 30-nm CuO nanofluid are approximately the same as also shown for their similar deposition patterns.

regions. The corresponding dryout pattern (Figure 4-5 (d)) shows a loosely defined rim with relatively thick coated nanoparticle stain in the center.

4.5 Conclusion

Thermal characteristics of evaporating nanofluid droplets are experimentally studied using a microheater array of 32-line elements that are 100-μm wide, 0.5-μm thick and 1.5-cm long under a constant-voltage mode. Strongly pinned nanofluid droplets are considered for a sequential evaporation process of (1) Pinning, (2) Liquid Dominant Evaporation, (3) Depinning, (4) Dryout Progress, and (5) Formation of Nanoparticle Stain (Figure 3). Upon completion of the evaporation process, ring-shaped nanoparticle stains are left and the pattern of the stain strongly depends upon the nanoparticle sizes (Figure 4-4). In general smaller nanoparticles result in wider edge accumulation and more uniform central deposition whereas larger nanoparticles make more distinctive and narrower nanoparticle stains at the edge with less central deposition (Figure 4-6).

Tomographic deconvolution of measured data obtained from the linear heater elements reveals spatially and temporally resolved temperature/heat flux profiles on the wet droplet surface (Figures 4-7 and 4-8). Nanofluid evaporation consists of three periods. First, Liquid Dominant Evaporation (I) occurs with steady thermal properties that are nearly identical to those of pure water with little effect of suspended nanoparticles on the overall heat and mass transfer. Next, the Dryout Progress (II) characterizes the later part of evaporation when the nanoparticle effect dominates with water level being receded. This period shows discontinuous surge of temperature and heat flux, due to the high

thermal conductivity of nanoparticles, which rapidly recovers to the dry heater condition while the recovery process for pure water droplet is gradual and continual. Finally, Formation of Nanoparticle Stain (III) period occurs which strongly depends on nanoparticle size.

The temperature span between the droplet center and the edge (Figure 4-8) increases with increasing particle sizes, and this is consistent with the different stain patterns for different nanoparticle sizes. The more distinct ring-shaped edge accumulation of larger nanoparticles results in larger temperature span because of the large difference of thermal conductivity between nanoparticles and water. Accordingly, the less distinction between the edge ring and the central deposits for the case of smaller nanoparticles can result in a relatively small temperature span.

CHAPTER 5

CONCLUSIONS AND FUTURE RESEARCHES

5.1 Conclusions

Nanofludic heat and mass transport has been studied experimentally and the mechanism of thermal conductivity enhancement has been demonstrated by systematcally designed measurements of the roll of thermally driven nanoparticles and evaporative characteristics of nanoparticles in a droplet. Focus on these studies was to delineate the basic energy transport mechanism of highly thermal conducting nanofluid and the thermophysical roll of nanoparticles on it by experimentation. To achieve this goal, three different experiments have been conducted: (1) thermal conductivity measurement for nanofluids, (2) thermophoretic velocity measurement of nanoparticles, and (3) thermal and fluidic evaporation characteristics measurement for droplets embedding nanoparticles.

The following conclusions were drawn from the conducted experimental studies:

1. Temperature, particle size, volume concentration of particles, and particle types have been evaluated and validated as major factors for nanofluid thermal conductivity enhancement.
2. Particle mobility, called Brownian velocity, is validated as a most dominant factor in nanofluid thermal conductivity enhancement.
3. Temperature induces particle mobility and conclusively causes the thermal conductivity enhancement.

4. An empirical correlation has been derived for predicting nanofluid thermal conductivity.
5. Thermophoretic velocity theory in liquid is validated and extended to nanometer scale.
6. Both Brownian motion and thermophoretic motion are important to thermally driven particle motion and may induce micro-convection to enhance thermal conductivity.
7. Temperature gradient in thermophoresis plays a more important role than temperature in Brownian motion.
8. Thermophoresis is not dependent on particle size.
9. Nanofluid droplets shows unique evaporation characteristics called ring stain by nanoparticle's strong pinning.
10. Ring stain and particle deposition depend upon nanoparticle size.
11. Nanofluid temperature recovery is more distinctive than that of a water droplet.
12. The temperature difference between the edge and center depends on particle size. The most distinct ring stain is from the larger nanoparticle with larger temperature span because of large difference of thermal conductivity between nanoparticles and water.

Conclusively, the nanofluid thermal conductivity can be systematically controlled based on conducted experimental findings and the roll of nanoparticles in thermal conductivity enhancement and evaporation has been revealed. These findings will lead to

a complete understanding the energy and fluidic characteristics of nanofluids and the abnormally enhancing mechanism of nanofluid thermal conductivity and finally will help make nanofluids applicable in real world applications.

5.2 Recommendations for Future Study

The nanofluid thermal conductivity enhancing mechanism and other energy transport studies are not completed and need further exploration. For future and more extensive researches, there are several suggestions:

1. A study to link nanoparticle motion and micro-convection is required. There are several conjectures, however, direct evidence is still not shown. Therefore, the important question remains of how nanoparticle motion generates micro-convection and how fast micro-convection transfers heat.
2. As some researchers (Keblinski et al, 2002; Vadasz, 2005) suggested, the other possibility of inducing nanofluid thermal conducitivity enhancement such as heat transfer by phonon wave or thermal wave has to be searched and checked.
3. A continued study of nanofluid evaporation and ring stain control is desireable to allow for cheap and precise nanopatterning with evaporation.
4. The study of thermal characteristics in nanofluid thin film region generated during evaporation near the pinning position may prove to be a useful tool to understand thin film heat transfer.

REFERENCES

Adrian, R.J. (1988). Statistical Properties of Particle Image Velocimetry Measurements in Turbulent Flow. *Laser Anemometry Fluid Mechanics, III. Lisbon, Portugal, LADOAN Institute Superior Technico.*, 112-129

Adrian, R.J. (1991). Particle Imaging Techniques for Experimental Fluid Mechanics. *Annual Rev. Fluid Mech.*, 23, 261-304.

Anderson, D.M. and Davis, S.H. (1995). The Spreading of Volatile Liquid Droplets on Heated Surfaces. *Phys. Fluids*, *7*, 248-265.

Annual Book of ASTM Standards, 2005 Edition, ASTM International.

Bakanov, S.P. and Derjaguin, B.V. (1959). *Koll. Zh.*, *21*,365.

Balandin, A.A. (2002). Nanoscale Thermal Management. *IEEE Potentials*. Feb/Mar., 11-15.

Bird, R.B., Stewart, W.E., and Lightfoot, E.N. (2002). *Transport Phenomena*. 2nd ed., John Wiley & Sons Inc., New York.

Birdi, K.S., Vu, D.T., and Winter, A. (1989). A Study of the Evaporation Rates of Small Water Drops Placed on a Solid Surface. *J. Phys. Chem.*, *93*, 3702-3703.

Birdi, K.S. and Vu, D.T. (1993). Wettability and the Evaporation Rates of Fluids from Solid-Surfaces. *J. Adhes. Sci. Technol.*, *7*, 485-493.

Bourges, C. and Shanahan, M.E.R. (1995). Influence of Evaporation on Contact Angle. *Langmuir*, *11*, 2820-2829.

Brock, J.R., 1962, "On the Theory of Thermal Forces Acting on Aerosol Particles," *J. Colloid Interface Sci.*, *17*, 768-780.

Brown, R. (1966). *in The World of the Atom*. edited by Boorse, H. and Motz, L., Basic Books, New York.

Buongiorno, J., 2006, “Convective Transport in Nanofluids,” *J. Heat Transfer*, *128*, 240-250.

Carey, V.P. (1999). *Statistical Thermodynamics and Microscale Thermophysics*. Cambridge, New York.

Cawood, W. (1936). *Dispersed system in gases: Dust, Smoke and Fog*. Faraday Society General Discussion, Gurney and Jackson, London, 1068.

Chandra, S., di Marzo, M., Qiao, Y.M., and Tartarini, P. (1996). Effect of Liquid-Solid Contact Angle on Droplet Evaporation. *Fire Safety J.*, *27*, 141-158.

Choi, U.S. (1995). Enhancing Thermal Conductivity of Fluids with Nanoparticles. *Developments and Applicatioins of Non-Newtonian Flows*, D.A. Siginer and H.P. Wang, eds. FED-Vol. 231/MD-Vol. 66, ASME, New York, 99-105.

Choi, S.U.S., Zhang, Z.G., Yu, W., Lockwood, F.E., and Grulke, E.A. (2001). Anomalously Conductivity Enhancement in Nano-tube Suspensions. *Appl. Phys. Lett., 79(14)*, 2252-2254.

Choi, S.U.S., Zhang, Z.G., and Keliniski, P. (2004). Nanofluids in *Encyclopedia of Nanosicence and nanotechnology*, ed. H.S. Nalwa, Vol. 6, 757-773, American Scientific Publishers, Los Angeles, Calif.

Chon, C.H., Kihm, K.D., Lee, S.P., and Choi, S.U.S. (2005). Empirical Correlation Finding the Role of Temperature and Particle Size for Nanofluid (Al_2O_3) Thermal Conductivity Enhancement. *Appl. Phys. Lett. 87*, 153107.

Christensen, K.T., Soloff, S.M. and Adrian, R.J. (2000). PIV Sleuth: Integrated Particle Image Velocimetry (PIV) Interrogation/Validation Software. Tech. Report 943, Dept. Theoretical and Applied Mechanics, UIUC.

Conway, J; Korns, H.; Fisch, M.R. (1997). Evaporation Kinematics of Polystyrene Bead Suspensions. *Langmuir*, *13*, 426-431.

Das, S.K., Putra, N., Thiesen, P., and Roegzel, W. (2003). Temperature Dependence of Thermal Conductivity Enhancement for Nanofluids. *J. Heat Transfer, 125*, 567-574.

Deegan, R.D. (2000). Pattern Formation in Drying Drops. *Phys. Rev. E, 61*, 475-485.

Deegan, R.D., Bakajin, O., Dupont, T.F., Huber, G., Nagel, S.R., and Witten, T.A. (1997). Capillary Flow as the Cause of Ring Stains from Dried Liquid Droplets. *Nature, 389*, 827-829.

Deegan, R.D., Bakajin, O., Dupont, T.F., Huber, G., Nagel, S.R., and Witten, T.A. (2000). Contact Line Deposits in an Evaporating Drop. *Phys. Rev. E, 62*, 756-764.

Denkov, N.D., Velev, O.D., Kralchevsky, P.A., Ivanov, I.B., Yoshimura, H., and Nagayama, K. (1992). Mechanism of Formation of Two-Dimensional Crystals from Latex Particles on Substrates. *Langmuir*, *8*, 3183-3190.

Digilov, R.M. and Reiner, M. (2004). Trouton's rule for the law of corresponding states. *Euro. J. Phys*. *25*, 15-22.

di Marzo, M., Tartarini, P., Liao, Y., Evans, D., and Baum, H. (1993). Evaporative Cooling Due to a Gently Deposited Droplet. *Int. J. Heat Mass Transfer*, *36*, 4133-4139.

Ding, Y.Z., Zhang, G., Frulke, E.A., Anderson, W.B., and Wu, G. (2006). Heat Transfer Properties of Nanoparticle-in-Fluid Dispersions (Nanofluids) in Laminar Flow. *Int. J. Heat Mass Transfer, 48*, 1107-1116.

Dugas, V., Broutin, J, and Souteyrand, E. (2005). Droplet Evaporation Study Applied to DNA Chip Manufacturing. *Langmuir*, *21*, 9130-9136.

Eastman, J.A., Choi, S.U.S., Li, S., Thompson, L.J., and Lee, S. (1997). Enhanced Thermal Conductivity through the Development of Nanofluids. *Proc. Symp. Nanophase Nanocomposite Mat. II., Boston, 457*, 3-11.

Eastman, J.A., Choi, S.U.S., Li, S., Yu, W., and Thompson, L.J. (2001). Anomalously Increased Effective Thermal Conductivities of Ethylene Glycol-Based Nano-Fluids Containing Copper Nano-Particles. *Appl. Phys. Lett., 78(6),* 718-720.

Eastman, J.A., Phillpot, S.R., Choi, S.U.S., and Keblinski, P. (2004). Thermal Transport in Nanofluids. *Annu. Rev. Mater. Res., 34*, 219-246.

Einstein, A. (1905). Űber die von der Molekularkinetischen Theorie der Wärme Geforderte Bewegung von in Ruhenden Flüssigkeiten Suspendierten Teilchen, *Ann. Phys., (Leipzig), 17*, 549-560.

Einstein, A.Z. (1924). *Phys., 27:1*.

Einstein, A. (1956). *Investigations on the Theory of the Brownian Movement*. Dover, New York.

Evans, W., Fish, J., and Keblinski, P. (2006). Role of Brownian Motion Hydrodynamics on Nanofluid Thermal Conductivity. *Appl. Phys. Lett., 88*, 093116.

Fischer, B.J. (2002). Particle Convection in an Evaporating Colloidal Droplet. *Langmuir, 18,* 60-67.

Fox, R.W., McDonald, A.T., and Pritchard, P.J. (2004). *Introduction to Fluid Mechanics*. 6th ed., Wiley & Sons Inc., New York.

Friedlander, S.K. (2000). *Smoke, Dust, and Haze*. 2nd ed., Oxford University Press, New York.

Ge, Z., Cahill, D.G., and Braun, P.V. (2004). AuPd Metal Nanoparticles as Probes of Nanoscale Thermal Transport in Aqueous Solution. *J. Phys. Chem. B. 108*, 18870-18875.

Glasstone, S., Laidler, K.J., and Eyrinig, H. (1941). *Theory of Rate Processes*. McGraw-Hill, New York, Ch. 9.

Goldstine, H.H. and Goldstine, A. (1982). *The Origins of Digital Computers: Selected Papers*. reprinted, Springer-Verlag, New York, 359-373.

Hamiton, R.L. and Crosser, O.K. (1962). Thermal Conductivity of Heterogeneous Two-Component Systems. *I & EC Fundamentals, 1*, 182-191.

Hammerschmidt, U. and Sabuga, W. (2000). Transient Hot Wire (THW) Method: Uncertainty Assessment. *Int. J. Thermophys., 21(6)*, 1255-1278.

Hisatake, K, Tanaka, S, and Aizawa, Y. J. (1993). Evaporation Rate of Water in a Vessel. *Appl. Phys., 73*, 7395-7401.

Hinze, J.O., Turbulence, 2nd Edition, 1975, McGraw-Hill, New York.

Hu, H. and Larson, R.G. (2002). Evaporation of a Sessile Droplet on a Substrate. *J. Phys. Chem. B, 106*, 1334-1344.

Hu H. and Larson, R.G. (2005). Analysis of the Microfluid Flow in an Evaporating Sessile Droplet. *Langmuir, 21*, 3963-3971.

Hu H. and Larson, R.G. (2005). Analysis of the Effects of Marangoni Stresses on the Microflow in an Evaporating Sessile Droplet. *Langmuir, 21*, 3972-3980.

Incropera, F.P. and DeWitt, D.P. (2002). *Fundamentals of Heat and Mass Transfer*. 5th ed., John Wiley & Sons, New York.

Jang, S. P. and Choi, S.U.S. (2004). Role of Brownian motion in the enhanced thermal conductivity of nanofluids. *Appl. Phys. Lett, 84(21),* 4316-4318.

Johns, A.I., Scott, A.C., Watson, J.T.R., Ferguson, D., and Clifford, A.A. (1988). Measurement of the Thermal Conductivity of Gases by the Transient Hot-Wire Method. *Phil. Trans. R. Soc. Lond. A, 325,* 294-356.

Kak, A.C. and Slaney, M. (1987). *Principles of Computerized Tomographic Imaging*. IEEE Press, New York, 275-296.

Kearne, R.D. and Adrian, R.J. (1990). Optimization of Particle Image Velocimeters. *Meas. Sci. Technol., 2,* 1202-1215.

Kearne, R.D. and Adrian, R.J. (1992). Theory of Cross-Correlation of PIV Images. *Appl. Sci. Res. 49,* 191-215.

Keblinski, P., Phillpot, S.R., Choi, S.U.S., and Eastman, J.A. (2002). Mechanisms of Heat Flow in Suspensions of Nano-sized Particles (Nanofluids). *Int. J. Heat Mass Trans., 45,* 855-863.

Kestin, J. and Wakeham, W.A. (1978). A Contribution to the Theory of the Transient Hot-wire Technique for Thermal Conductivity Measurement. *Physica*, *92A,* 102-116.

Kim, M.J., Beskok, A., and Kihm, K.D., 2002, "Electro-osmosis-driven Micro-channel Flows: A Comparative Study of Microscopic Particle Image Velocimetry Measurements and Numerical Simulations," *Exp. Fluids*, *33*, 170-180

Kincaid, J.F., Eyring, H., and Stearn, A.E. (1941). *Chem. Revs. 28*, 301.

Klassen, M., di Marzo, M., and Sirkis, (1990). Infrared Thermography of Dropwise Evaporative Cooling. *J. ASME HTD, 141,* 117-121.

Kline, S. J. and McClintock, F.A. (1953). Describing Uncertainties in Single-Sample Experiments. *Mechanical Engineering, 75(1),* 3-8.

Kralchevsky, P.A. and Denkov, N.D. (2001). Capillary Forces and Structuring in Layers of Colloid Particles. *Curr. Opin. Colloid Interface Sci., 6,* 383-401.

Krishnamurthy, S., Bhattacharya, P., Phelan, P.E., and Prahser, R.S. (2006). Enhanced Mass Transport in Nanofluids. *Nano Lett., 6(3),* 419-423.

Kumar, D.H., Patel, H.E., Rajeev Kumar, V.R., Sundararajan, T., Pradeep, T., and Das, S.K. (2004). Model for Heat Conduction in Nanofluids. *Phys. Rev. Lett., 93(14),* 144301.

Lee, S.P., Choi, S.U.S., Li, S., and Eastman, J.A. (1999). Measuring Thermal Conductivity of Fluids Containing Oxide Nano-Particles. *J. Heat Transfer, 121,* 280-289.

Lee, S.P., Lee, M.H., Kim, M.T., and Oh, J.M. (2004). Development of a New Sensor and Data Processing Method in Transient Hot-wire Technique for Nanofluid. *J. KAME, 28(5),* 510-515 (in Korean).

Lienhard IV, J.H. and Lienhard V, J.H. (2004). *A Heat Transfer Textbook*. 3rd ed., Phlogiston Press, Cambridge.

Maenosono, S., Dushkin, C.D., Saita, S., and Yamaguchi, Y. (1999). Growth of a Semiconductor Nanoparticle Ring during the Drying of a Suspension Droplet. *Langmuir, 15,* 957-965.

Maglic, K.D., Cezairliyan, A., and Peletsky, V. E. (1984). *Compendium of Thermophysical Property Measurement Methods Volume 1 Survey of Measurement Techniques*. Plenum Press, New York.

Makino, K. and Michiyoshi, I. (1984). The Behavior of a Water Droplet on Heated Surfaces. *Int. J. Heat Mass Transfer, 34*, 781-791.

Maxwell, J.C. (1904). *A Treaties on Electricity and Magnetism*. 2nd ed., Oxford University Press, Oxford.

McNab, G.S. and Meisen, A. (1973). Thermophoresis in Liquids. *J. Colloid Interface Sci., 44*, 339-346.

Michiyoshi, I. and Makino, K. (1978). Heat Transfer Characteristics of Evaporation of a Liquid Droplet on Heated Surfaces. *Int. J. Heat Mass Transfer, 21*, 605-613.

Nagasaka, Y. and Nagashima, A. (1981). Absolute Measurement of the Thermal Conductivity of Electrically Conducting Liquids by the Transient Hot-wire Method. *J. Phys. E: Sci. Instr., 14*, 1435-1440.

Nambu, T., Yamauchi, Y., Kushiro, T., and Sakurai, S. (2005). Micro-convection, Dissipative Structure and Pattern Formation in Polymer Blend Solutions under Temperature Gradients. *Faraday Discuss., 128*, 285-298.

Nan, C.W., Birringer, R, Clarke, D.R., and Gleiter, H. (1997). Effective Thermal Conductivity of Particulate Composites with Interfacial Thermal Resistance. *J. Appl. Phys., 81*, 6692-6699.

Nieto de Castro, C.A., Calado, J.C.G., Wakeham, W.A., and Dix, M. (1976). An Apparatus to Measure the Thermal Conductivity of Liquids. *J. Phys. E: Sci. Instr., 9*, 1073-1080.

Paik, S. Ph.D. (2005). *Spatially Resolved Temperature and Heat Flux Measurements for Slow Evaporating Droplets Heated by a Microfabricated Heater Array*. Ph.D. Dissertation, Texas A&M University, College Station, TX.

Paik, S.W., Kihm, K. D., Lee, S. P., and Pratt, D. M. (2006). Spatially and Temporally Resolved Temperature and Heat Flux Measurements for Slow Evaporating Sessile Droplets Heated by a Microfabricated Heater Array. *J. Heat Transfer* (accepted for publication).

Pak, B.C. and Cho, Y.I. (1998). Hydrodynamic and Heat Transfer Study of Dispersed Fluids with Submicron Metallic Oxide Particles. *Exp. Heat Transfer*, *11*, 151-170.

Parola, A. And Piazza, R. (2004). Particle Thermophoresis in Liquids. *Eur. Phys. J. E.*, *15*, 255-263.

Pasquini, L., Barla, A., Chumakov, A.I., Leupold, O., Rüffer, R., Deriu, A., and Bonetti, E. (2002). Size and oxidation effects on the vibrational properties of nanocrystalline α-Fe. *Phys. Rev. B. 66*, 073410.

Patel, H.E., Das, S.K., Sundararajan, T., Nair, A.S., George, B., and Pradeep, T. (2003). Thermal Conductivities of Naked and Monolayer Protected Metal Nanoparticle Based Nanofluids: Manifestation of Anomalous Enhancement and Chemical Effects. *Appl. Phys. Lett.*, *83*, 2931-2933.

Perrin, J. (1990). *Atoms.* Ox Bow Press, New York.

Peterson, G.P. (1994). *An Introduction to Heat Pipes Modeling, Testing, and Applications*. John Wiley & Sons, New York.

Prasher, R., Bhattacharya, and P., Phelan, P.E. (2005). Thermal Conductivity of Nanoscale Colloidal Solutions (Nanofluids). *Phys. Rev. Lett., 94(2)*, 025901.

Putnam, S.A. and Cahill, D.G. (2005). Transport of Nanoscale Latex Spheres in a Temperature Gradient. *Langmuir, 21(12)*, 5317-5323.

Raffel, M., Willert, C., and Kompenhans, J. (1998). *Particle Image Velocimetry A Practical Guide*. Springer, New York.

Roder, H.M. (1981). A Transient Hot-wire Thermal Conductivity Apparatus for Fluids. *J. Research National Bureau Standards*, *86(5)*, 457-483.

Rohrer, H. (1996). The Nanoworld: Chances and Challenges. *Microelectr. Engin.*, *32*, 5-14.

Rule, T.D. and Kim, J. (1999). Heat Transfer Behavior on Small Horizontal Heaters During Pool Boiling of FC-72. *J. Heat Transfer*, *121*, 386-393.

Rusconi, R., Isa, L., and Piazza, R. (2004). Thermal-lensing Measurement of Particle Thermophoresis in Aqueous Dispersions. *J. Opt. Soc. Am. B.*, *21(3)*, 605-616.

Santiago, J.G., Wereley, S.T., Meinhart, C.D., Beebe, D.J., and Adrian, R.J. (1998). A Particle Image Velocimetry System Microfluidics. *Exp. Fluids*, *25*, 316-319.

Schleiermacher, A.L.E.F. (1888). Über die Wärmeleitung der Gase. Wiedemann. *Ann. Phys.*, *34*, 623-646 (in German).

Shanahan, M.E.R. and Bourges, C. (1994). Effects of Evaporation on Contact Angles on Polymer Surfaces. *Int. J. Adhes. Sci. Technol.*, *14*, 201-205.

Shanahan, M.E.R. (1995). Simple Theory of “Stick-Slip” Wetting Hysteresis. *Langmuir*, *11*, 1041-1043.

Son, S.Y. and Kihm, K.D. (1998). Effect of Coal Particle Size on Coal-Water Slurry (CWS) Atomization. *Atom. Sprays*, *8*, 503-519.

Szczech J.B., Megaridis, C.M., Gamota, D.R., and Zhang, J. (2002). Fine-Line Conductor Manufacturing Using Drop-On-Demand PZT Printing Technology. *IEEE Trans. Electron. Packaging Manufact.*, *25*, 26-33.

Talbot, L., Cheng, R.K., Schefer, R.W., and Willis, D.R. (1980). Thermophoresis of Particles in a Heated Boundary Layer. *J. Fluid Mech., 101*, 737-758.

Tay, B.Y. and Edirisinghe, M.J. (2002). Time-Dependent Geometrical Changes in a Ceramic Ink Droplet. *Proc. R. Soc. Lond. A, 458*, 2039-2051.

Tien, C.L. and Lienhard, J.H. (1971). *Statistical Thermodynamics*, Holt, Rinehart and Winston Inc.

Touloukian, Y.S., Powell, R.W., Ho, C.Y., and Klemens, P.G., (1970). *Thermophysical Properties of Matter*, Vol. 2, Plenum Press, New York.

Tyndall, J. (1870). On Dust and Disease. *Proc. R. Inst. Gt. Br., 6*, 1-14.

Uno, K., Hayashi, K., Hayashi, T., Ito, K., and Kitano, H. (1998). Particle Adsorption in Evaporating Droplets of Polymer Latex Dispersions on Hydrophilic and Hydrophobic Surfaces. *Colloid Polym Sci., 276*, 810-815.

Vadasz, J.J., Govender, S., and Vadasz, P. (2005). Heat Transfer Enhancement in Nano-fluid Suspensions: Possible Mechanisms and Explanations. *Int. J. Heat Mass Transfer, 48*, 2673-2683.

Van der Held, E.F.M. and Van Drunen, F.G. (1949). A method for evaluating thermal conductivity of liquids. *Physica A, 15*, 865.

Vanam,K., Junghans, J., Barlow, F., Selvam, R.P., Balda, J.C., and Elshabini, A. (2005). A Novel Packaging Methodology for Spray Cooling of Power Semiconductor Devices Using Dielectric Lequids. *Appl. Power Electron. Conf. Exposition*, APEC2005, Vol 3,2014-2018

Vijayendran, R.A., Motsegood, K.M., Beebe, D.J., and Leckband, D.E. (2003). Evaluation of Three-Dimensional Micromixer in a Surface-Based Biosensor. *Langmuir*, *19*, 1824-1828.

Vincenti, W.G. and Kruger, C.H. Jr. (1965). *Introduction to Physical Gas Dynamics*. Krieger, New York.

Waldman, L. (1959). Űber die Krafteines Inhomogenen Gases auf Kleine Suspensierte Kugeln. *Z. Naturforsch*, *14a*, 589-599.

Waldman, L. and Schmitt, K.H. (1966). *Thermophoresis and Diffusiophoresis of Aerosol*. Chap. VI. In Davis, C.N., (Ed.) Aerosol Science, Academic, New York.

Wang, J., Harris. J.B., and Adler, J. (1992). Series approach to randomly diluted elastic networks. *Phys. Rev. B, 45*, 7084-7093

Wang, W., Lin, J., and Schwartz, D.C. (1998). Scanning Force Microscopy of DNA Molecules Elongated by Convective Fluid Flow in an Evaporating Droplet. *Biophys. J.*, *5*, 513-520.

Wang, X., Xu, X., and Choi, S.U.S. (1999). Thermal Conductivity of Nanoparticle-Fluid Mixture. *J. Thermophy. Heat Transfer*, *13(4)*, 474-480.

White, F.M. (1986). *Fluid Mechanics*. 2nd ed., McGraw-Hill, New York.

Wilson, O.M., Hu, X., Cahill, D.G.., and Braun, P.V. (2002). Colloidal metal particles as probes of nanoscale thermal transport in fluids. *Phys. Revs. B.*, *66* 224301.

Xie, H., Wang, J., Xi, T., Liu, Y., Ai, F., and Wu, Q. (2002). Thermal Conductivity Enhancement of Suspensions Containing Nanosized Alumina Particles. *J. Appl. Phys.*, *91*, 4568-4572.

Xie, H. Q., Fujii., M., and Zhang, X. (2005). Effect of Interfacial Nanolayer on the Effective Thermal Conductivity of Nanoparticle-Fluid Mixture. *Int. J. Heat Mass Transfer, 48(14)*, 2926-2932, 2005.

Xiong, T.Y. and Yuen, M.C. (1991). Evaporation of a Liquid Droplet on a Hot Plate. *Int. J. Heat Mass Transfer, 34*, 1881-1894.

Xuan, Y., Li, Q., and Hu, W. (2003). Aggregation Structure and Thermal Conductivity of Nanofluids. *AIChE J., 49(4)*, 1038-1043.

Yarin A.L., Szczech, J.B., Megaridis, C.M., Zhang, J., and Gamota, D.R. (2006). Lines of Dense Nanoparticle Colloidal Suspensions Evaporating on a Flat Surface: Formation of Non-Uniform Dried Deposits. *J. Colloid Interface Sci., 294*, 343-354.

Young, H.D. and Freedman, R.A. (1996). *University Physics*. 9th ed., Addison Wesley, New York, 805.

Yu, W. and Choi, S.U.S. (2003). The Role of Interfacial Layers in the Enhanced Thermal Conductivity of Nanofluids: A Renovated Maxwell Model. *J. Nanopart. Resea., 5*, 167-171.

Zhang, Y., Zeng, G., Piprek, J., Bar-Cohen, A., and Shakouri, A. (2005). Superlattice Microrefrigerators Flip-Clip Bonded with Optoelectronic Devices. *J. IEEE Trans. Comp. Pack. Tech., 28(4)*, 658-666.

APPENDICES

APPENDIX A

ESTABLISHING CORRELATION BY BUCKINGHAM-PI THEOREM

Eq. (2-11) shows the parameters which are applied for establishing correlations for predicting the nanofluid thermal conductivity enhancement as

$$\frac{k_{eff}}{k_{BF}} = g\left(f, d_{BF}, d_p, k_p, k_{BF}, \mu_{BF}, \rho_{BF}, C_{p,BF}, T, l_{BF}, k_b\right) \tag{2-11}$$

where f [-] is the volume concentration, d_{BF} [L] is the diameter of a base fluid molecule, d_p [L] is the diameter of a nanoparticle, k_p [$MLT^{-3}\Theta^{-1}$] is the thermal conductivity of a nanoparticle, k_{BF} [$MLT^{-3}\Theta^{-1}$] is the thermal conductivity of a base fluid, μ_{BF} [$ML^{-1}T^{-1}$] is the viscosity of a base fluid, ρ_{BF} [ML^{-3}] is the density of a base fluid, $C_{p,BF}$ [$L^2T^{-2}\Theta^{-1}$] is the specific heat of a base fluid, and T [Θ] is the base fluid temperature, l_{BF} [L] is mean free path of a base fluid molecule, and k_b [$ML^2T^{-2}\Theta^{-1}$] is the Boltzmann constant. Brackets indicate dimension of parameters: L (Length), M (Mass), T (Time), and Θ (Temperature).

From Buckingham-pi theorem, 6 pi groups can be formed by power products since there are 10 variables and four dimensions. Note that the volume concentration *f* is dimensionless unit and Buckingham-pi theorem is not applied for it. In this research, d_{BF}, k_{BF}, μ_{BF}, and T are designated as repeating variables. The pi groups are expressed as

$$g\left(\Pi_1, \Pi_2, \Pi_3, \Pi_4, \Pi_5, \Pi_6\right) = 0 \tag{A-1}$$

where

$$\Pi_1 = d_{BF}^{a1} k_{BF}^{b1} \mu_{BF}^{c1} T^{d1} d_p \tag{A-2}$$

$$\Pi_2 = d_{BF}^{a2} k_{BF}^{b2} \mu_{BF}^{c2} T^{d2} k_p \tag{A-3}$$

$$\Pi_3 = d_{BF}^{a3} k_{BF}^{b3} \mu_{BF}^{c3} T^{d3} \rho_{BF} \tag{A-4}$$

$$\Pi_4 = d_{BF}^{a4} k_{BF}^{b4} \mu_{BF}^{c4} T^{d4} C_{BF,p} \tag{A-5}$$

$$\Pi_5 = d_{BF}^{a5} k_{BF}^{b5} \mu_{BF}^{c5} T^{d5} l_{BF} \tag{A-6}$$

$$\Pi_6 = d_{BF}^{a6} k_{BF}^{b6} \mu_{BF}^{c6} T^{d6} k_b \tag{A-7}$$

By non-dimensional analysis, 6 pi can be algebraically found as

$$\Pi_1 = \frac{d_p}{d_{BF}} \tag{A-8}$$

$$\Pi_2 = \frac{k_p}{k_{BF}} \tag{A-9}$$

$$\Pi_3 = \frac{d_{BF} \rho_{BF} \sqrt{k_{BF} T}}{\sqrt{\mu_{BF}^3}} \tag{A-10}$$

$$\Pi_4 = \frac{\mu_{BF} C_{BF,p}}{k_{BF}} = \mathrm{Pr} \tag{A-11}$$

$$\Pi_5 = \frac{l_{BF}}{d_{BF}} \tag{A-12}$$

$$\Pi_6 = \frac{k_b \sqrt{T}}{d_{BF}^2 \sqrt{k_{BF} \mu_{BF}}} \tag{A-13}$$

In Eq. (A-11), is formed by Prandtl number, non-dimensional parameter indicating the ratio of momentum diffusivity to thermal diffusivity. To set up well known

dimensioinless parameter and make parameter simple, the procedure of regrouping is needed with Eqs. (A-10), (A-12), and (A-13).

$$\Pi_3' = \frac{\Pi_3}{\Pi_5} = \frac{l_{BF}\rho_{BF}\sqrt{k_{BF}T}}{\sqrt{\mu_{BF}^3}} \tag{A-14}$$

$$\Pi_6' = \frac{\Pi_5^2}{\Pi_6} = \frac{l_{BF}^2\sqrt{k_{BF}\mu_{BF}}}{k_b\sqrt{T}} \tag{A-15}$$

$$\Pi_5'' = \frac{\Pi_3'}{\Pi_6'} = \frac{\rho_{BF}k_bT}{l_{BF}\mu_{BF}^2} \tag{A-16}$$

By dividing Eq. (A-16) by 3π, Π_5'' can be replaced by *Re* defined at Eq. (2-14), $\mathrm{Re} = \frac{\rho_{BF}k_bT}{3\pi\mu_{BF}^2 l_{BF}}$. From above results with dimensionless volume concentration *f*, Eq. (2-11) becomes

$$\frac{k_{enh}}{k_{BF}} = g\left(f, \frac{d_{BF}}{d_p}, \frac{k_p}{k_{BF}}, \frac{\mu_{BF}C_{BF,p}}{k_{BF}}, \frac{\rho_{BF}k_bT}{3\pi\mu_{BF}^2 l_{BF}}\right) \tag{A-17}$$

or

$$\frac{k_{enh}}{k_{BF}} = g\left(f, \frac{d_{BF}}{d_p}, \frac{k_p}{k_{BF}}, \mathrm{Pr}, \mathrm{Re}\right) \tag{A-17}$$

From Eq. (A-17), correlation for the nanofluid thermal conductivity enhancement is set up as

$$\frac{k_{eff}}{k_{BF}} = \frac{k_{enh}}{k_{BF}} + 1 = Const \cdot f^a \left(\frac{d_{BF}}{d_p}\right)^b \left(\frac{k_p}{k_{BF}}\right)^c \mathrm{Pr}^d\ \mathrm{Re}^e \tag{2-12}$$

APPENDIX B

LINEAR REGRESSION FOR A CORRELATING FORMULA

Linear regression using the least squares method is applied to achieve correlation on the nanofluid thermal conductivity enhancement as a function of fluidic and heat transfer properties of liquid and nanoparticle conditions. The non-dimensionalized correlation is set up by Buckingham-pi Theorem and shown in Eq. (2-12) as

$$\frac{k_{eff}}{k_{BF}} = \frac{k_{enh}}{k_{BF}} + 1 = Const \cdot f^{a} \left(\frac{d_{BF}}{d_p} \right)^{b} \left(\frac{k_p}{k_{BF}} \right)^{c} \mathrm{Pr}^{d}\ \mathrm{Re}^{e} \tag{2-12}$$

Microsoft Excel offers regression analysis tool using the linear least squares method to fit a line through a set of empirical data. To obtain parameters in Eq. (2-12), it needs to be converted into linear equation since Eq. (2-12) is power series. By applying logarithm for both sides, Eq. (2-12) is converted into

$$\ln\left(\frac{k_{eff}}{k_{BF}} \right) = \ln\left(Const \cdot f^{a} \left(\frac{d_{BF}}{d_p} \right)^{b} \left(\frac{k_p}{k_{BF}} \right)^{c} \mathrm{Pr}^{d}\ \mathrm{Re}^{e} \right) \tag{B-1}$$

From the nature of logarithm, Eq. (B-1) is converted into final form of linear equation of Eq. (2-12) as

$$\ln\left(\frac{k_{eff}}{k_{BF}} \right) = \ln(Const) + a\ln(f) + b\ln\left(\frac{d_{BF}}{d_p} \right) + c\ln\left(\frac{k_p}{k_{BF}} \right) + d\ln(\mathrm{Pr}) + e\ln(\mathrm{Re}) \tag{B-2}$$

By using Microsoft Excel, all coefficients of Eq. (B-2) can be obtained and all parameters of Eq. (2-12) can be achieved with these coefficients.

VITA

Chan Hee Chon was born in Chonju, South Korea on March 20, 1969. He was raised in Chonju and Seoul, South Korea. From Seoul, he went to the Yonsei University, South Korea and received a B.S. in Mechanical Engineering in 1991 and a M.S. in Mechanical Engineering in 1993. After graduation, he worked at the Daewoo Motor Co. for seven years as a research engineer in the area of engine development.

Chan Hee Chon entered Texas A&M University in 2000 and transferred to The University of Tennessee in 2005 and received the Ph.D. in the MABE in Fall of 2006.

Chan Hee is currently working as a research associate at the Department of Mechanical Engineering, Vanderbilt University, Nashville, TN.